

UNIVERSITA' DEGLI STUDI DI PARMA



**Dottorato di ricerca in Scienze della Terra**  
Ciclo XXV (2010-2013)

# **Synthesis and characterization of $\text{CaCoSi}_2\text{O}_6 - \text{Co}_2\text{Si}_2\text{O}_6$ pyroxenes**

Tutor:  
Prof. Mario Tribaudino

Co-Tutor:  
Dott. Danilo Bersani

Coordinatore:  
Prof.ssa Giuliana Villa

Candidata:  
Luciana Mantovani



## **Table of contents**

<b>Introduction</b>	<b>1</b>
 <b>PART I</b> 	
<b>Cobalt pyroxenes in ceramic and mineralogy</b>	<b>4</b>
1.1 Cobalt in traditional and advanced ceramic materials	5
1.2 The use of cobalt in ceramic pigments	8
1.2 Phase diagrams and experimental data	13
1.3 Crystal chemical behaviour: the $\text{CaCoSi}_2\text{O}_6$ - $\text{Co}_2\text{Si}_2\text{O}_6$ series as a model for quadrilateral pyroxenes	22
1.4 A possible new pigment?	30
 <b>PART II</b> 	
<b>Room pressure studies: a ceramic approach</b>	<b>33</b>
2.1 Synthesis and sample characterization	34
2.1.1 Synthesis	34
2.1.2 Sample characterization	38
2.1.2.1 <i>X-Ray Powder Diffraction</i>	38
2.1.2.2 <i>Scanning Electron Microscope – EDS</i>	45
2.1.2.3 <i>Raman Spectroscopy</i>	50
2.1.2.4 <i>Colour coordinates</i>	55
2.1.2.5 <i>Optical Absorption Spectroscopy</i>	60
2.2 Experimental conditions for a Co-pyroxene based pigment	67
 <b>PART III</b> 	
<b>High pressure synthesis: a mineralogical approach</b>	<b>69</b>
3.1 Synthesis and sample characterization	70
3.1.1 Synthesis	70
3.1.2 Sample characterization	73
3.1.2.1 <i>X-ray Powder Diffraction and SEM-EDS analysis</i>	73
3.1.2.2 <i>Raman Spectroscopy</i>	84
3.1.2.3 <i>Transmission Electron Microscope</i>	93
3.2 Comparison with quadrilateral pyroxenes: phase stability and cation ionic radius	95
 <b>Conclusion</b>	 <b>103</b>
<b>References</b>	<b>105</b>
<b>Appendix</b>	<b>112</b>

## ***Introduction***

This thesis concerns cobalt pyroxenes and it is mostly based on the join  $\text{CaCoSi}_2\text{O}_6\text{-Co}_2\text{Si}_2\text{O}_6$ . This series has an interest both in Mineralogy and Ceramic Science.

If we consider Mineralogy it is interesting to stress the analogy with the rock forming quadrilateral pyroxenes formed by diopside - enstatite ( $\text{CaMgSi}_2\text{O}_6$  -  $\text{Mg}_2\text{Si}_2\text{O}_6$ ) and hedenbergite - ferrosilite ( $\text{CaFeSi}_2\text{O}_6$  -  $\text{Fe}_2\text{Si}_2\text{O}_6$ ) series. Moreover, Ca,Co-pyroxenes ( $\text{CaCoSi}_2\text{O}_6\text{-Co}_2\text{Si}_2\text{O}_6$ ) provide a crystal chemical model to study the solid solutions of pyroxenes with a large ionic radius cation in the M2 site, such as diopside ( $\text{CaMgSi}_2\text{O}_6$ ) and hedenbergite ( $\text{CaFeSi}_2\text{O}_6$ ) and those with a smaller cation, such as enstatite, ( $\text{Mg}_2\text{Si}_2\text{O}_6$ ) and ferrosilite, ( $\text{Fe}_2\text{Si}_2\text{O}_6$ ).

Regarding Ceramic Sciences Ca,Co-pyroxenes may be used as a ceramic pigment, with good chemical stability and colour properties, whose stability field and physical properties are poorly constrained.

This work is divided in three parts.

In an introductory first part, the use of cobalt as an industrial inorganic pigment is reported. Cobalt is an important colour agent, giving different hues, obtained by the different coordination number of this element in the structure. If cobalt is in tetrahedral coordination the colour is deep blue (e.g. blue cobalt pigment, based on  $\text{CoAl}_2\text{O}_4$  spinel); otherwise, if the coordination number is higher, six or eight, the hue swings to pink (e.g. Co-olivine  $\text{Co}_2\text{SiO}_4$ , Ca,Co-pyroxenes  $(\text{Ca,Co})\text{Si}_2\text{O}_6$ , or Co-garnet  $\text{Co}_3\text{Al}_2\text{Si}_3\text{O}_{12}$ ). The possible use of Ca,Co-

pyroxenes as a pigment is then introduced; being Ca,Co-pyroxenes a member of the pyroxene mineral family, and in view of planning subsequent experiments, phase equilibria in the closely related group of quadrilateral pyroxenes, constituents of most rock forming pyroxenes, are presented. The presence of a miscibility gap between Ca-rich and Ca-poor pyroxenes, and the coexistence at low pressure of non-pyroxene phases are reported and discussed. The detailed crystal structure of pyroxenes has been then shown, for monoclinic and orthorhombic pyroxenes, in order to provide the basis for an interpretation of the Ca,Co-pyroxene properties at the atomic level. The different pyroxene varieties are related to the phase diagram stability conditions and crystal chemistry.

In the second part, based on a ceramic approach, Co-pyroxenes are synthesized at room pressure, with particular attention to the end member or close to end member  $\text{CoCaSi}_2\text{O}_6$ : this composition is most promising for a possible use as pigment, being stable also at room pressure. The conditions at which the end member is stable as a single phase are sought, as the coexistence with other phases, mostly Co-ackermanite ( $\text{Ca}_2\text{CoSi}_2\text{O}_7$ ) significantly modifies the colour response of the mixture, from pink in pure Ca,Co-pyroxene, to blue if some Co-ackermanite is present. The colorimetric properties of the mixtures obtained at room pressure for the starting materials along the  $\text{CaCoSi}_2\text{O}_6$ - $\text{Co}_2\text{Si}_2\text{O}_6$  series, are also determined at different temperature, relating the colour effect to the percentage of the phases.

In the third part we use a mineralogical crystal chemical approach: a series of pyroxenes with compositions spanning along the  $\text{CaCoSi}_2\text{O}_6$ - $\text{Co}_2\text{Si}_2\text{O}_6$  join are synthesized at high pressure and characterized to understand the effect of Ca

with Co substitution on the crystal-chemical and physical properties of pyroxenes. A pyroxene only phase-diagram is obtained: the observed miscibility gap and the phase transition between  $C2/c$  and  $P2_1/c$  pyroxenes are compared with those of quadrilateral pyroxenes and related to the structural changes obtained by single crystal investigation. The results constrain the chemical properties of pyroxenes, discussing the general point of the substitution of a smaller cation vs a larger one in pyroxenes in view of a simple ionic model. The crystal structure, the symmetry variations, the phase diagram, and the physical properties of the Co-pyroxenes are analyzed by means of a multi-technique approach, using X-Ray Diffraction (powder and single crystal), Transmission and Scanning Electron Microscopy with Energy Dispersive System analysis and Raman micro-spectroscopy.

# **PART I:**

## **Cobalt pyroxenes in ceramics and mineralogy**

## ***Cobalt in traditional and advanced ceramic materials***

Since human beings showed up on the Earth, materials have been important in culture and civilization. As history progressed, advanced technologies involved more and more sophisticated materials, utilizing devices, products, and systems based on advanced materials. The present technical development is strongly dependent on new materials with peculiar mechanical, chemical, electrical, magnetic, or optical properties. Among the new materials, ceramic materials are most relevant.

Ceramic materials and their products are described as non-metallic and inorganic materials. Usually they are cold formed and then consolidated by firing (Singer and Singer, 1979). This definition covers a very wide range of products, depending on chemical composition, raw materials (i.e. clay based ceramics, or other silicates, pure oxides ceramics) or even on the properties of these products and their applications (i.e. home-building ceramics, high temperature ceramics, electronics, chemical and nuclear industry)

Generally the ceramic materials used in technological applications can be divided in two groups: "traditional ceramic materials" and "advanced ceramic materials" (Peco, 1991).

"Traditional ceramics" generally indicate products obtained from raw materials widespread in nature, basically clay, silica and feldspars. Examples of traditional ceramic materials are bricks and tiles in the construction and the porcelain used in the electrical industry. It's worth mentioning at this point, the etymology of the term "ceramic", which derives from the Greek "κέραμος" (keramos) and means "clay".



The term "advanced ceramics" come into use in materials science and technology, to distinguish the most recent technologically oriented materials from "traditional ceramics".

The advanced materials are produced from synthetic raw materials typically composed of pure or nearly pure chemical compounds. They are used in electronics, mechanics, in the production of energy and for pigment applications. For example, some of the most used advanced materials are the ceramics made by alumina ( $\text{Al}_2\text{O}_3$ ), silicon nitride ( $\text{Si}_3\text{N}_4$ ), silicon carbide (SiC) and zirconia ( $\text{ZrO}_2$ ) (Choi and Bansal, 2005).

Traditional ceramics are widespread and produced in large amount; advanced ceramics are more high technology products, produced in smaller amount and for specific applications.

Among advanced materials pigments are specific in providing a stable colour with low economic investment and low-level techniques (Cassese, 2006).

Pigments are defined by the DCMA (Dry Colour Manufacturer Association) as:

*"Coloured, black, white, or fluorescent particulate, organic or inorganic solids which usually are insoluble in, and essentially physically and chemically unaffected by, the vehicle or substrate in which they are incorporated. They alter appearance by selective absorption and/or by scattering of light. Pigments are usually dispersed in vehicles or substrates for application, as for instance in the manufacture of inks, paints, plastics, or other polymeric materials. Pigments retain a crystal or particulate structure throughout the coloration process" (DCMA, 1991).*

Pigments provide the colour simply by mechanical dispersion in the medium that has to be coloured. They are different from dyes, which are dissolved in the substrate losing their structural characteristics (Bondioli, 2008).

## ***The use of cobalt in ceramic pigments***

Cobalt was discovered in 1732 by Georg Brandt, a Swedish chemist. Brandt was attempting to prove that the ability of certain minerals to colour the glass of blue is due to an unknown element and not to bismuth, as it was commonly believed at the time. Cobalt, (Co, atomic number 27) is a transition



*Fig. 1.1: Pure metallic cobalt (from [www.webmineral.com](http://www.webmineral.com))*

Metal appearing in the first period of the Periodic Table between iron and nickel. The ground state atom is  $1s^2 2s^2 2p^6 3s^2 3p^6 4s^2 3d^7$ . This leads to cobalt's commonest valence, i.e.  $Co^{2+}$ , by removal of the two 4s electrons. Another common oxidation state is  $Co^{+3}$ , found for instance in  $Co_3O_4$ , where mixed valences occurs ( $Co^{2+}$  and  $Co^{3+}$ ). Cobalt is a shiny, grey, brittle metal with a hexagonal close packed (CPH) crystal structure at room temperature, which changes at  $421^\circ C$  to a face centred cubic structure. The metal is rarely used as a structural material in the pure form, but as an alloy or a component of another system. The primary ores from which it is extracted are cobaltite ( $CoAsS$ ) and erythrite [ $Co_3(AsO_4)_2$ ] but the main source of this element is a by-product of copper and nickel mining. The copper belt in the Democratic Republic of the Congo and Zambia yields most of the cobalt metal mined worldwide.

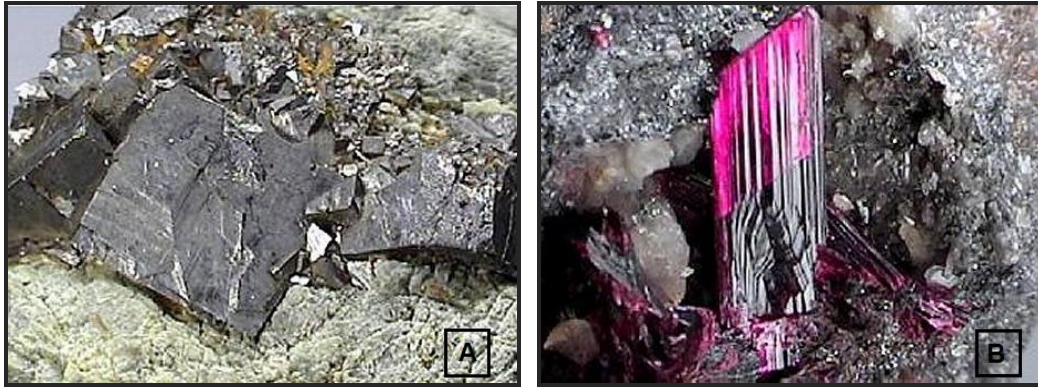


Fig. 1.2 a,b: Images of the primary ores from which cobalt is extracted, a) cobaltite ( $\text{CoAsS}$ ), b) erythrite  $\text{Co}_3(\text{AsO}_4)_2$  (from [www.webmineral.com](http://www.webmineral.com))

Cobalt compounds have historically been used as a dye in porcelain, glass, pottery, tile and enamel. Due to its ability to resist oxidation, cobalt is used in electroplating and in alloys (for magnets, jet engines, gas turbines, magnetic steels and certain stainless steel). This element is also important to human nutrition as it is an essential part of vitamin  $\text{B}_{12}$ .

Cobalt-60, a radioactive isotope of cobalt, is an important source of gamma rays and is used to treat some forms of cancer and as a medical tracer. It has a half-life of 5.27 years and decays into nickel-60 through beta decay (Kim, 1992).



Fig. 1.3: images of the powder of Co-aluminate spinel ( $\text{CoAl}_2\text{O}_4$ ) known as "blue cobalt" (from [www.cemcraft.com](http://www.cemcraft.com))

Cobalt-based ceramic pigments are widely used for coloured glazes in the ceramic industry, for wall or floor wares, and also in the bulk coloration of unglazed, stoneware. The main characteristic of Co-based pigments is an high resistance respect to light, environment, high temperature and chemical agents.

In addition the use of cobalt in pigments provides an extensive range of colour, fine particle size, good hiding power, acid acceptance and compatibility with many organic and inorganic systems.

There is a wide range of various historical cobalt pigments. Some of them are more important in the history of painting, others are more often used for decorating ceramic objects or producing ceramic glaze (Jonynaitė et al., 2009).

The first use of a Co-based pigment was mainly connect with glassware and porcelain in China (Leung and Luo, 2000); later, in Middle Ages, in the same area, it is utilized under the form of dyes (i.e. potassium glass containing cobalt) (Colomban et al., 2001). Some authors also reported an uncommon use of cobalt aluminate pigments in ancient Egyptian ceramics (Riederer, 1974). However the use of cobalt in Europe is not mentioned until the end of the 18<sup>th</sup> century. The first synthesis of a modern cobalt-based pigment (called cobalt green) is dated 1780 by the chemist Sven Rinmann. However, it was not industrially manufactured and used as an artistic colour until 1835 (Bouchard and Gambardella, 2010; Zucchiatti et al., 2006). In the same period all around Europe other cobalt-based pigments are synthesized annealing a mixture of oxides.



Fig.1.4: different colour for cobalt-based pigment (from [www.fineartstore.com](http://www.fineartstore.com))

Usually cobalt in pigments is related to the blue hue but the palette is very large: blue, green, yellow, violet, brown and black (Eppler, 2000; Melo et al., 2003; Mimani and Ghosh, 2000).

There are, however, several environmental issues in the use of cobalt, as this element is highly impacting on man, environment and economics, being cobalt toxic, polluting and expensive (Kim, 1992). At present, research is ongoing to minimize its use and to find phases highly stable to leaching (Fores et al., 2000; Ozel et al., 2010).

Among the cobalt based pigments Co-bearing pyroxenes are proposed as an interesting candidate. The pyroxene structure is interesting in ceramic field both for the good stability to the alteration and the lower cobalt content per formula units respect to the commonly used Co-olivine  $\text{Co}_2\text{SiO}_4$  (Fores et al., 2000; Masse et al., 1999).

However, the very few data are available on Ca,Co-pyroxenes are limited to the end members, their optical spectrum and, only for the  $\text{CaCoSi}_2\text{O}_6$  end member, thermodynamic properties and magnetic low temperature behaviour. No data on phase kinetics and equilibrium and on the colorimetric analysis are available.

Also the structural and spectroscopic behaviour of intermediate  $\text{CaCoSi}_2\text{O}_6$ - $\text{Co}_2\text{Si}_2\text{O}_6$  pyroxenes have not been investigated until now.

In this thesis the binary join  $\text{CaCoSi}_2\text{O}_6$  -  $\text{Co}_2\text{Si}_2\text{O}_6$ , with pyroxene stoichiometry is studied. In this join at room pressure several pigment phases like Ca,Co-pyroxene, Co-olivine and Co-ackermanite are found, and the resulting pigment colour is investigated by means of colorimetric analysis, in view of an application as a ceramic pigment. Moreover the same join at a pressure of 3GPa shows only

pyroxene phases, and provides several constraints to the mineralogy of the pyroxene mineral family.

In the next paragraphs the phase diagram and crystal structure of pyroxenes will be discussed, as a basis for the subsequent analysis and characterization.

## ***Phase diagrams and experimental data on pyroxenes***

### History

Pyroxenes are a family of minerals that include important components of the Earth's crust and mantle and lunar and Martian rocks, and meteorites. They also occur in rocks of widely different composition formed under conditions of regional and contact metamorphism.

Beyond natural ones, several synthetic pyroxene phases can also be synthesized.

The name pyroxene derives from the Greek *pyro*, meaning "fire," and *xenos*, meaning "stranger," and was given by Haüy to the greenish crystals found in many lavas which he considered to have been accidentally included there (Deer et al., 1963).

The crystal structure of pyroxene has been known since 1928, when Warren and Bragg showed that monoclinic  $C2/c$  diopside is characterized by single tetrahedral chains along the  $c$  axis, arranged in layers parallel to (100) (Warren and Bragg, 1928). A few years later, Warren and Modell solved the structure of orthorhombic  $Pbca$  hyperstene by noting the close correspondence, except for the doubled  $a$  axis, between its unit cell parameters and those of diopside (Warren and Modell, 1930).

The monoclinic  $P2_1/c$  structure was predicted by Ito (Ito, 1950) but it was Morimoto (Morimoto et al., 1960) that published the first description of the  $P2_1/c$  pyroxene (pigeonite and clinoenstatite) structures. Other space groups are found



in pyroxenes (Redhammer et al., 2012; Yang et al., 1999), but only in peculiar synthetic compositions and experimental conditions.

Natural and almost all synthetic pyroxenes, actually, occur in one of the three  $P2_1/c$ ,  $C2/c$  and  $Pbca$  space groups.

Since the description of the basic structure types appeared, scores of refinements of both end-member and intermediate pyroxenes provided excellent detailed data on the structural variation of the pyroxene structure as a function of temperature, composition and pressure, in terrestrial, lunar, and meteoritic pyroxenes (Downs, 2003; Iezzi et al., 2011; Tribaudino et al., 2002; Tribaudino et al., 2001).

#### Chemical classification and nomenclature

The general formula of pyroxenes is  $M_2M_1T_2O_6$ , where  $M_2$  are the cations in the distorted polyhedron  $M_2$ , with coordination from 6 to 8 ( $Mg^{2+}$ ,  $Fe^{2+}$ ,  $Li^{2+}$ ,  $Ca^{2+}$ ,  $Na^{2+}$ ),  $M_1$  are cations in the relatively regular  $M_1$  octahedron, i.e. in a sixfold coordination ( $Al^{3+}$ ,  $Fe^{3+}$ ,  $Ti^{3+}$ ,  $Cr^{3+}$ ,  $V^{3+}$ ,  $Ti^{3+}$ , Zr, Sc, Zn, Mg, Fe, Mn ..) and T refers to the cations (Si, Al) present into the tetrahedra forming the pyroxene chains (Putnis, 1992).

The chain silicate structure of the pyroxene offers much flexibility in the incorporation of various cations and the name of the different pyroxenes depends primarily by their chemical composition, within the broader families of clinopyroxenes and orthopyroxenes. The range of the possible chemical substitutions in pyroxene is constrained by the size of the available sites in the structure and the charge of the substituting cations. Twenty minerals from the pyroxene family names are recognized by the International Mineralogical

Association Commission on New Minerals and Mineral Names and 105 previously used names have been discarded (Morimoto, 1989).

The most common pyroxenes can be represented as part of the chemical system  $\text{CaSiO}_3$  (wollastonite, a pyroxenoid),  $\text{MgSiO}_3$  (enstatite), and  $\text{FeSiO}_3$  (ferrosilite). Since no phase with the pyroxene structure exists with calcium content greater than that of the intermediate components diopside ( $\text{CaMgSi}_2\text{O}_6$ ) and hedenbergite ( $\text{CaFeSi}_2\text{O}_6$ ), the field of the possible compositions of pyroxenes falls within the quadrilateral end members diopside-enstatite and hedenbergite-ferrosilite. As shown in Fig. 1.5, the composition of natural quadrilateral pyroxenes is limited by a miscibility gap between Ca-poor and Ca-rich pyroxenes. This is due to the larger cation radius of Ca (1.0 Å), that hinders complete solid solution.

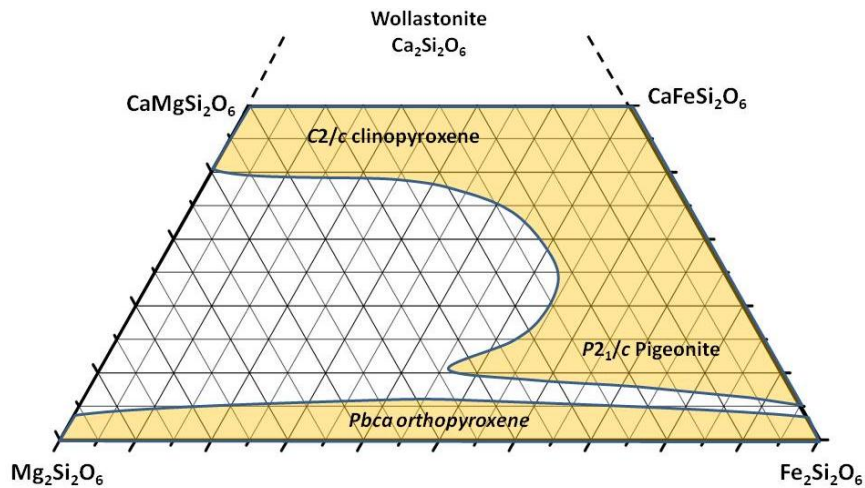


Fig. 1.5: the pyroxene quadrilateral (after Brown, 1967, modified)

Ferrous iron and magnesium are able to give complete solid solution since they have similar ionic sizes (i.e. 0.78 and 0.72 Å) respectively (Shannon, 1976), and identical charges. Complete substitution exists between enstatite ( $\text{Mg}_2\text{Si}_2\text{O}_6$ ) and

ferrosilite ( $\text{Fe}_2\text{Si}_2\text{O}_6$ ), and between diopside ( $\text{CaMgSi}_2\text{O}_6$ ) and hedenbergite ( $\text{CaFeSi}_2\text{O}_6$ ) (Cameron and Papike, 1981; Downs, 2003).

Pyroxenes in the quadrilateral with compositions near the diopside-hedenbergite join (Ca-rich) exist only in the monoclinic  $C2/c$  form. Those with compositions near the enstatite - ferrosilite join (Ca-poor) can be subdivided in two structural types: they are orthorhombic (orthopyroxenes) if they contain less than about 5% of  $\text{CaSiO}_3$ , and monoclinic  $P2_1/c$  (pigeonite) if they contain between 5% and 20% of  $\text{CaSiO}_3$ . The pigeonite inverts to orthorhombic structure if it slowly cools at low temperatures. The inversion of high-temperature pigeonite to low-temperature orthopyroxene is accompanied by the exsolution of lamellae of calcium-rich and magnesium-iron-rich phases: as high-temperature monoclinic pigeonite cools down, it exsolves calcium ions to form the Ca-rich augite lamellae and inverts to the orthorhombic enstatite structure (Huebner, 1980a). At high pressure transition to monoclinic structure in orthorhombic enstatite is documented (Gasparik and Lindsley, 1980).

Phase diagram at low pressure

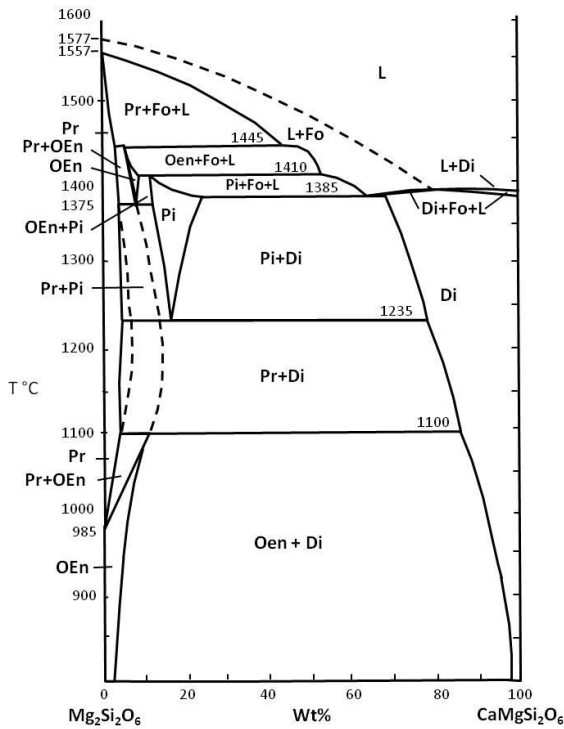


Fig. 1.6: subsolidus phase equilibria and solid solution in the system Di-En ( $Mg_2Si_2O_6 - CaMgSi_2O_6$ ) at low pressure. Dotted line indicates metastable two phase field of protoenstatite (Pr) and orthoenstatite (Oen); Di: diopside, Fo: forsterite, L: liquidus (Longhi and Boudreau, 1980).

The mutual equilibrium relations between pyroxenes were widely studied, and the main results, starting point for our studies on Ca,Co-pyroxenes will be here summarized for the two diopside - enstatite ( $CaMgSi_2O_6 - Mg_2Si_2O_6$ ) and hedenbergite - ferrosilite ( $CaFeSi_2O_6 - Fe_2Si_2O_6$ ) joins.

Boyd and Schraier (Boyd and Schairer, 1964) first described the phase diagram of the binary join diopside-enstatite. In their study, at room pressure, the miscibility gap between Ca-rich and Ca poor pyroxenes was constrained, as well as the melting conditions for pyroxenes. Incongruent melting of forsterite assemblage ( $Mg_2SiO_4 + \text{melt}$ ) was found in Ca-poorer pyroxenes, with forsterite as the only non pyroxene solid phase in the diagram (fig.1.6).

Quite complex polymorphism is found at low pressure in Ca-poorer pyroxenes, with monoclinic  $P2_1/c$  and orthorhombic  $Pbca$  and  $Pbcn$  phases (respectively

orthopyroxene and protopyroxene) present at different temperature and Ca content. Further studies clarified the issue of the phase diagram on the Ca-poorer side (Carlson, 1989; Huebner, 1980b; Longhi and Boudreau, 1980). This polymorphism disappears at high pressure.

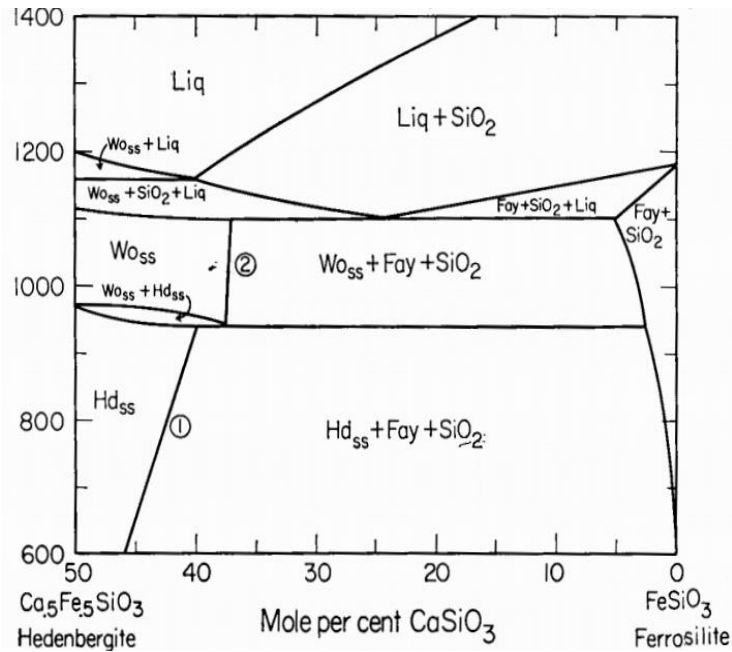


Fig. 1.7: subsolidus phase relations in the join hedenbergite-ferrosilite ( $\text{CaFeSi}_2\text{O}_6$ - $\text{Fe}_2\text{Si}_2\text{O}_6$ ) at low pressure Hd: hedenbergite, Fay: fayalite, Wo: wollastonite ss:solid solution, Liq:liquidus (Lindsley and Munoz, 1969)

On the Fe counterpart the paper by Lindsley and Munoz (1969) highlights that pyroxene is present at room pressure only in the Ca richer side of the join, being stable at higher Fe content an assemblage of fayalite ( $\text{Fe}_2\text{SiO}_4$ ) and  $\text{SiO}_2$ . To note, the orthopyroxene phase is not stable at room pressure. This point affects little natural pyroxenes which are generally on the Mg richer side of the quadrilateral.

Phase diagram at high pressure

At higher pressure the phase diagram strongly simplifies in both of the joins: only the  $C2/c$ ,  $Pbca$  and  $P2_1/c$  phases are present.

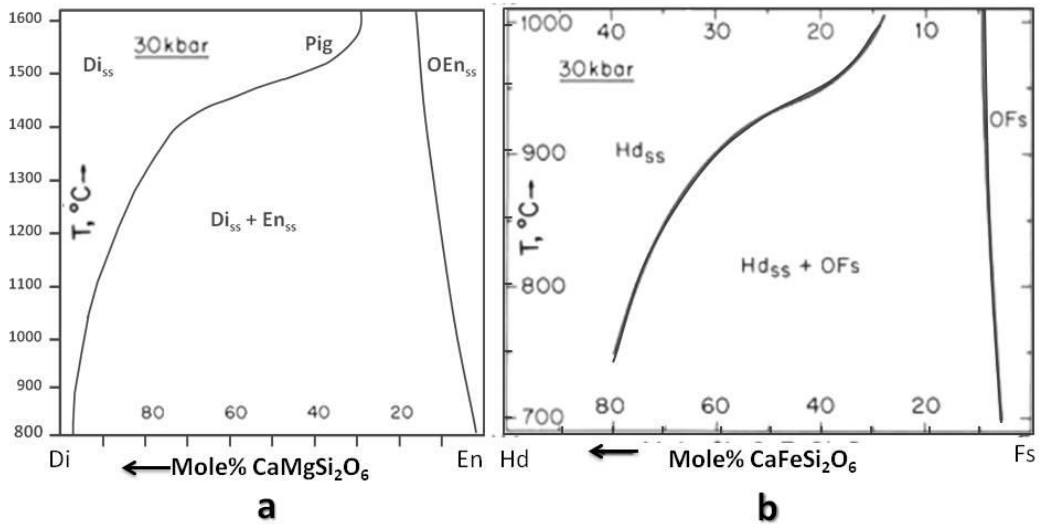


Fig. 1.8: phase diagram of the Di-En and Hd-Fs series at 3 GPa a) diopside enstatite (Lindsley, 1980) and b) hedenbergite-ferrosilite (Lindsley and Munoz, 1969)

The miscibility gap in Ca-Mg pyroxenes was determined by several reversal experimental runs i.e. using both starting materials containing pyroxenes Ca-richer and poorer than the final composition (Gasparik and Lindsley, 1980). At high dry pressure the melting temperature increases and wide solid solution in the subsolidus can be obtained in a narrow field between the solidus and the miscibility gap (Lindsley, 1980).

In Ca-Fe pyroxenes the phase diagram is similar to that of Ca-Mg ones, but with larger miscibility in the Ca-richer pyroxene side, and lower melting temperature (Lindsley and Munoz, 1969). The non pyroxene phases present at room pressure disappear.

In Ca,Co-pyroxenes we can expect a strong similarity with Ca-Fe and Ca-Mg pyroxenes: the substitution of Co in a  $\text{CaCoSi}_2\text{O}_6$ - $\text{Co}_2\text{Si}_2\text{O}_6$  join is similar to that

in  $\text{CaMgSi}_2\text{O}_6$ - $\text{Mg}_2\text{Si}_2\text{O}_6$  and  $\text{CaFeSi}_2\text{O}_6$ - $\text{Fe}_2\text{Si}_2\text{O}_6$  pyroxenes, being the cation radius of Co (0.745 Å) intermediate between that of Mg and Fe. However as yet no experimental evidence supporting this expectation is given: literature data on the CaCo-pyroxenes are scarce, concerning the synthesis and the characterization of the end members and mostly the Ca-rich end-member.

The first synthesis of stoichiometric  $\text{CaCoSi}_2\text{O}_6$  pyroxene was done by White et al. (White et al., 1971), after a suggestion of the likely existence of such pyroxene is given by Biggar (Biggar, 1969). Navrotsky et Coons (Navrotsky and Coons, 1976) synthesized some crystal of  $\text{CaMgSi}_2\text{O}_6$  at a temperature of 1150°C, finding melt at 1400°C. Also Durand et al. (Durand et al., 1996) studied  $\text{CaCoSi}_2\text{O}_6$  synthesizing the compound with sol-gel method and annealing at 1100°C. Further synthesis were conducted via ceramic route between 1000°C and 1250°C by Masse et al. (Masse et al., 1999), that reported coexistence of pyroxene and other phases, like Co-akermanite and quartz, without determining whether they are metastable or not. Both Masse et al. and Navrotsky et Coons find incongruent melting for the composition  $\text{CaCoSi}_2\text{O}_6$  between 1175°C and 1250°C.

Data on intermediate  $\text{CaCoSi}_2\text{O}_6$ - $\text{Co}_2\text{Si}_2\text{O}_6$  samples are limited to an investigation by Mukhopadhyay and Jacob (Mukhopadhyay and Jacob, 1996), at the unique temperature of 1150 °C and room pressure, within a broader study on CaO-CoO-SiO<sub>2</sub> system. In that paper the isothermal binary section along  $\text{CaCoSi}_2\text{O}_6$  -  $\text{Co}_2\text{SiO}_4$  composition shows that pyroxene has a very limited solution on the Ca-rich side, and is readily destabilized into a three phase assemblage SiO<sub>2</sub> + clinopyroxene +  $\text{Co}_2\text{SiO}_4$  olivine. The extension of the pyroxene solid solution at

some different temperature was not determined, and sample characterization is also lacking, in spite of the possible interest in ceramic sciences.

As concerns the other end member,  $\text{Co}_2\text{Si}_2\text{O}_6$  the literature data are even scarcer. Preliminary attempts to synthesize the Co-orthopyroxene ( $\text{Co}_2\text{Si}_2\text{O}_6$ ) failed and  $\text{Co}_2\text{SiO}_4$  olivine and tridymite were found instead (Masse and Muan, 1965). Co-orthopyroxene was synthesized at 2 GPa and 800°C in the Akimoto et al. work (Akimoto et al., 1965), which, at present, is the only high pressure study on Co-pyroxenes. In their paper Akimoto found in the synthesis above 7 GPa the formation of monoclinic  $\text{Co}_2\text{Si}_2\text{O}_6$ . The successful synthesis at high pressure of the Co-orthopyroxene suggests that, like in Ca-Fe pyroxenes, at high pressure the olivine + tridymite assemblage disappears, and only pyroxene phases are present. High pressure experiments which can provide a model to interpret the mutual relations between pyroxenes of specific mineralogical and petrological interest, have been therefore done in this work.



## ***Crystal chemical behaviour: the $\text{CaCoSi}_2\text{O}_6$ - $\text{Co}_2\text{Si}_2\text{O}_6$ series as a model for quadrilateral pyroxenes***

The above phase diagrams and the physical properties of pyroxenes can be interpreted by their structure at the atomic level, which requires a basic knowledge of their structure.

Pyroxenes are single chain silicates; they crystallize in the monoclinic and orthorhombic system. The monoclinic pyroxene with  $C2/c$  space group, as found for instance in diopside, provides a standard model for the discussion of the topologies of pyroxenes in other symmetries.

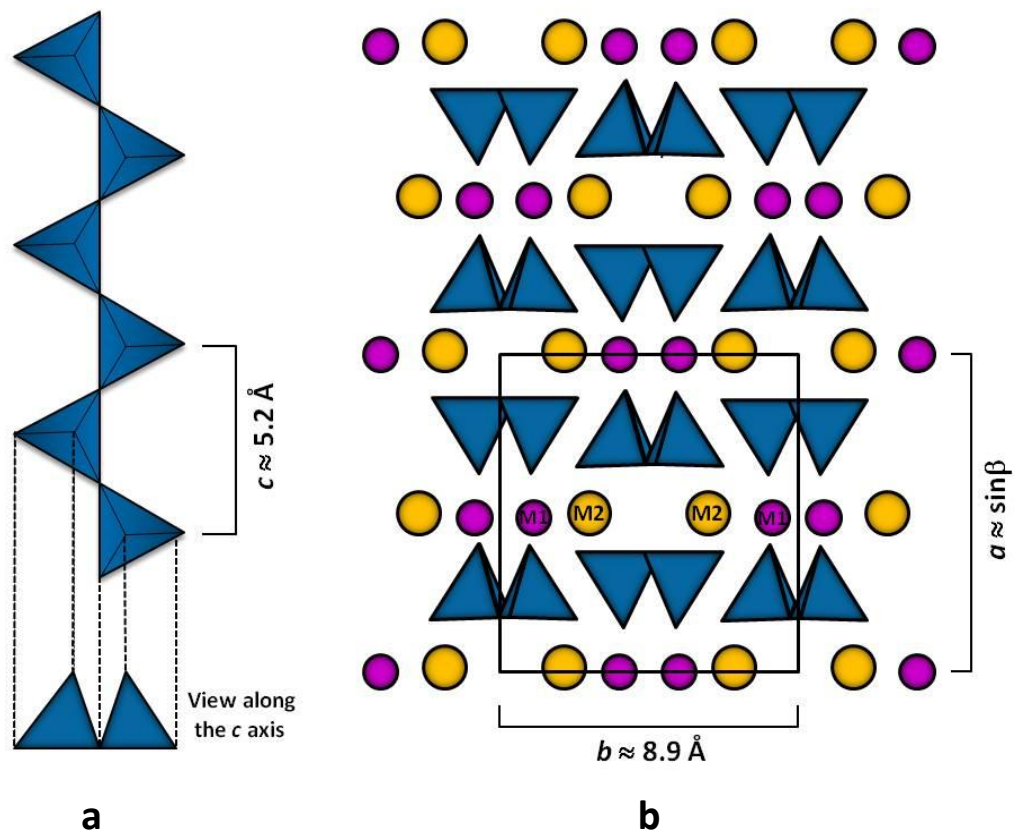


Fig. 1.9: projection of monoclinic  $C2/c$  pyroxene along the (a)  $a$  and (b)  $c$  axis; from (Putnis, 1992), modified.

The basic unit of pyroxenes is a single chain of  $[\text{SiO}_4]^{4-}$  tetrahedra linked by shared oxygen atoms [bridging oxygen, named O3 in the crystallographic nomenclature (Burnham et al., 1967)]. The tetrahedra within a single chain point all in the same direction, marked by the O1 oxygen at the tetrahedral vertex, and the basis of all tetrahedra within a chain lie approximately onto the same plane, formed by the two O3 bridging oxygen, and the O2 non bridging oxygen. The tetrahedral chain is elongated in the **c** axis direction, with a repeat of two tetrahedra, which defines in all pyroxenes the **c** parameter of the unit cell ( $\approx 5.2$  Å) (fig. 1.9 a).

Figure 1.9 b shows the structure projected along the **c** axis, the tetrahedral chains are arranged parallel to each other, in layers onto the (100) plane, with apex on alternating direction. The **b** axis repeat of pyroxene ( $\approx 8.9$  Å) corresponds to the distance of two tetrahedral chains on the same layer pointing on the same direction. The **a** axis repeat is the distance repeat of corresponding tetrahedra in a direction normal to the **b** axis. The layers of tetrahedral chains onto (100) are stacked, and shifted to each other, so that the angle between **a** and the chain direction, i.e. **c** axis, is between 100 and 110°. In clinopyroxenes this corresponds to the  $\beta$  angle. For instance in diopside the unit cell has a  $\beta$  equal to 105.9° (Cameron and Papike, 1981). Using the polytypic nomenclature monoclinic pyroxenes can be considered as 2M.

In this  $C2/c$  structure the chains are all the same and are symmetrically related one to another. Differences between pyroxene structures are found in the tetrahedral chain stacking, and in the loss of equivalence between the different chains, or within a single chain. Also within a single structure type the chain is

rather flexible, as it can rotate and single tetrahedra may slightly change their shape.

As above reported, the cation positions in pyroxene are three, M1, M2 and T. M1 sites lie between the apices of the opposite tetrahedra; M2 sites lie between their bases, and T sites into the tetrahedron. In  $C2/c$  space group pyroxenes both the M1 and M2 atoms lie on the two-fold rotation axis and coordinate respectively six and six-eight oxygen; oxygen lie in a general position, i.e. off any symmetry element. T atoms lie in a general position close, but not at the centre of the tetrahedron M2 polyhedra have an octahedral coordination (6-fold coordinated) when containing a smaller cation, or is 8-fold coordinated when occupied by a larger cation.

The M1 octahedra form edge-sharing chains which run parallel to the silicate chains. Together with the tetrahedral chains they model the shape of the M2 polyhedron, which is in fact a cavity between tetrahedral and octahedral chains (fig. 1.10 a).

In the unit cell of the  $C2/c$  space group each tetrahedral chain has a symmetry equivalent at the 0.5, 0.5, 0 fractional coordinates, accounting for the C (centered) lattice. A  $c$  glide plane is located through the chains, and reflects each tetrahedron of a given chain in the subsequent one in the same chain after a shift by 0.5 of the  $c$  axial parameter.

The way in which the silicate chains are linked to the cation polyhedra is important in understanding the polyhedral response to the changes in composition, temperature and pressure. The M1 and M2 polyhedra expand and contract significantly, whereas this does not occur in T tetrahedra. The tetrahedral chain changes, therefore its length to accommodate it.

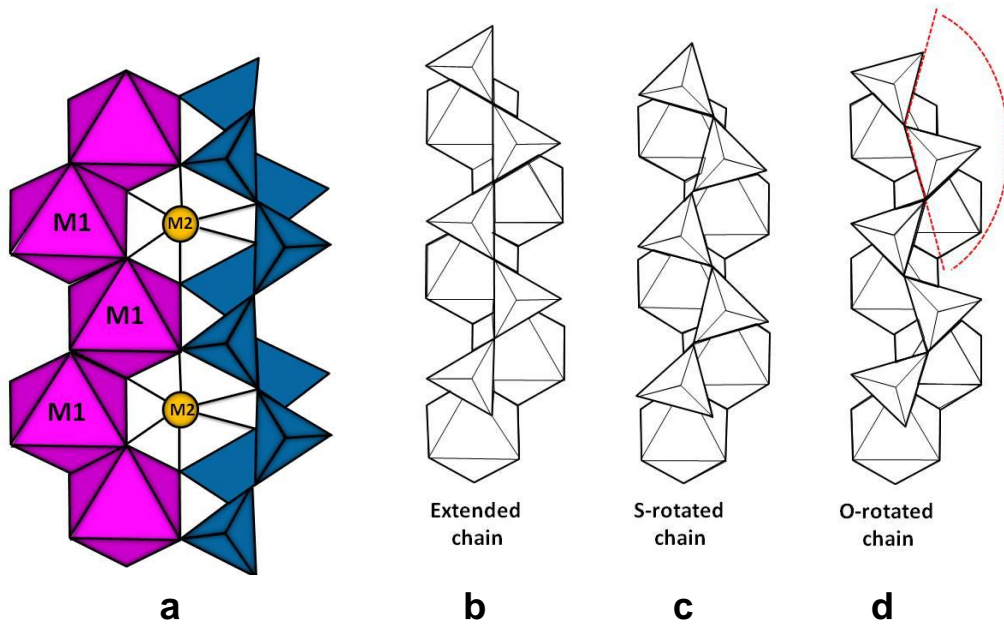


*Fig. 1.10: The linkage between a single  $\text{SiO}_4$  chain and a chain of octahedral: a) and b) fully extended chain; c) and d) when the octahedral become smaller, due to the occupancies by a smaller cation, the tetrahedral chains have to shorten by rotation of the individual tetrahedral to achieve a successful linkage. There are two possible sense of tetrahedral rotation, termed S-rotation or O-rotation. After (Cameron and Papike, 1981).*

Figure 1.10 a and b shows the way in which a straight silicate chain is linked, by its apices to an edge sharing octahedral chain. This is the fully extended situation; if the octahedra were any larger, the pyroxene chain could not accommodate them in this way, posing a limit to the size of the cation in the M1 polyhedron. A contraction of the octahedra is accommodated by rotation of the individual  $\text{SiO}_4$  tetrahedra which shortens the chain length. Alternate tetrahedra along the chain always rotate in opposite sense, but there are two different rotation possibilities leading to two types of chains, named the O-chain and the S-chain (fig. 1.10 c and d). In the  $C2/c$  structure the chains are all equivalent by symmetry and O-rotated. If adjacent chains are not of the same type they lose

their equivalence and the symmetry of the space group is reduced. This is what occurs in  $P2_1/c$  pyroxenes, in response to a decrease in the size of the M2 cation.

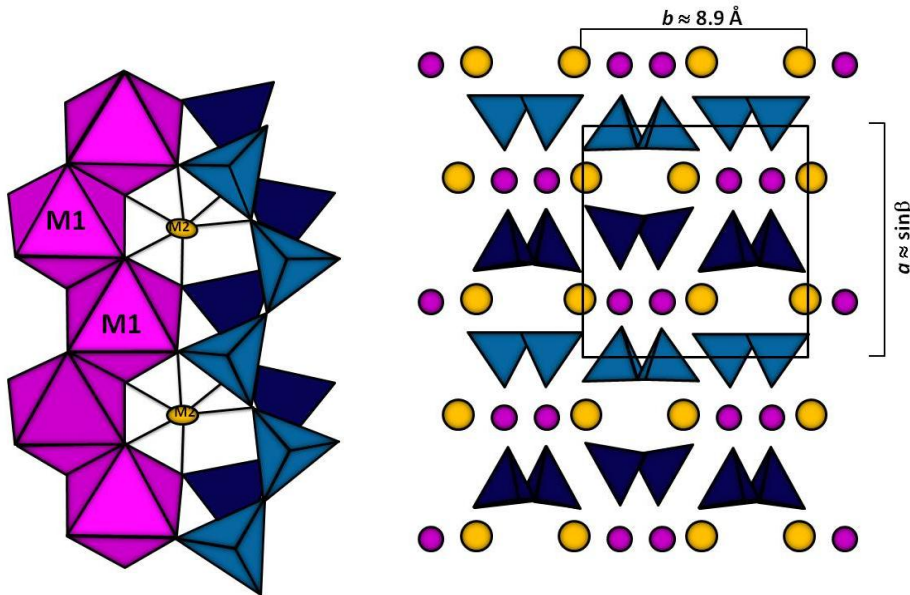


Fig. 1.11: representation of  $P2_1/c$  pyroxenes a) light blue and deep blue represent different rotation of the two tetrahedral chain in  $P2_1/c$  pyroxene (s-rotated and O-rotated); (b) projection of the structure along the  $c$  axis;

In  $P2_1/c$  the chains are rotated in opposite sense, one being S-rotated and the other O-rotated. The diad axes through the M1 and M2 sites are also lost and the symmetry is reduced, as the diad axis becomes a screw  $2_1$  axis.

In  $P2_1/c$  however the stacking is the same as in  $C2/c$  pyroxenes, and along the  $a$  direction, all layers are stacked in the same way.

In  $Pbca$  orthopyroxenes, subsequent layers are instead stacked in opposite directions, with the formation of a mirror plane at the unit cell scale. This results in a doubling of the unit cell along the  $a^*$  ( $d_{100}$ ), and in an orthorhombic symmetry (fig. 1.12 a). From the geometrical point of view an orthorhombic unit cell with

$$\mathbf{a}_{\text{opx}} = 2a_{\text{cpx}}\sin\beta, \quad \mathbf{b}_{\text{opx}} = \mathbf{b}_{\text{cpx}}, \quad \mathbf{c}_{\text{opx}} = \mathbf{c}_{\text{cpx}}$$

is obtained, but like in  $P2_1/c$  clinopyroxenes there are two equivalent tetrahedral chains for each unit cell. The symmetry  $Pbca$ , requires that new glide planes normal to the  $\mathbf{a}$  and  $\mathbf{c}$  axes are formed.

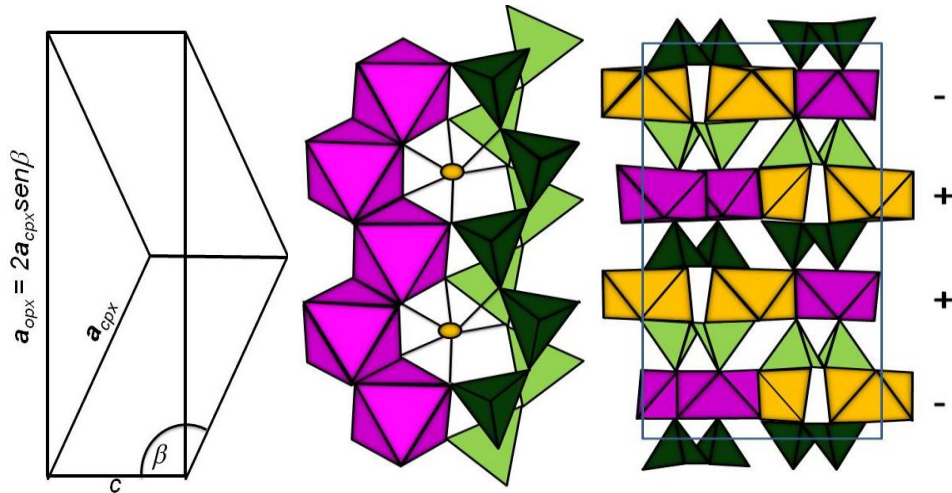


Fig. 1.12: a) the relationship between the unit cells of clinopyroxene and orthopyroxene; b) view of the orthopyroxene structure and the way in which the tetrahedra links to polihedra b) projection along the  $\mathbf{c}$  axis. The chain arrangement along the  $\mathbf{c}$  axis results in non equivalent chains, labelled A and B, and an alternation of octahedral in the + and - orientation (Burnham et al., 1967).

To clarify the differences between the three most common space group in pyroxene the I-beam configuration is used (fig. 1.13). This configuration explains better the M1 position. The + or - depend on the orientation of the octahedra between the chain apices. Viewed along the  $\mathbf{c}$  axis the octahedral can have a triangular face pointing downwards (+) or upwards (-) depending on the relative position of the chains along their length.

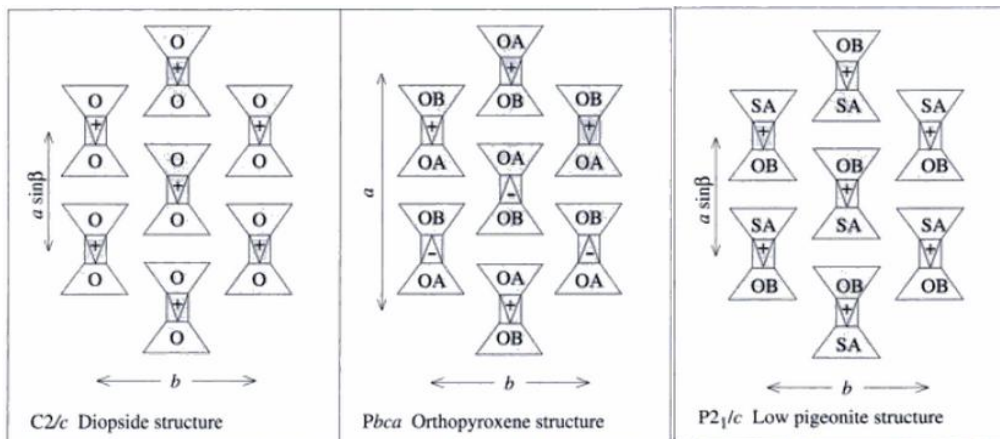


Fig. 1.13: I-beam diagrams for the three pyroxene structure examined. S and O refer to the rotations of the of the tetrahedral chain. M1 octahedra are labelled + or -; A and B refer to non-equivalent chains (Cameron and Papike, 1981).

A structural change from the  $C2/c$  to  $P2_1/c$  and  $Pbc_a$  symmetry can be observed at room pressure as an effect of cation substitution into the M2 site. The larger Ca cation is well hosted into the M2 polyhedron in the 8-fold configuration of  $C2/c$  diopside or hedenbergite. In the  $C2/c$  configuration of the M2 polyhedron the M2 is bonded with four symmetry equivalent couples of oxygen.

However the size of the M2 cavity is larger than suitable for the smaller  $\text{Fe}^{2+}$  and  $\text{Mg}^{2+}$ , which find a better configuration when the equivalence between the symmetry related couples of oxygen is lost. That means that increasing  $\text{Fe}^{2+}$  and  $\text{Mg}^{2+}$  prompts for a  $P2_1/c$  configuration, quite similar at a local level to that of orthorhombic  $Pbc_a$ . In solid solutions a phase transition of average structures between  $C2/c$  and  $P2_1/c$  is then promoted by compositional changes. Moreover the coexistence at a local level of different M2 configurations for the smaller and larger cations causes in intermediate pyroxenes a significant strain. Only at high temperature in subsolidus the strain is released, and wide solid solution is stable, whereas at lower temperature solid solution is limited, and the two phase

assemblage is found in intermediate pyroxenes. This is the crystal chemical basis for the miscibility gap between Ca-rich and Ca-poor pyroxenes, widely used for geothermometry (Gasparik, 1984).

The point is discussed in several papers investigating the crystal structure of pyroxenes along the joins diopside-enstatite (Bruno et al., 1982; Tribaudino and Nestola, 2002) and hedenbergite-ferrosilite (Ohashi et al., 1975a), i.e. from Ca-Mg and Ca-Fe substitutions in the M2 site. It is relevant to the interpretation of the two phase assemblage in natural pyroxenes, and may also explain the limited solid solution of Ca-Fe pyroxenes observed at room temperature: the strain due to the Ca-Fe substitution increases the free energy of the pyroxene phases, and the strained solid solutions have larger free energy than an assemblage containing fayalite and silica.

In the above papers the discussion is limited to the investigated joins; moreover on the hedenbergite - ferrosilite join only one rather old paper is available. An attempt to compare and model the structural effect of the entrance of a smaller cation into a Ca-rich pyroxene requires data on different substituting cations.

By this respect Co pyroxenes provide a suitable model: the cation radius of Co is intermediate between that of  $\text{Mg}^{2+}$  and  $\text{Fe}^{2+}$ , the end member structures do share the same space group as end-member quadrilateral pyroxenes, being  $\text{CaCoSi}_2\text{O}_6$  *C2/c* and  $\text{Co}_2\text{Si}_2\text{O}_6$  *Pbca*, and the mechanism of the substitution along the join is expected to be similar (Ghose et al., 1987; S Sasaki, 1982).

We have therefore determined the crystal structure of three *C2/c* Ca,Co-pyroxenes, and the cell parameters for all the pyroxenes along the join. The data are used for an interpretation of the properties of Ca,Co-pyroxenes, and to obtain a model for the solid solutions between Ca and smaller divalent cations like Mg,



Fe or Co. The results for the single crystal refinements are object of a separate publication and here only the major results, of interest for crystal chemical discussion, will be reported.

## ***A possible new pigment?***

The crystal chemical characterization of Co bearing pyroxenes has an impact on the study of pigments.

The entrance of Co in the pyroxene structure occurs via the substitution into the M1 and/or M2 sites but Co can enter in the M2 site only when the site is not occupied by cations with larger ionic radius, which may only enter the M2 site, like Ca or Na. In pyroxenes along the series  $\text{CaCoSi}_2\text{O}_6$ - $\text{Co}_2\text{Si}_2\text{O}_6$ , Co fully occupies the M1 site, and the substitution, from crystal chemical point of view, is that of Co for Ca in the M2 site.

The colour of the pigment is given here only by cobalt. It varies according to the interaction of the outer electrons of Co with the surrounding oxygen, which causes selective absorption of light, and hence colour. The structure environment of first neighbour oxygen coordinating cobalt and it is therefore crucial for the resulting colour.

However, although the atomic environment of  $\text{Co}^{2+}$  is obviously different in the M1 and M2 sites, and the absorption peaks are different for  $\text{Co}^{2+}$  in different coordination, the resulting pink colour is very similar in  $\text{CaCoSi}_2\text{O}_6$  pyroxenes where no Co enters in M2 and in  $\text{Co}_2\text{Si}_2\text{O}_6$  where the M2 is fully occupied by Co (S Sasaki, 1982). Intermediate pyroxenes are then expected to show a similar colour (this will be confirmed by the present thesis). The pink colour of Co pyroxenes may therefore be the basis for a new pigment, based on pyroxenes.

Ca,Co-pyroxenes are actually interesting candidates as a ceramic pigment both for the strong resistance of the pyroxene structure and the final colour given by the entrance of Co in octahedral site. Ca,Co-pyroxenes are alternative to the Co-olivine based pigments. A possible advantage may be in the lower Co-content in

the formula unit of pyroxene  $\text{CaCoSi}_2\text{O}_6$  respect to  $\text{Co}_2\text{SiO}_4$ , with the advantage of reducing the use of the cobalt.

The entrance of Co in the tetrahedral site has been never observed in pyroxenes, but Co may enter in the tetrahedral coordination in glasses and in several phases, like spinel ( $\text{CoAl}_2\text{O}_4$ ) or Co-akermanite ( $\text{Ca}_2\text{CoSi}_2\text{O}_7$ ), showing here distinctly different absorption and an overall blue colour. The Co akermanite is found by Mukhopadhyay and Jacob (1996) and Masse et al. (1999), coexisting with Co-pyroxene, and glass obviously occurs at higher temperature. From a colouring point of view cobalt in tetrahedral coordination has a higher hiding power respect that in octahedral coordination (Llusar et al., 2001), and special care has to be done in avoiding the formation of these phases, to exploit the use of Co as a pigment.

The point of the synthesis and the characterization of a cobalt-based pyroxene becomes therefore extremely important in order to define a potential use in ceramics. As previously shown at room pressure, i.e. at a pressure which is ordinarily used for the ceramic manufacturing, only  $\text{CaCoSi}_2\text{O}_6$  pyroxene is stable, and the interest stems from this end member.

Co-richer solid solutions require high pressure synthesis and consequently high production cost. However the characterization of the end-member  $\text{CaCoSi}_2\text{O}_6$  as a pink pigment cannot be separated from the basic knowledge of the entire system  $\text{CaCoSi}_2\text{O}_6$ - $\text{Co}_2\text{SiO}_4$  both from a structural and phase equilibria point of view.

In a first part of this work synthesis at room pressure and characterization of a cobalt-based pyroxene with the formula  $\text{CaCoSi}_2\text{O}_6$  is done in order to define a potential use in ceramics, in view of a possible further investigation on the

interaction between pigment, glaze and enamel. Also other compositions along the  $\text{CaCoSi}_2\text{O}_6\text{-Co}_2\text{Si}_2\text{O}_6$  join are studied at room pressure, to clarify the phase diagram and the bulk colorimetric behaviour of the synthesized samples.

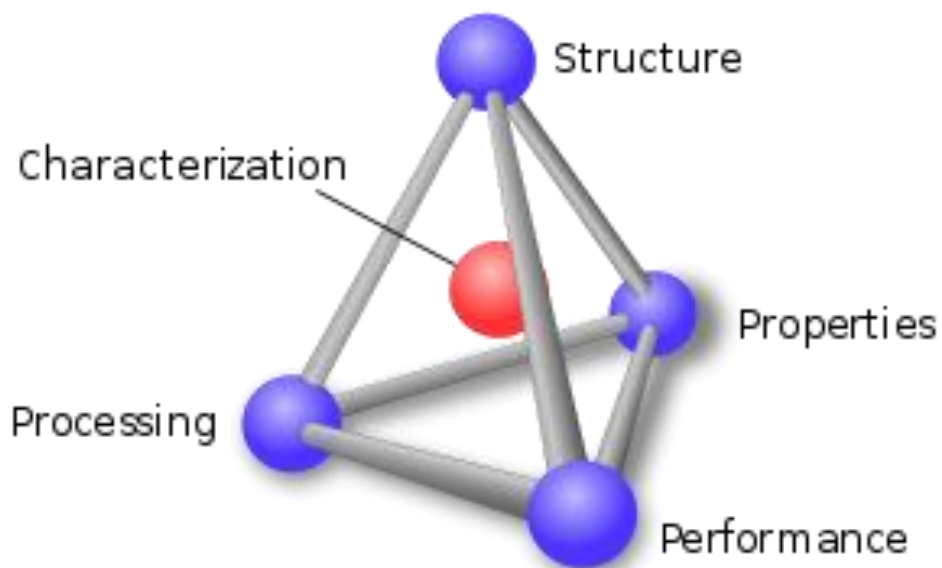
In the second part of this thesis, CaCo-pyroxenes were synthesized at high pressure (3GPa) in order to analyze the mechanism of cation substitution in the join. Phase transition, changes in symmetry and in the structure were investigated and compared to the quadrilateral pyroxenes.



*Fig. 1.14: image of the  $\text{CaCoSi}_2\text{O}_6$  pyroxene synthesized at  $P = 3\text{GPa}$  and  $T = 1200^\circ\text{C}$*

## PART II

# Room pressure studies: a ceramic approach



## ***Synthesis and sample characterization***

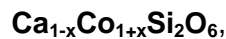
### **Synthesis**

The syntheses are carried out at room pressure, with the aim to determine which are the best conditions in terms of temperature, time and composition for the synthesis of a pink pigment with a pyroxene structure. We consider best conditions those where Ca,Co-pyroxene is present as a single phase. In this work technological tests on the obtained pigments, like coating on surface or annealing together with enamel, are not done.

Starting from the Ca-rich end-member ( $\text{CaCoSi}_2\text{O}_6$ ), in which in the M1 site there is one atom of Co and in M2 site one atom of Ca, we increase cobalt content by 0.1 atoms per formula units up to the Co-rich end member  $\text{Co}_2\text{Si}_2\text{O}_6$ .

The process we follow for this synthesis at room temperature is a traditional ceramic route known as “solid state synthesis”, where stoichiometric ratios of oxides and  $\text{CaCO}_3$  carbonate are mixed and heated.

The starting material are powder of  $\text{Co}_3\text{O}_4$  (black)  $\text{CaCO}_3$  (white) and amorphous  $\text{SiO}_2$  (white), prepared according to the stoichiometry:



where  $x = 0, 0.1, 0.2, 0.3, 0.4, 0.5, 0.6, 0.7, 0.8, 0.9$  and  $1$ .

The starting materials are labelled as Co ( $x \cdot 10$ ): for instance Co6 means that the starting material has a bulk composition of  $\text{Ca}_{0.4}\text{Co}_{1.6}\text{Si}_2\text{O}_6$  with 0.6 of Co atoms p.f.u. in the M2 site of an hypothetical stoichiometric pyroxene.

A slight silica excess is added in all the samples. After weighting the oxides, they are mixed and crushed in an agate mortar with acetone. Several crushing cycles are done to obtain an homogeneous material. The sample is then reduced in pellets,

and heated within an alumina crucible in an electric furnace in air. The heating system increases the temperature with a step of 200°C/h up to the desired temperature of 1000°C, and then the samples are annealed for the selected time. At this temperature reduction of  $\text{Co}^{3+}$  to  $\text{Co}^{2+}$  and decarbonation occurs readily. The quenching is done by turning off the power and letting cool the samples. A sketch of the synthesis process is shown in figure 2.1.

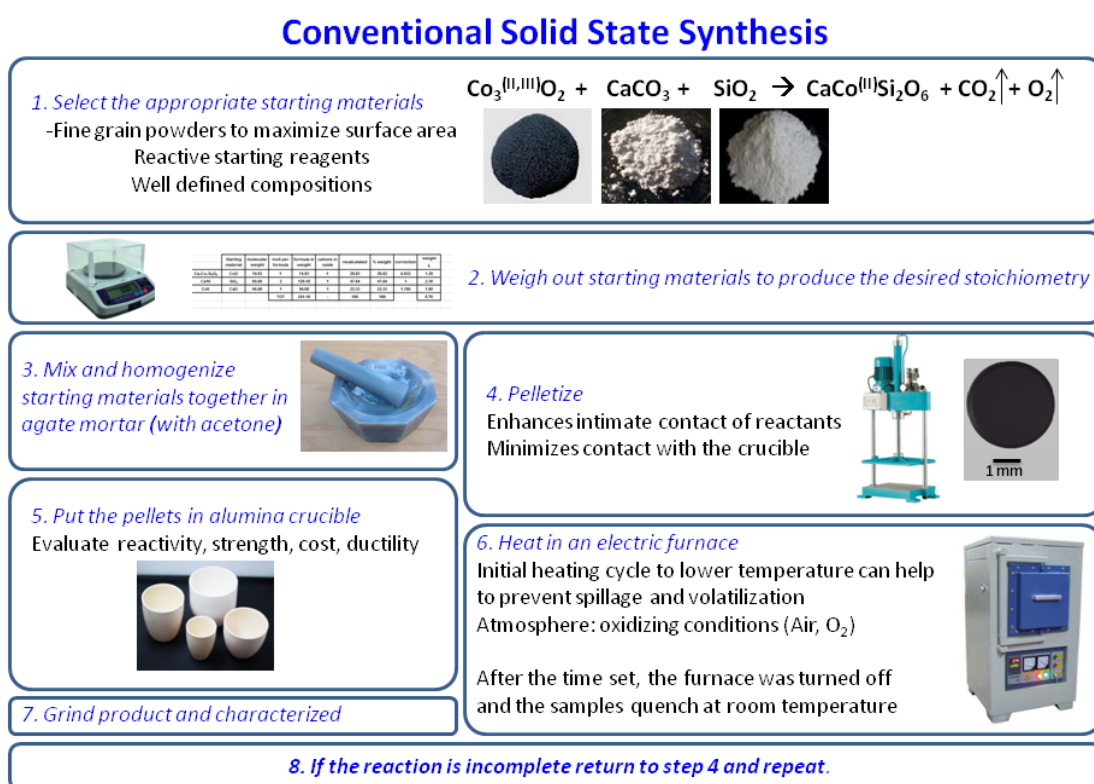


Fig. 2.1: Schematic process of the solid state synthesis

This procedure is followed in two set of runs, on all the samples, at the same temperature, but for 12 and 48 hours; then for two compositions, Co0 ( $\text{CaCoSi}_2\text{O}_6$ ) and Co5 ( $\text{Ca}_{0.5}\text{Co}_{0.5}\text{Si}_2\text{O}_6$ ) further heating is done at different time and temperature between 1000°C and 1200°C. In this second series of runs the heating employs the

same rate that in the first set, but cooling is done by quenching the sample in air. Therefore, in the second series the cooling lasts few minutes, while in the first series it lasts almost one night. An important implication is that in the first series slow cooling can enable the formation of phases stable at lower temperature; such formation is kinetically hindered by the fast cooling in the second series.















At the end of the experiments the samples are first optically examined. Most of the samples appear like synthesized pellets of different colour, from blue to pink, well separated from the alumina crucible. In two runs at 1200°C, from stoichiometric  $\text{CaCoSi}_2\text{O}_6$  for 3 and 24 hours, a blue glass is observed instead, which cannot be separated from the crucible, that has to be broken for further examination.
















At the optical microscope all the pellets look like an aggregate of hardly visible crystals.

The pellets are then crushed in an agate mortar and pulverized. A little chip for each sample is taken apart for SEM-EDS analysis.

Table 2.1 reports the name in which the samples are labelled, their nominal composition and the synthesis conditions, as well as the resulting assembling and the colorimetric parameters. After the synthesis, all run products were examined by X-Ray powder diffraction, SEM-EDS microprobe, Raman spectroscopy, UV-VIS and colorimetric analysis.



Sample	Co0	Co0	Co0	Co0	Co0	Co0	Co1	Co1	Co2	Co2	Co3	Co3	Co4	Co4
<b>temperature (°C)</b>	1000	1000	1000	1100	1100	1150	1000	1000	1000	1000	1000	1000	1000	1000
<b>time (h)</b>	12	48	120	3	96	24	12	48	12	48	12	48	12	48
<b>Nominal Ca content</b>	1	1	1	1	1	1	0.9	0.9	0.8	0.8	0.7	0.7	0.6	0.6
<b>Phase</b>	ak+px+ol+tr	ak+px+ol+tr	N.d.	N.d.	N.d.	Px+tr	ak+px+ol+tr	N.d.	ak+px+ol+tr	N.d.	ak+px+ol+tr	N.d.	ak+px+ol+tr	N.d.
<b>L*</b>	43.33	56.07	58.79	59.76	63.18	66.53	46.75	62.91	48.28	64.96	49.94	66.59	50.98	63.17
<b>a*</b>	9.17	13.9	18.74	27.16	25.54	25.35	9.07	14.16	8.77	16.67	9.87	18	10.48	18.59
<b>b*</b>	-36.5	-25.4	-15.6	-8.1	-10.2	-8.85	-32.5	-18.7	-28.3	-15.4	-25.2	-13.4	-20.9	-15.5
<b>Colour</b>														

Sample	Co5	Co5	Co5	Co5	Co5	Co6	Co6	Co7	Co7	Co8	Co8	Co9	Co9	Co10	Co10
<b>temperature (°C)</b>	1000	1000	1100	1100	1100	1000	1000	1000	1000	1000	1000	1000	1000	1000	1000
<b>time (h)</b>	12	48	3	24	96	12	48	12	48	12	48	12	48	12	48
<b>Nominal Ca content</b>	0.5	0.5	0.5	0.5	0.5	0.4	0.4	0.3	0.3	0.2	0.2	0.1	0.1	0	0
<b>Phase</b>	Px+ol+tr	Px+ol+tr	N.d.	N.d.	Px+ol+tr	Px+ol+tr	N.d.	Px+ol+tr	N.d.	Px+ol+tr	N.d.	Px+ol+tr	N.d.	Ol+tr	Ol+tr
<b>L*</b>	49.91	-	60.46	57.68	68.76	52.97	61.02	54.25	59.1	55.1	58.52	54.66	56.51	56.5	56.01
<b>a*</b>	13.89	-	19.64	23.91	18.7	18.42	18.69	20.58	19.2	21.12	19.41	21.74	20.07	20.5	20.59
<b>b*</b>	-19.9	-	-15.8	-14.8	-8.87	-21.7	-16.7	-22.8	-18.3	-23.1	-19.2	-23.5	-20.6	-21.5	-21.4
<b>Colour</b>															

Tab. 2.1: name of the samples, synthesis condition, phases obtained, colour coordinates and final colour for all the sample synthesized; Px: Ca,Co-pyroxene, ol: Co-olivine, tr: tridymite, ak: Co-akermanite.

## X-Ray Powder Diffraction

Powder diffraction patterns are recorded on the crushed samples, to determine which phases are present (qualitative analysis) and their relative abundance, through Rietveld refinement. A Bruker-AXS D8 Advance diffractometer (Bruker, Karlsruhe, Germany) equipped with an Si(Li) solid state detector is used. Intensity measurements are run at 40 kV and 30 mA and are taken using  $\text{CuK}\alpha$  radiation ( $\lambda = 1.54178 \text{ \AA}$ ) in steps of  $0.02^\circ$  over a  $2\theta$  range from  $10^\circ$  to  $80^\circ$ , with a counting time of 10 sec per step. The identification of the phases is done with the EVA software (Bruker), and ICDD database. Only Ca,Co-pyroxene, Co-olivine, Co-akermanite and a silica phase, likely tridymite, are found. The pyroxene is found in all but the Co10 sample (nominal composition  $\text{Co}_2\text{Si}_2\text{O}_6$ ), where olivine and tridymite are present instead; the tridymite is found in all runs, whereas Co-akermanite is present only from Co0 to Co4, i.e. in Ca-richer starting materials. Olivine instead is found by X-ray diffraction between Co2 and Co10, in Co-richer samples.

The identification of the silica phase is difficult as only one peak at  $2\theta = 23^\circ$  is present. Both cristobalite and tridymite can be fit, and the assignment to tridymite is given mostly from reference to previous papers (Masse et al., 1999) and to the silica phase diagram. Some tests are done also using cristobalite as silica phase in the Rietveld refinements, obtaining poorer fitting.

The determination of the unit cell parameters and the phase quantification is performed by the Rietveld method with the GSAS-EXPGUI software package by multiphase refinement (Larson and Von Dreele, 2000). Independent variables for the Rietveld refinement were: scale factor, zero point, nine coefficients of the shifted Chebyshev function to fit the background, unit cell dimensions, and separate scale

factors for the different phases. A pseudo-Voigt profile function was used, refining two Gaussian coefficients (Gv and Gw) and one Lorentzian (Lv). The Rietveld analysis was done using structural data from Kimata et al. (1983)(Kimata, 1983) for Co-akermanite, from Morimoto et al. (1974) (Morimoto et al., 1974) for Co-olivine, from Ghose et al. (1987) (Ghose et al., 1987) for Ca,Co-pyroxene and from Konnert et al. (1978) (Konnert and E, 1978) for tridymite. A good fit of the observed vs calculated patterns is always obtained, with  $\chi^2$  values varying between 3.1 and 1.5. Figure 2.2 shows a part (10-40  $2\theta$ ) of the X-Ray diffraction pattern for Co0, Co5 Co10 at 1000°C for 12 hours and an example of peak identification. The unit cell parameters and phase abundance are listed in Table 2.3. To note for all phases the relevant peaks are sharp, indicating sample homogeneity and low strain.

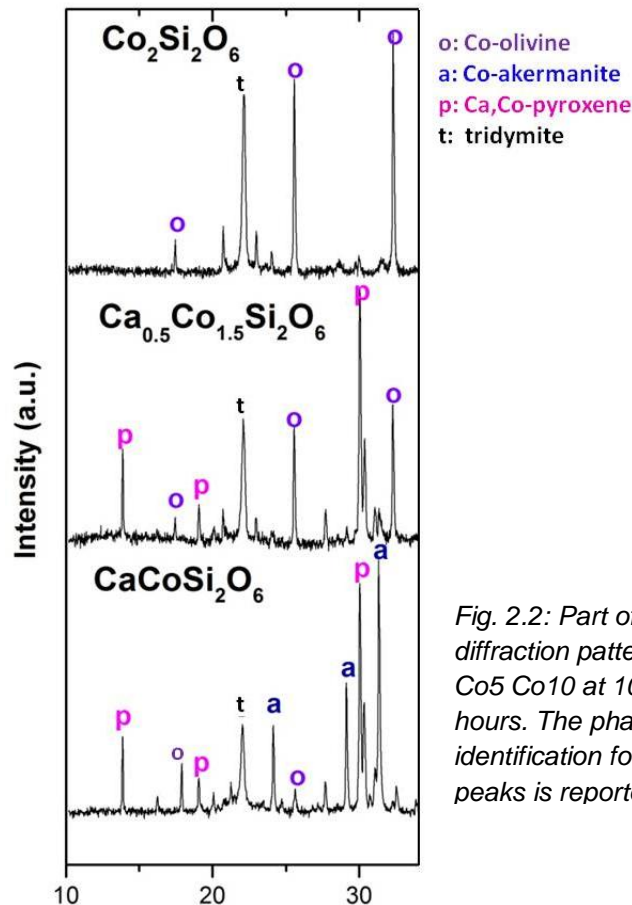


Fig. 2.2: Part of a X-Ray diffraction pattern for Co0, Co5 Co10 at 1000°C for 12 hours. The phase identification for the major peaks is reported.

	Sample	Co0	Co0	Co0	Co1	Co2	Co3	Co4	Co5	Co5	Co5	Co6	Co7	Co8	Co9	Co10	Co10
Synthesis condition	Co fraction (a.p.f.u.)	1	1	1	1.1	1.2	1.3	1.4	1.5	1.5	1.5	1.6	1.7	1.8	1.9	2	2
	Time (h)	12	48	24	12	12	12	12	12	48	96	12	12	12	12	12	48
	Temper (°C)	1000	1000	1150	1000	1000	1000	1000	1000	1000	1100	1000	1000	1000	1000	1000	1000
Pigment phase composition	<b>CaCoSi<sub>2</sub>O<sub>6</sub></b> wt%	<b>50.6</b>	<b>81.9</b>	<b>98.1</b>	<b>61.1</b>	<b>59.1</b>	<b>58.5</b>	<b>55.7</b>	<b>54.3</b>	<b>60.4</b>	<b>59.1</b>	<b>45.8</b>	<b>33.5</b>	<b>22.2</b>	<b>11.0</b>		
	a (Å)	9.791(1)	9.794(1)	9.798(1)	9.794(2)	9.794(1)	9.792(1)	9.788(1)	9.791(1)	9.796(2)	9.793(1)	9.783(2)	9.793(2)	9.790(3)	9.793(2)		
	b (Å)	8.961(1)	8.957(1)	8.961(2)	8.962(1)	8.963(2)	8.965(2)	8.961(2)	8.963(1)	8.967(2)	8.961(3)	8.958(1)	8.966(3)	8.963(2)	8.965(3)		
	c (Å)	5.241(1)	5.243(1)	5.246(1)	5.242(1)	5.242(1)	5.242(1)	5.239(2)	5.241(2)	5.243(1)	5.244(3)	5.240(1)	5.241(1)	5.241(1)	5.244(1)		
	β (°)	105.53(2)	105.50(2)	105.51(2)	105.55(2)	105.58(2)	105.60(3)	105.60(2)	105.64(2)	105.70(4)	105.70(2)	105.65(4)	105.67(4)	105.69(1)	105.74(4)		
	V (Å <sup>3</sup> )	443.03(1)	443.20(1)	443.78(3)	443.24(1)	443.28	443.18(1)	443.57(3)	443.94(3)	443.34(6)	443.02(4)	442.17(5)	443.07(7)	442.75(7)	442.83(7)		
	<b>Ca<sub>2</sub>CoSi<sub>2</sub>O<sub>7</sub></b> wt%	<b>34.9</b>	<b>13.9</b>		<b>26.8</b>	<b>19</b>	<b>9.6</b>	<b>6.7</b>									
	a (Å)	7.833(2)	7.828(2)		7.834(2)	7.836(2)	7.833(2)	7.833(2)									
	c (Å)	5.021(2)	5.022(3)		5.023(2)	5.023(3)	5.023(2)	5.018(2)									
	V (Å <sup>3</sup> )	308.11(3)	307.73(5)		308.30(5)	308.30(3)	308.21(5)	307.86(3)									
	<b>Co<sub>2</sub>SiO<sub>4</sub></b> wt%					<b>11</b>	<b>19.3</b>	<b>22.6</b>	<b>31.2</b>	<b>32.7</b>	<b>34.5</b>	<b>37.6</b>	<b>47</b>	<b>57.3</b>	<b>66.4</b>	<b>70.7</b>	<b>72.3</b>
	a (Å)					4.782(2)	4.784(3)	4.781(3)	4.783(2)	4.783(3)	4.784(4)	4.781(3)	4.783(2)	4.783(3)	4.783(4)	4.782(4)	4.781(2)
	b (Å)					10.311(4)	10.311(2)	10.312(4)	10.314(4)	10.320(2)	10.319(5)	10.308(4)	10.316(4)	10.314(5)	10.313(2)	10.302(5)	10.301(4)
	c (Å)					6.008(3)	6.007(3)	6.005(3)	6.008(3)	6.012(3)	6.011(3)	6.005(2)	6.009(4)	6.008(3)	6.008(2)	6.003(4)	6.002(2)
	V (Å <sup>3</sup> )					296.46(5)	296.41(4)	296.06(5)	296.33(7)	296.80(5)	296.74(5)	295.91(4)	296.48(7)	296.35(7)	296.34(3)	295.73(9)	295.59(8)
<b>SiO<sub>2</sub></b> wt%	<b>14.4</b>	<b>4.0</b>	<b>1.5</b>	<b>11.9</b>	<b>10.8</b>	<b>12.5</b>	<b>14.9</b>	<b>12.2</b>	<b>6.1</b>	<b>6.0</b>	<b>16.4</b>	<b>19.4</b>	<b>20.3</b>	<b>22.5</b>	<b>29.2</b>	<b>27.6</b>	
a (Å)	4.915(5)	4.959(5)	4.956(5)	4.923(5)	4.894(5)	4.942(5)	5.007(5)	4.993(5)	4.980(5)	4.983(5)	4.985(5)	4.988(7)	4.988(6)	4.989(7)	4.989(7)	4.997(7)	
c (Å)	7.279(6)	7.157(4)	7.118(3)	7.271(7)	7.352(6)	7.173(5)	6.977(6)	7.003(6)	6.988(6)	6.976(7)	6.992(5)	7.006(7)	6.992(5)	6.987(5)	6.983(7)	6.943(5)	
V (Å <sup>3</sup> )	175.85(4)	176.03(4)	174.85(5)	176.19(4)	176.11(3)	175.17(5)	174.89(4)	174.62(3)	173.31(5)	173.19(3)	173.77(1)	174.28(7)	173.98(7)	173.95(3)	173.81(5)	173.39(5)	

Tab.2.3: Cell parameters and wt fraction for some synthesized samples. The error for single measurement is reported in brackets. If the wt% fraction is less than 5% the Rietveld refinement doesn't reveal exactly the phase content.

In spite of the large changes in bulk composition, cell parameters of the synthesized phases change very little. This indicates, as confirmed by subsequent SEM-EDS results (following chapter), that the composition of the single phases doesn't change, and what varies is their abundance.

More in detail, in the Ca,Co-pyroxene phase the **a**, **b**, **c** parameters don't change significantly, but we found a small change in the  $\beta$  angle ( $105.53^\circ - 105.74^\circ$ ) and in volume ( $443.7 \text{ \AA}^3 - 442.8 \text{ \AA}^3$ ), which can be hardly related to changes in the bulk composition. Such small changes can be interpreted anticipating the results on the high pressure pyroxenes, whose composition is the same as the bulk starting materials (following chapter, Part III). From the plot in figure 2.3 it appears that the changes in  $\beta$  and volume for the low pressure series are little more than an experimental and compositional variation around a Co content of about 0.1 - 0.2 a.p.f.u in M2. These small quantities of Co in M2 indicate that some solid solution of Co in the M2 site is possible also at room pressure, as will be confirmed by EDS analysis.

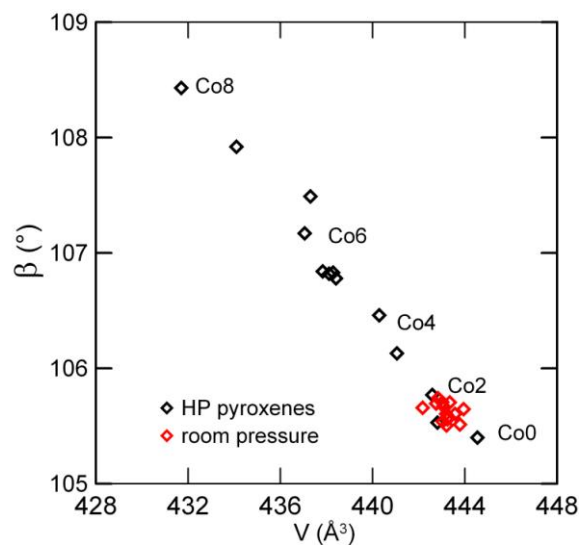


Fig. 2.3:  $\beta$  angle ( $^\circ$ ) vs volume value ( $\text{\AA}^3$ ) for the samples synthesized ad room pressure and high pressure. The variation of the parameters for the room pressure experiment correspond to a composition at about 0.1 – 0.2 of Co in M2 (a.p.f.u.).

As regards Co-akermanite cell parameters are the same within error in all runs, indicating an homogeneous composition. Co-olivine cell volume is slightly different (0.3% higher) in Ca-bearing samples respect to the sample Co10 where Ca is not present in the starting materials. In Ca-bearing samples, where olivine coexists with pyroxene, the cell volumes of Co-olivine are instead very similar. The likely explanation is the presence of some Ca in solid solution in the olivine structure, which increases the cell volume by its higher than Co cation radius. Again this will be confirmed by SEM-EDS analyses.

Despite the problem of the poor definition of the silica phase the Rietveld refinement is successful in determining the abundance.

Figure 2.3 shows the trend of the weight percentages of the various compounds as a function of Co content in the bulk composition. We observe the major presence of Co-akermanite in Ca-rich samples, that gradually disappeared while cobalt increased, leading to the formation of Co-olivine. We note that Ca,Co-pyroxene is present, during almost the entire series (except on Co10 where there's no Ca), but its abundance decreases drastically from Co5 onwards. The tridymite content increases in the Co-rich samples. It is also observed that in  $\text{CaCoSi}_2\text{O}_6$ , prolonging heating and increasing temperature the pyroxene phase is formed at expenses of Co-akermanite, that disappears in longer annealing (figure 2.4).

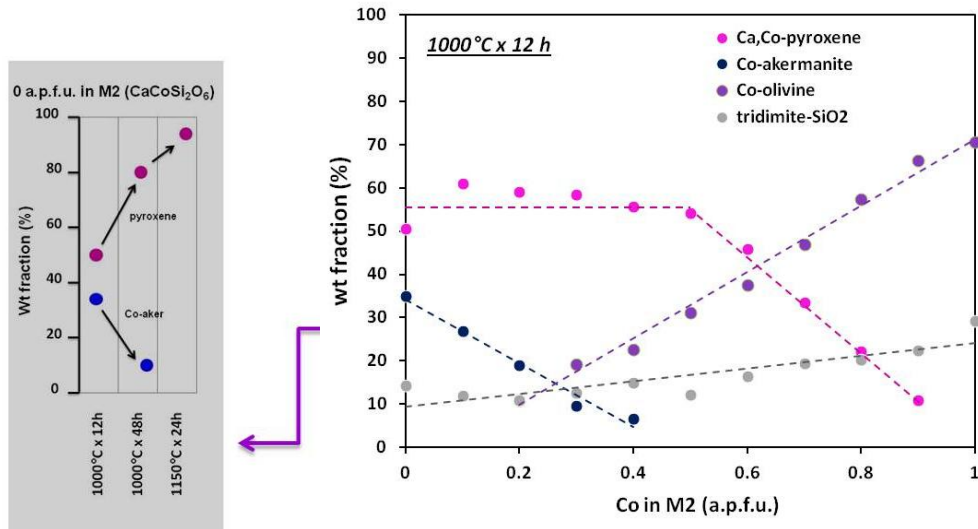


Fig. 2.4: wt fraction (%) of the phases vs Co content (a.p.f.u.) in M2. The sample CoO is annealed at different temperature and for different time: in this second step the pyroxene phase is formed at expenses of Co-akermanite, that disappears in longer annealing.

The assemblage obtained in the first series of runs and Ca-richer samples, does not represent equilibrium, as it can be shown by simple thermodynamic considerations. In a system with a T and P fixed the Gibbs' phase rules establishes that the degree of freedom of a system (f) is:

$$f = c - p + m + 0 (P, T)$$

where c is the number of the components, here 3 (CaO, CoO, SiO<sub>2</sub>), p the number of the phases obtained, and m the number of external parameters that have an effect on the state of the system. In our case m, at a pressure and temperature constant equals to 0. Obviously the phase freedom can be at minimum 0, in an invariant system.

In Ca-richer samples (see table 2.3) we have found four phases, - Ca,Co,pyroxenes, Co-olivine (found in Raman spectra), Co-akerminite and tridymite -, so that the freedom is -1, which indicates that at least one of the obtained phases is metastable.

In a ternary diagram CoO, CaO, SiO<sub>2</sub>, based on Mukhopadhyay et Jacob (1996) phase diagram, our bulk composition should lie in the ternary field included between Co<sub>2</sub>SiO<sub>4</sub>, SiO<sub>2</sub> and a phase rich in Ca and Co, like pyroxene or Co-akermanite. The suggestion is that one either Co-akermanite and CaCO-pyroxene are not stable at the experimental condition, and evidence is that the metastable phase is Co-akermanite: while increasing annealing time at constant temperature the CaCo-pyroxene increases gradually at the expense of the Co-akermanite. The same happens if we increase temperature (table 2.3).

The single pyroxene phase, which is the final product of longer annealing and higher temperature is a stable phase at least above 1000°C for the CaCoSi<sub>2</sub>O<sub>6</sub> starting materials. Co-akermanite can be a residual of a stability field that is present a lower temperature during the slow cooling in the furnace or simply a metastable phase formed during the first step of the synthesis.

To note, Co-akermanite is found in the synthesis of CaCoSi<sub>2</sub>O<sub>6</sub> pyroxene also by Masse et al. (1999), who did not clarify the point of metastability.

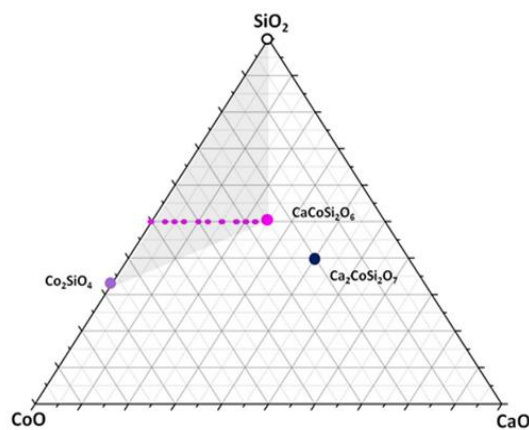


Fig. 2.11: ternary diagram of the studied samples. The composition of the studied phases is shown, as well as that of the starting materials (small dots). Note that the starting materials fall into a ternary field, determined by Co<sub>2</sub>SiO<sub>4</sub>-CaCoSi<sub>2</sub>O<sub>6</sub>-SiO<sub>2</sub>, or Co<sub>2</sub>SiO<sub>4</sub>-Ca<sub>2</sub>CoSi<sub>2</sub>O<sub>7</sub>-SiO<sub>2</sub>. In the former case stoichiometric CaCoSi<sub>2</sub>O<sub>6</sub>, would give a pyroxene only assemblage.



## Scanning Electron Microscopy and EDS microanalysis

The size and the shape of the different phases are observed through SEM backscattered images, and their composition is determined with microprobe EDS analysis. SEM-EDS analyses are performed with a Jeol 6400 Scanning Electron Microscope equipped with an Oxford EDS (Energy Dispersive System). Operating conditions are 20 kV and 1.2 mA current, and analyses are taken using  $\sim 1\ \mu\text{m}$  beam diameter and 75 sec counting time. Cobalt is used as a standard. An average of about 15 spots per sample is obtained. The images are taken under low vacuum conditions. The samples are glued in epoxy resin and polished, to make them flat and covered with a high-conductance thin film (graphite film) to avoid charging effects. Analyses of the room pressure runs are done only on samples with bulk composition Co<sub>0</sub>, Co<sub>5</sub> and Co<sub>10</sub>.

Figures from 2.4 to 2.11 show backscattered electron (BSE) images. The different grey tone is related to the average atomic number (Z) of the specimen: the darker corresponds to the lower number of backscattered electron, i.e. to the lower mean atomic number; the mean atomic numbers Z for the phases found in our syntheses are: Z = 14.5 for Co-olivine, Z = 10.6 for SiO<sub>2</sub>, Z = 12.7 for CaCoSi<sub>2</sub>O<sub>6</sub> and Z=12.9 for Co-ackermanite. Co-ackermanite and pyroxene are hardly distinguishable in backscattered electron images, being their average atomic number similar.

Only in few cases they reached 5-10  $\mu\text{m}$ . Large silica nuclei are present, with reaction rims of clinopyroxene, olivine and Co-akermanite.

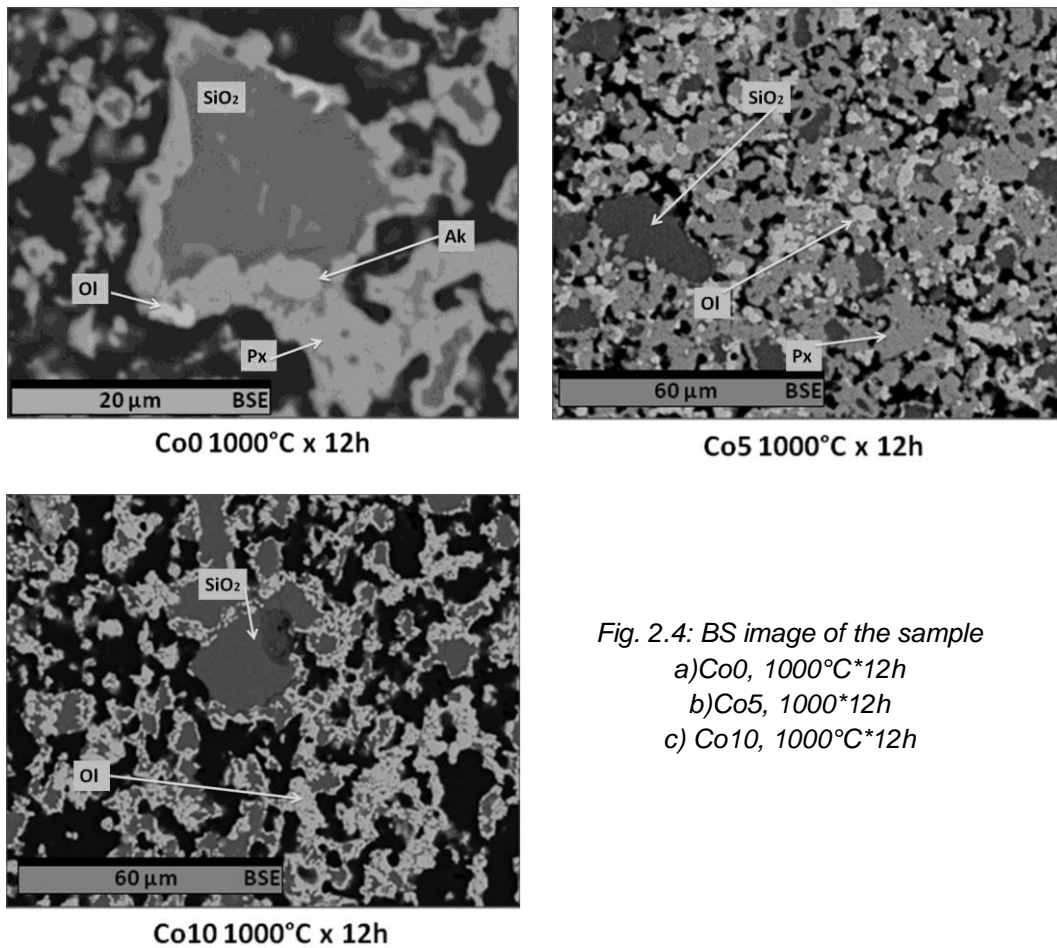
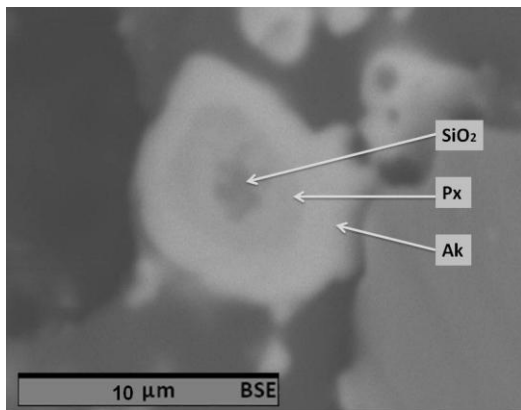


*Fig. 2.4: BS image of the sample  
 a) Co0, 1000°C\*12h  
 b) Co5, 1000\*12h  
 c) Co10, 1000°C\*12h*

In the first series of runs a common feature is that they are microcrystalline aggregates and mostly anhedral: crystals sized of the order of few microns; only in few cases they reached 5-10 µm. Large silica nuclei are present, with reaction rims of clinopyroxene, olivine and Co-akermanite

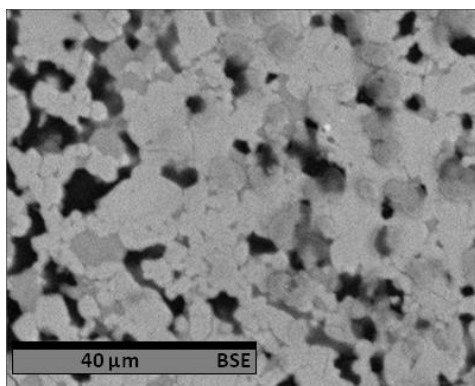
This situation is texturally indicative of a non-equilibrium, and it is mostly found in Co0. Further evidence of the non-equilibrium are rounded terminations of the crystals, or reaction rims. In figure 2.4 a reaction rim showing silica at the core, surrounded by Co pyroxene, mantled by Co-akermanite, is shown.



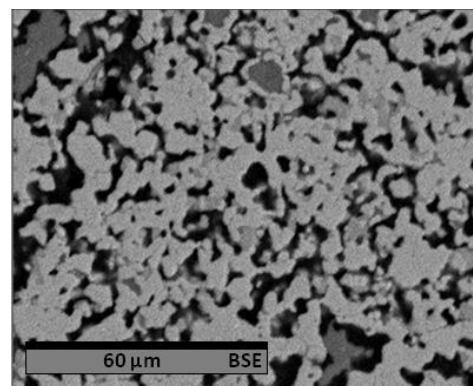
CoO 1000°C x 12h

*Fig. 2.5 : BSE image of a small crystal in a no-equilibrium situation: a silica nucleus is still reacting, showing the formation of a pyroxene and Co-akermanite phases.*

The above non-equilibrium textures are indicative that at the temperature of 1000°C for 12 hours the reaction is not completed and thermodynamic equilibrium is not reached. Increasing heating time and temperature larger crystals and more homogeneous samples with similar crystal size appear, like it is shown in figure 2.5: the crystals are still tiny, sized at maximum 10 microns, but become euhedral and reaction rims disappear, as well as large tridymite crystals.



CoO 1100°C x 96h



CoO 1150°C x 24h

*Fig. 2.6: BS image of the sample CoO: a)1100°C\*96h and b)1150\*24h*

In fact we can see that the silica nuclei gradually reduced when temperature or time of the synthesis increased, although an excess silica was always present, related to an excess of SiO<sub>2</sub> in the starting material.

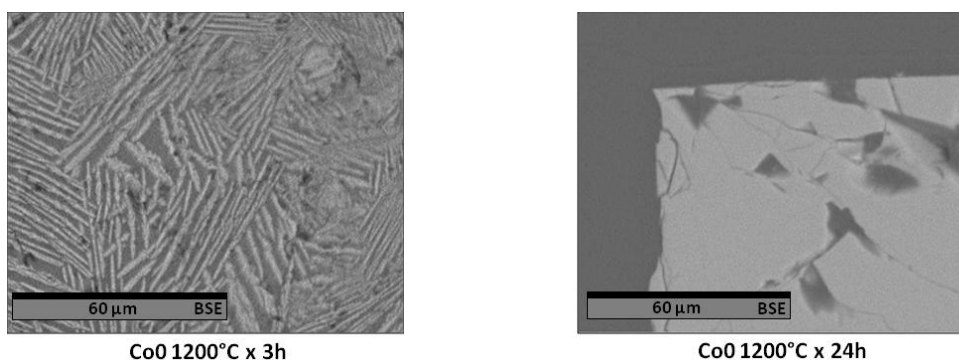


Fig. 2.7: BS image of the sample Co0: a)1000°C\*12h and b)1000\*48h

As previously said, in the synthesis carried out at 1200°C, the samples are partially or totally molten after 3 and 24 hours annealing. The melting of samples caused a gradual leaching of cobalt that dissolved into the glass, changing the coordination in tetrahedral and giving a deep blue-black colour (figure 2.7).

Chemical analyses are performed with EDS only for Co0, Co5 and Co10 samples (table 2.4). The SEM-EDS analysis confirms the phases found by XRD.

A major analytical problem is the point analysis on overlapping crystals, due to their dimension close to the beam analyzed volume (few μm<sup>3</sup>). Analysis whose stoichiometry cannot be classified in one of the reported phases are therefore discarded.

CaCo-pyroxene shows a different composition between samples Co0 and Co5. In fact in Co5 samples a Co-richer pyroxene (Ca<sub>0.9</sub>Co<sub>1.1</sub>Si<sub>2</sub>O<sub>6</sub>), coexisting with Co-olivine and tridymite in agreement of the suggestion of the powder XRD analysis of a slightly Co-richer solid solution at room pressure. As regards Co-olivine a small

Ca content (0.004 Ca atoms p.f.u.) is found in the analysis of the Co5 samples confirming the XRD diffraction results.

Sample	Co0	Co0	Co0	Co0	Co0	Co0	Co5	Co5	Co5	Co5	Co5	Co10	Co10
<b>Co nom.</b>	1	1	1	1	1	1	1.5	1.5	1.5	1.5	1.5	2	2
<b>Time (h)</b>	12	48	120	3	96	24	12	48	3	24	96	12	48
<b>Temp (°C)</b>	1000	1000	1000	1100	1100	1150	1000	1000	1100	1100	1100	1000	1000
<b>n° analysis</b>	2	3	2	5	6	4	6	6	5	5	5		
<b>Cation on the basis of 6 O atoms per formula units (CaCoSi<sub>2</sub>O<sub>6</sub>)</b>													
<b>Ca</b>	1.04	0.96	0.98	0.95	0.93	1.03	0.88	0.85	0.8	0.9	0.83		
<b>Co</b>	1.02	1.02	1.06	0.94	1.07	1.02	1.12	1.15	1.14	1.1	1.15		
<b>Si</b>	1.97	2.04	1.96	1.99	1.98	1.98	1.99	1.98	2	1.99	1.98		
<b>Total</b>	4.03	4.02	4.00	3.88	3.98	4.03	3.99	3.98	3.94	3.99	3.96		
<b>Cation on the basis of 7 O atoms per formula units (Ca<sub>2</sub>CoSi<sub>2</sub>O<sub>7</sub>)</b>													
<b>n° analysis</b>		1											
<b>Ca</b>		1.91											
<b>Co</b>	n.a.	1.03											
<b>Si</b>		2.01											
<b>Total</b>		4.95											
<b>Cation on the basis of 4 O atoms per formula units (Co<sub>2</sub>SiO<sub>4</sub>)</b>													
<b>n° analysis</b>							3	2	2	1	5	3	4
<b>Co</b>							2	1.98	1.95	1.96	2.04	2	1.99
<b>Ca</b>	n.a.	n.a.					n.d	0.01	0.02	0.01	0.01		
<b>Si</b>							1.99	1.98	1.99	2.01	2	1.99	1.99
<b>Total</b>							3.99	3.97	3.96	3.98	4.05	3.99	3.98

Table 2.4 shows chemical analysis made on the samples Co0, Co5 and Co10, at different temperature and time. Estimated error is on the last digit.

## Raman Spectroscopy

Raman spectroscopy is performed on the samples synthesized at room pressure to determine the phases present. By this respect it is complementary to X-ray phase determination. The information specific for Raman spectroscopy, i.e. an observation on roto-vibrational modes of molecules to identify phases but also to analyze the order/disorder into the crystal structure will be fully exploited in the analysis of the high pressure samples.

Raman spectroscopy is performed on powdered samples using a Jobin-Yvon Horiba LabRam microRaman apparatus, with spatial resolution of  $\sim 2 \mu\text{m}$  and a spectral resolution of  $\sim 2\text{cm}^{-1}$ . The 632.8 nm line of an He-Ne laser is used as the excitation. A filter wheel is used to reduce the laser power from 20 mW to 1 mW or less on the sample. The frequency calibration is performed against the Raman peak of silicon. On each sample, an average of five Raman spectra are taken. The peak positions are obtained from baseline-corrected spectra by least-squares analysis using the computer program Labspec (HORIBA). A Lorentzian profile is used in the peak profile analysis.

Figure 2.8 shows Raman spectra of the samples synthesized at 1000°C for 12 hours. The spectra reveal sample heterogeneity: we find different peaks ascribable to different phases in the same spectrum. This is due to the presence of crystals sized close or less the area excited by laser spot, which, taking into account the penetration of the laser by few microns, is at least  $5\text{-}10 \mu\text{m}^3$ : as the crystals dimension of the room pressure runs are generally smaller the information is that of a sum of several crystals. Figure 2.6 shows a sketch of the area included in Raman analysis.

It should be also noted that the intensity of the peaks from the different phases vary locally, and has no meaning of average compositional content, differently from the IR spectroscopy.

To analyze the obtained spectra single phase standards are taken, and used to separate the different phases (figure 2.8 b). The most intense peaks for each phase are reported in table 2.5.

Raman data confirm the presence of the phases found by XRD, but also show the presence of Co-olivine in the Co0 sample. The phases present in the synthesis from the Co0 starting material of the first series of runs are the Co-akermanite, Ca,Co-pyroxene, Co-olivine and tridymite. The observation of Co-olivine in the Ca0 sample completes the XRD and SEM data: Rietveld refinement doesn't reveal the presence of Co-olivine being this phase present in a small quantities (<5% in weight).

In the first series we find in all samples except in Co10 the typical pyroxene pattern: the three peaks at 300-400  $\text{cm}^{-1}$  and the two intense peaks, one at 660  $\text{cm}^{-1}$  and the other at 1010  $\text{cm}^{-1}$ , which will be redetailed in the high pressure paragraph.

The peak near 900  $\text{cm}^{-1}$ , ascribable to Co-akermanite gradually decreases its intensity, disappearing at the composition of Co5, while the double peak at 810 and 840  $\text{cm}^{-1}$  ascribable to the Co-olivine is clearly visible in all the series.

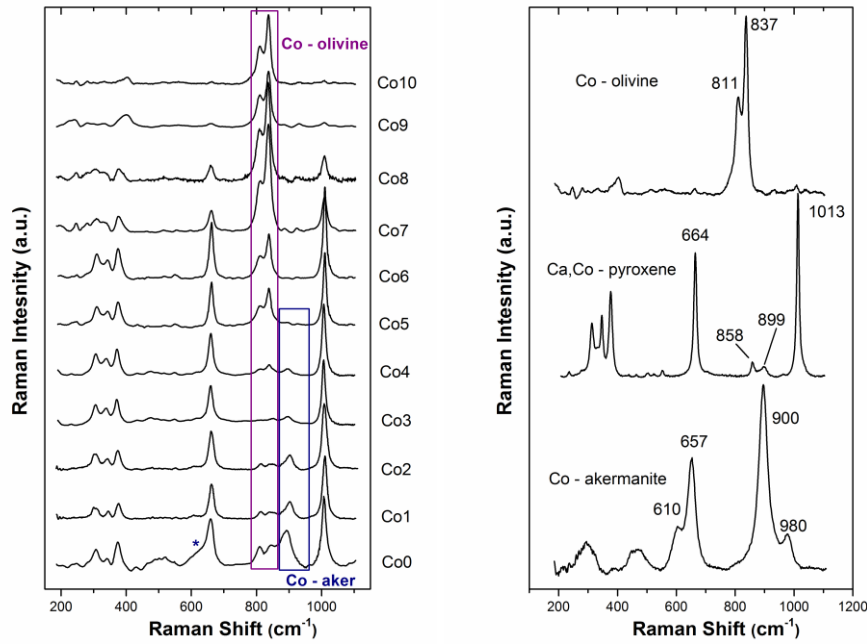


Fig. 2.8: a) Raman spectra of samples synthesized at 1000°C for 12 hours, b) standard used for the identification of the phases

Sample	Temperature (°C)	Time (h)	V <sub>1</sub>	V <sub>2</sub>	V <sub>3</sub>	V <sub>4</sub>	V <sub>5</sub>	V <sub>6</sub>	V <sub>7</sub>	V <sub>8</sub>
			Ca,Co-px	Ca,Co-px	Ca,Co-px	Ca,Co-px	Co-olivine	Co-olivine	Co-akerm	Ca,Co-px
Co0	1000	12	306.1	344.9	375.4	659.3	811.4	840.3	899.7	1009.7
Co0	1000	48	308.2	342.1	375.0	661.0	812.6	840.1	901.3	1009.4
Co0	1000	120	310.2	343.1	376.8	665.5	810.3	840.5	897.6	1010.4
Co0	1100	3	312.7	340.5	377.8	664.7	812.5	840.1	895.1	1013.2
Co0	1100	96	311.7	345.6	380.2	665.2	814.3	838.3	891.0	1011.2
Co0	1150	24	311.0	345.3	378.2	662.9	810.2	839.0	893.2	1011.5
Co1	1000	12	305.0	344.6	376.7	662.0	809.9	838.9	901.1	1010.0
Co2	1000	12	305.7	342.0	374.5	661.2	811.7	838.3	900.6	1008.8
Co3	1000	12	306.0	337.6	371.2	658.9	810.5	840.7	895.5	1006.4
Co4	1000	12	306.4	337.9	372.3	659.5	808.0	839.9	894.6	1007.0
Co5	1000	12	311.1	341.9	376.0	661.5	810.2	838.0		1009.8
Co5	1000	48	313.4	343.3	378.9	662.6	811.5	838.4		1010.5
Co5	1100	3	311.5	345.0	380.4	664.8	812.7	839.5		1012.9
Co5	1100	24	311.8	344.8	379.9	665.1	812.8	839.1		1013.2
Co5	1100	96	313.8	348.8	379.9	664.9	812.7	839.1		1013.2
Co6	1000	12	311.1	342.0	375.9	661.6	811.1	838.3		1009.9
Co7	1000	12	309.5	340.7	379.1	660.7	810.2	836.5		1009.1
Co8	1000	12	308.2	336.0	380.2	660.0	809.2	835.9		1008.6
Co9	1000	12					810.4	837.0		
Co10	1000	12					811.0	837.1		
Co10	1000	48					810.5	836.8		

Table 2.5 peak position of the fitted Raman spectra with some attribution of the peaks. Error is estimated  $\pm 0.5$



In all runs the peak position of the phases does not change significantly, varying only their intensity: this confirms the observation of almost constant composition of the phases by XRD and SEM-EDS.

In figure 2.9 a the Raman spectra of the second series of runs on the sample Co0 are reported. The presence of characteristic peaks of the pyroxene is evident (the triplet between 300-400  $\text{cm}^{-1}$ , 660 and 1013  $\text{cm}^{-1}$ ), but at the same time are visible peaks ascribable to Co-akermanite (900  $\text{cm}^{-1}$ ) and Co-olivine (811 and 837  $\text{cm}^{-1}$ ). Increasing the annealing time, (1000°C x 120h) Co-olivine disappears but peaks of Co-akermanite are still present. Raising the temperature to 1100 °C, a typical spectrum of the pyroxene is observed, but two small peaks at about 620  $\text{cm}^{-1}$  and 1000  $\text{cm}^{-1}$  ascribable to Co-akermanite are also found. In the synthesis carried out at T = 1100° C for 96 hours and T = 1150°C for 24 hours the Raman spectrum reveals the presence of Ca,Co-pyroxene only. At 1200°C the sample begins to melt. The Raman spectrum reveals the coexistence of glass and pyroxene, with larger peaks, due to inherent structural disorder.

The samples Co5 and Co10 show Co-olivine and tridymite in all runs, together with clinopyroxene in Co5 (figure 2.9 b,c).

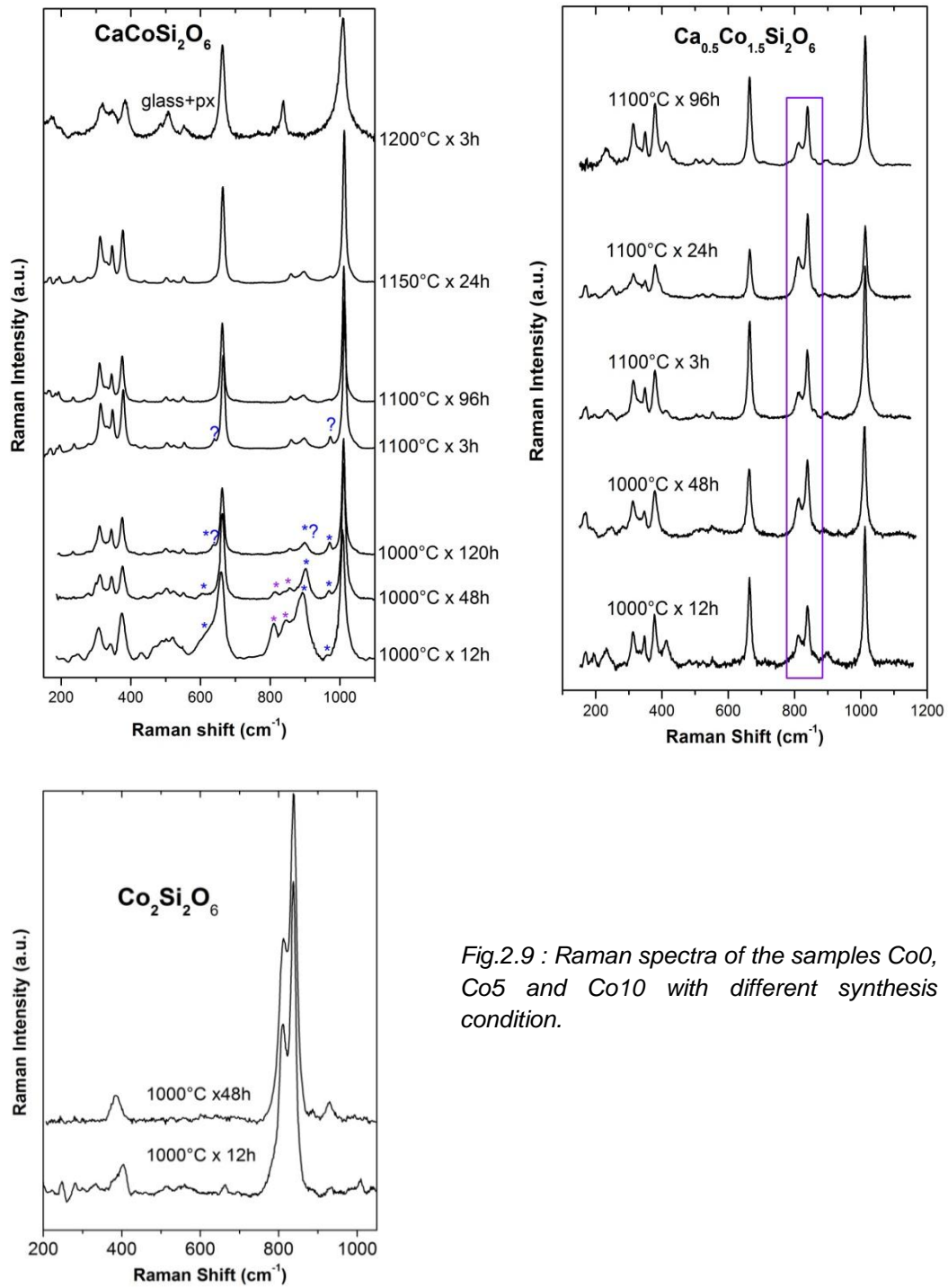


Fig.2.9 : Raman spectra of the samples Co0, Co5 and Co10 with different synthesis condition.

## Colour coordinates

The colour of a pigment provides the basis for any interest in manufacturing, but also conveys important analytical information.

Colour is the sensation that we perceive visually from the refraction or reflection of light on the surface of objects. Colour is light — as it is strictly related to it — and depending on the type of light (illuminating or luminous stimulus) we see one colour or another. Light is highly variable and so too is colour, to a certain extent.

Pigments absorb a part of the radiations of the incident light and reflect another, which reaches the eye of the observers, making them experience the sensation of colour. For instance, the dark colour of a pigment is almost entirely due to the fact that incident radiation is absorbed almost completely in the visible spectrum.

The purpose of colour analysis is to measure chromatic characteristics of the pigments in an objective way. This is done according to CIE standards.

An organization called CIE (Commission International de l'Eclairage) determines standard values that are used worldwide to measure colour. The values use by CIE are called  $L^*$ ,  $a^*$  and  $b^*$  colour coordinates and the colour measurement method is called CIELAB.

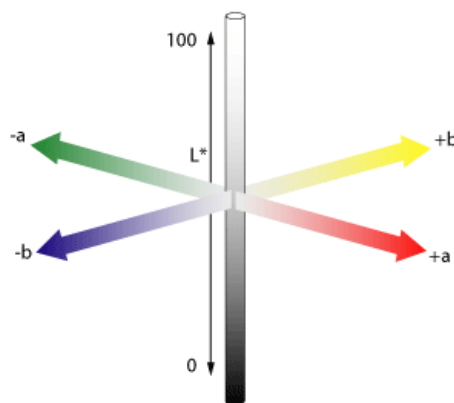


Fig. 2.10: CIELAB coordinate system

$L^*a^*b^*$  colour parameters can be measured with a spectrophotometer using a standard lighting C, following the CIE- $L^*a^*b^*$  colorimetric method.

The field of blue colour is mainly governed by the parameter  $b^*$ : the more negative the  $b^*$  value is, the bluer the colour hue results. On the other hand, the coordinate  $L^*$  gives us the lightness of the pigment (the higher  $L^*$ , means lighter hue); it is also an indirect measurement of the brightness or intensity of the pigment (the lower  $L^*$  means the brighter or more intense the colour). In the analysis of our syntheses colorimetric analysis enables to assess the changes in colour and relate the colour components the composition of the different phases. The final colour can also be calculated from colour components, and represented as done in table 3.1.

The products of all the room pressure syntheses are measured with a colorimeter (spectrophotometer) with  $d_i/8$  geometry (diffuse component seen at  $8^\circ$  from the normal to the sample), sampling step by 20 nm, measured between 360 and 780nm. The colorimetric calculation is done after spectral reflection measurement with the standard CIE 1964 observer and Daylight.

The colour parameters ( $L^*a^*b^*$ ) of our samples are shown in Table 3.1.

In our samples the colour comes only from the Co-bearing phases, i.e. not from tridymite. The colours of the pure phases are deep blue for Co-ackermanite, ( $\text{Ca}_2\text{CoSi}_2\text{O}_7$ ) and pink for pyroxene ( $\text{CaCoSi}_2\text{O}_6$ ) and olivine ( $\text{Co}_2\text{SiO}_4$ ). Colorimetric analysis shows that some difference is present between the two pink phases: pure olivine, found in the Co10 synthesis shows lower luminance,  $a^*$  and  $b^*$  components vs pure  $\text{CaCoSi}_2\text{O}_6$  clinopyroxene found in the longest synthesis at  $1150^\circ\text{C}$ . Colour coordinates of single phase pyroxene were  $25 < a^* < 27$  and  $-10 < b^* < -8$ . For the single Co-olivine phase the  $a^*$  parameters has a similar value, but  $b^*$  was more

negative ( $b^*$  about -20). Smaller value in  $b^*$  parameters indicate a more blue-violet hue. In fact the sample Co10 made by olivine exhibited an achromatic violet colour (very low  $a^*$  and  $b^*$  values), and the resulting colour of a single olivine phase appeared more violet respect to the pyroxene.

By mixing the different phases, the resulting colour reflects both colour efficiency and phase abundance. The most apparent colour changes are those in the first series runs from the (Co0)  $\text{CaCoSi}_2\text{O}_6$  bulk composition to the (Co10),  $\text{Co}_2\text{Si}_2\text{O}_6$  where a change from blue to pink is observed. This is due to the presence of the Co-akermanite in the samples Ca-richer (from Co0 to Co5), that produced blue colour hues ( $b^*$  values around 36).

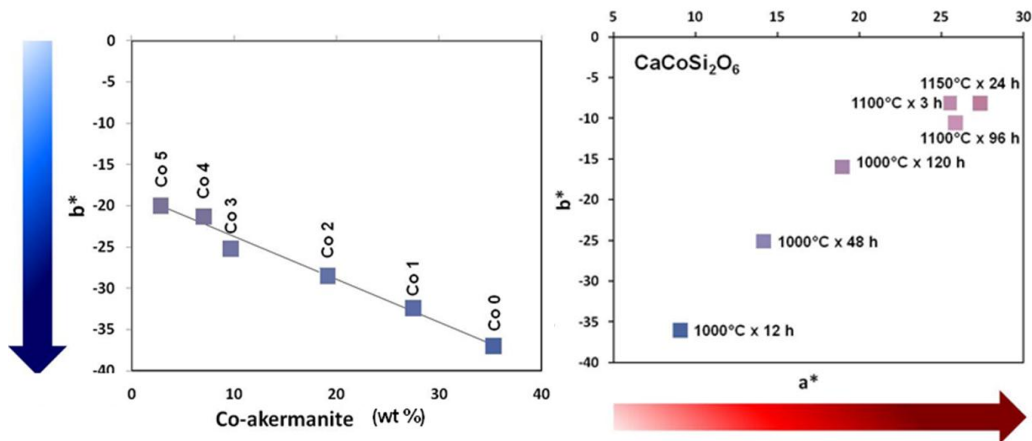


Fig. 2.11 a) shows the  $b^*$  parameters vs Co-akermanite content (wt% fraction) for the samples from Co0 to Co5 (1000°C for 12 hours) b)  $a^*$  vs  $b^*$  colour parameters for the samples Co0 annealing at different temperature and time

In figures 2.11 a the colorimetric parameters  $b^*$  vs Co-akermanite content obtained by Rietveld refinement are reported. The Co-akermanite is never present as dominating phase, but the colour for Co0 is deep blue, very similar to the colour of pure ackermanite. This occurs as cobalt in tetrahedral coordination has a more

intense hiding power respect to that in octahedral coordination, and the presence/absence of the Co-akermanite dominates the resulting colour, giving a deep blue colour even if it is present in small quantities (i.e. in fig 2.11a, samples Co4 has almost a blue hue even if Co-akermanite don't reach 7% in weight. As shown in fig 2.11 the akermanite  $b^*$  component is proportional to the phase content. In this case colorimetric analysis can become an analytical technique, to determine even small quantities of ackermanite.

In figure 2.11 b for the composition Co0  $a^*$  vs  $b^*$  parameters are reported after different annealing time and temperature. In the samples belonging to the second series the linear change in the  $a^*$  component can be interpreted as indicative to a continuous decrease and final disappearance of the Co-akermanite, as confirmed by Rietveld refinement results. When Co-akermanite disappeared and the Co is present only in octahedral coordination the final colour is a bright pink, as we can see in the sample Co0 annealed at a temperature  $T = >1100^\circ\text{C}$ .

This result has an important consequence on the possible use of  $\text{CaCoSi}_2\text{O}_6$  pyroxene as a pigment. For the synthesis of a pure  $\text{CaCoSi}_2\text{O}_6$  pyroxene pigment, showing the purest colour, the formation of metastable Co-ackermanite must be avoided, and this could be obtained only at temperature not lower than  $1100^\circ\text{C}$  or by very long annealing time at  $T = 1000^\circ\text{C}$ .

As shown in figure 2.12 strong differences exist between the two runs at  $1000^\circ\text{C}$ , after 12 and 48 hours, mostly due in the Ca-rich part to a different Co-akermanite content, but the Co-akermanite content is not the only factor affecting colour changes. Some difference still exists also in the Ca-poorer part of the join, likely due to different pyroxene and olivine ratio in the two series. To note the decrease with

Ca in the L\* value between Co4 and Co10, is related to the decreased pyroxene content, as L\* parameter is higher in Co-pyroxene respect to Co-olivine (66 vs 56).

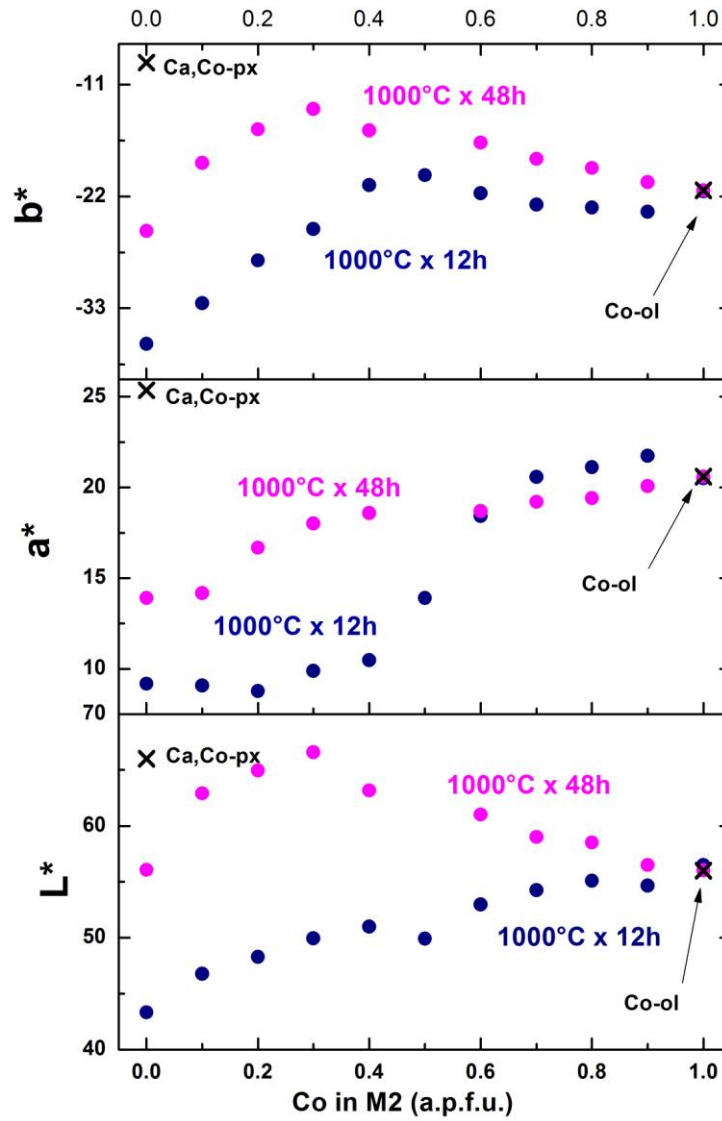


Fig. 2.12:  $L^*$ ,  $a^*$  and  $b^*$  parameters vs Co (a.p.f.u.) content in M2. Blue dots are referred to samples annealed at 1000°C for 12h, the pink ones to those annealed at 1000°C for 48h. The black cross represent the value for single phase  $\text{CaCoSi}_2\text{O}_6$  and Co-olivine.

Optical absorption analysis (UV-VIS-NIR)

Colourimetric analysis measures the resulting colour of the studied samples, but the cause of the different colour, that resides in electronic transitions, can be investigated by ultraviolet–visible spectroscopy (UV-VIS). This spectroscopy measures light absorption in the ultraviolet-visible spectral region. In this region of the electromagnetic spectrum, atoms undergo transitions of the outer electrons from the ground to an excited state, absorbing light on the required frequency.

The transitions that promote absorption in the visible range (380-720 nm) directly affect the perceived colour of the elements involved. Most often transitions in the visible range are present in transition metal. Electronic spectra of transition metal compounds in the visible region originate when electrons are excited by light to occupy incompletely filled 3d orbital of different energy levels within the transition metal ion.

The origin of the splitting of the 3d energy levels can be described by the crystal field theory. This theory treats the transition metal ion in a crystalline environment, as though it was subjected to purely electrostatic interaction with surrounding anions which are approximated as point negative charges. Each transition metal has five 3d orbitals which are energetically equivalent in a spherical environment such as a hypothetical gaseous free ion. However when the cations are surrounded by ligands in a crystal structure, the relative energies of the 3d orbitals change, depending on the symmetry of the ligand environment which defines the geometry of the coordination site. In the case of a tetrahedral regular environment, the energies of the five 3d orbitals split in two  $e_g$  and three  $t_2$  orbitals; in a regular octahedron the split occurs between three  $t_2$  and two  $e_g$  orbitals. The energy separation between the



$t_{2g}$  and  $e_g$  levels is the crystal field splitting. The energy of the transition can be obtained directly from the spectra of the transition metal-bearing phases in the visible and near infrared regions measuring the specific absorption energy.

In  $\text{Co}^{2+}$  we have seven 3d electrons. According to the Hund rule they distribute in separate orbitals. In  $\text{Co}^{2+}$  which is an high spin configuration two 3d orbitals have two electron each and three for one each.

For tetrahedral coordination the ground state, i.e that with lower energy, has four electrons in the two filled  $e_g$  orbitals, and the remaining three in each of the  $t_2$  orbitals. In octahedral coordination five electrons are in the three orbitals of the  $t_2$  split level, and two in each of the  $e_g$  orbitals. A transition may occur for instance promoting in a tetrahedrally coordinated Co one of the electrons in  $e_g$  to  $t_2$ , or one in  $t_2$  to  $e_g$  in octahedrally coordinated cobalt.

The energy level diagram of  $\text{Co}^{2+}$  both in octahedral and tetrahedral coordination is reported in figure 2.13. Three spin-allowed transitions for  $\text{Co}^{2+}$  ( $3d^7$  configuration) can be predicted, both in regular octahedral and tetrahedral ligand fields, but in our phases  $\text{Co}^{2+}$  is never in a regular polyhedron, and the orbitals further split in sublevels, depending on the site geometry, so that for each transition we have several peaks. Further complexities arise from other electron transitions, like spin forbidden ones or vibronic transition in molecules. The intensity of the related absorptions in these two cases is however much lower than in spin allowed ones.

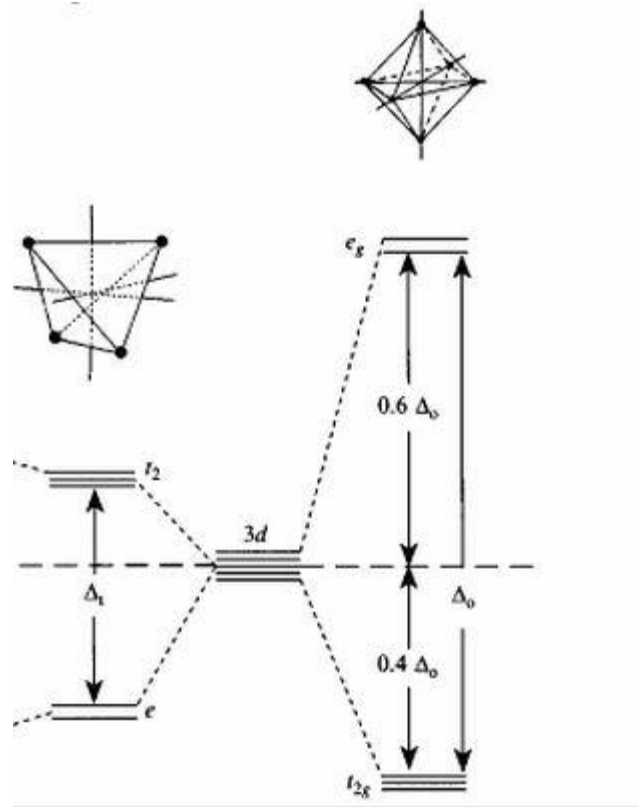


Figure 2.12. Cristal field splitting of transition metal 3d orbital in tetrahedral (4-fold) and octahedral (6-fold) coordination (Burns, 1993)

Optical absorption measurements are performed over the 200-800 nm range by means of a Varian 2390 spectrophotometer (resolution 1 nm). Pellets are then prepared by mixing 10-15 mg of the powdered compounds with 100 mg of KBr powders. The recorded spectra are fitted with Gaussian components using the Origin Pro 8 software .

The absorption spectra of this work samples are rather difficult to interpret due to the high number of the coexisting phases and absorption peaks. Figure 2.15 showed the optical spectra of the samples synthesized at 1000°C for 12 hours, where Co is present in different phases, and sites: Co is both in tetrahedral (Co-akermanite) and

octahedral (Co-olivine and Ca,Co-pyroxene) coordination, and we have two octahedral sites for pyroxene and two for olivine.

At first therefore we try to identify the electronic transitions that occur in the single phases of Co-akermanite, Co-olivine and Ca,Co-pyroxene (figure 2.14). They are at first measured separately, using for Co-olivine the sample Co10, for CaCo-pyroxene the Co0 at 1100°C and for Co-akermanite a synthesis of a pure phase (courtesy of Dondi). The interpretation of the optical absorption spectra in the three phases is done with reference to previous literature. In olivine we have three spin allowed transitions, but only two give absorption in the visible range. One [ ${}^4T_1(F) \rightarrow A_1(F)$ ], in the electron configuration nomenclature] is present in visible spectrum as a very weak shoulder in red region, and the other is a major one [ ${}^4T_1(F) \rightarrow {}^4T_1(P)$ ] and splits in several sub-peaks due to the distorted nature of the octahedral M2 and M1 polyhedra in olivine. Of these seven peaks Taran (Taran and Rossman, 2001) interprets four absorption peaks related to Co in the M2 polyhedron and three in the M1 polyhedron. The intensity of this absorption is very strong and dominates the absorption in the range of visible spectra.

In pyroxene the major absorption was due to split  ${}^4T_1(F) \rightarrow {}^4T_1(P)$  transition, showing two strong peaks in the visible region (White et al., 1971).

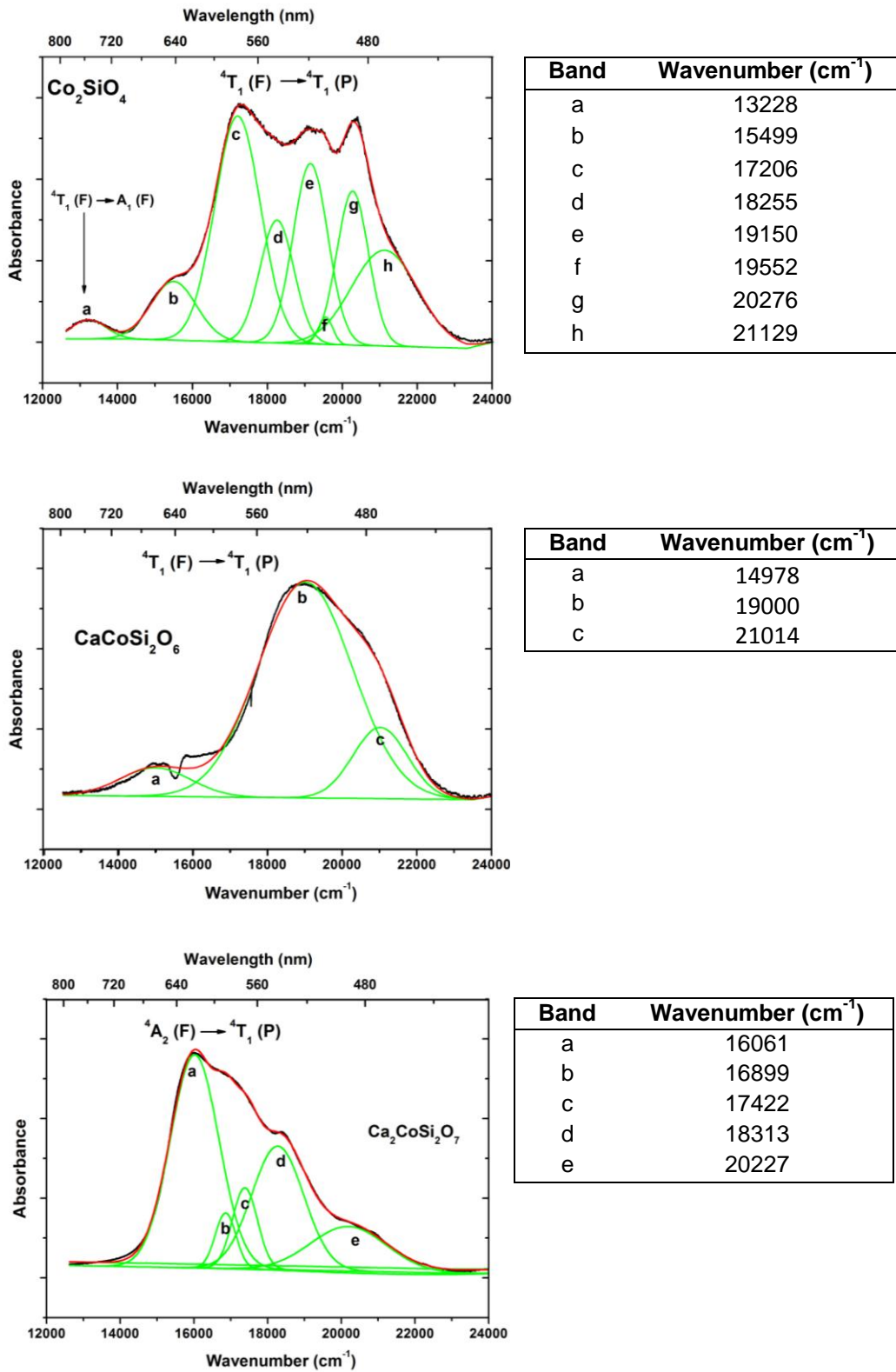


Fig.2.14: Optical absorption spectra of Co-olivine, Ca,Co-px and Co-akermanite with an attempt of deconvolution.

In Co-ackermanite (where Co is in tetrahedral coordination) the two spin allowed bands fall in the infrared region (1400 and 1600 nm) and only the third one is present in the visible region, usually as a triple band around 540, 590 and 640 nm, which gives rise to the blue coloration.

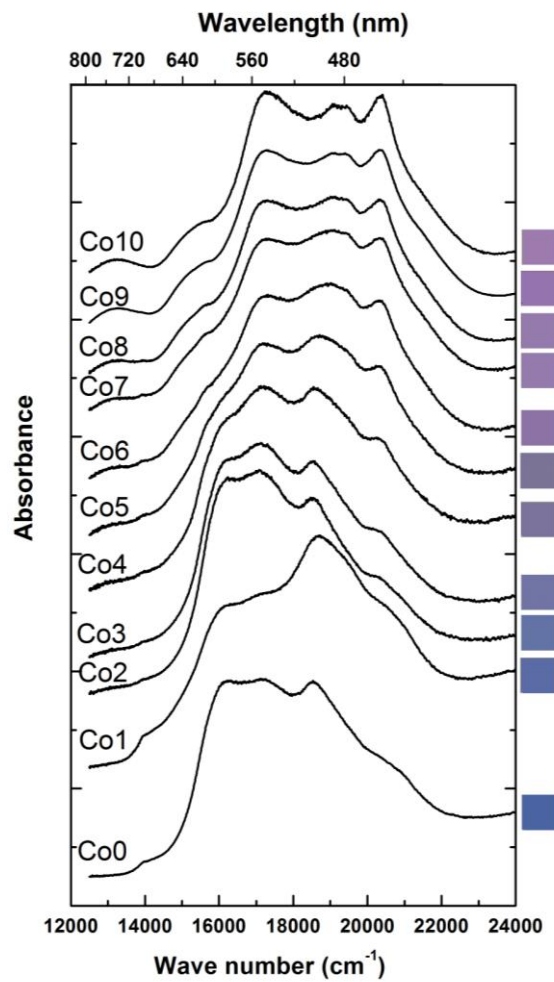


Fig.2.15: optical spectrum of the samples synthesized at 1000°C for 12 hours and their colour resulting

In our composite spectra the three complex spectra of the phases are superimposed, and can be hardly determined. What is observed in the optical absorption spectra measured in the range  $13000\text{-}24000\text{ cm}^{-1}$  (833-416 nm) is a large and composite absorption peak in the visible region with maximum transmission in the red and violet wavelength. As shown in figure 2.10 the broad peaks can be fitted by several Gaussian peaks, all related to the absorption of  $\text{Co}^{2+}$  both in octahedral and tetrahedral coordination. In the first group from the sample Co0 to Co5 we observed some peaks in the range from  $16000$  to  $20000\text{cm}^{-1}$ , while in the second group, between Co5 and Co10 the number of the peaks increased and shifted towards higher wavelength. The absorption in the first region (at about 600-550 nm) is related to the blue appearance of the samples. In the second region the sample absorbs much of the blue component so we perceive pink-violet as a result.

## ***Experimental conditions for a Co-pyroxene based pigment***

Co-pyroxenes can be synthesized at room pressure only in the  $\text{CaCoSi}_2\text{O}_6$  –  $\text{Ca}_{0.9}\text{Co}_{1.1}\text{Si}_2\text{O}_6$  range and an homogeneous clinopyroxene, suitable as a pure pigment, is obtained at room pressure by annealing at a temperature 1150°C for 24 hours or 1100°C for 96 hours.

These resulting samples are well-crystallized, and qualitative and quantitative analysis reveals the presence of  $\text{CaCoSi}_2\text{O}_6$  only. The colorimetric analysis confirm a deep pink hue as a result. Respect to the olivine based pigment the pyroxene shows a more distinct pink colour, with the need of lower Co-content (i.e. 10 wt% of Co in the formula  $\text{CaCoSi}_2\text{O}_6$  pyroxene respect 28 wt% in  $\text{Co}_2\text{SiO}_4$  Co-olivine).

During synthesis made at temperature of 1000°C for 12 hours in  $\text{CaCoSi}_2\text{O}_6$  the pyroxene coexists with Co-olivine and Co-akermanite and the reaction doesn't reach equilibrium. The point is critical for the presence of a Co-akermanite phase, where cobalt enters in tetrahedral coordination, resulting in a deep blue hue. In this situation the pigment cannot result as pink, since the colour blue prevailed even if it is present in small quantities. (i.e. in the samples Co 4 only 5% mol of  $\text{Co}^{\text{IV}}$  were sufficient to give a blue colour even if the remaining 95% Co is present in octahedral coordination)

When the annealing time or temperature increases the Co-akermanite disappears, so that pyroxene only is present. At 1200°C or higher the phase melts, and again we have a blue colour. Therefore the best condition for a pyroxene pigment are between 1100°C and 1200°C.

Longer duration synthesis from intermediate  $\text{CaCoSi}_2\text{O}_6$ - $\text{Co}_2\text{Si}_2\text{O}_6$  starting materials give at equilibrium mixtures of pyroxene, Co-olivine, tridimite, and metastable Co-





## **PART III**

# **High pressure synthesis: a mineralogical approach**

## ***Synthesis and sample characterization***

### ***Synthesis***

The starting materials for the high pressure experiment is the mixture of phases obtained after the first series of runs at a temperature of 1000°C and for 12 hours.

The high pressure experiments are performed with a piston cylinder apparatus at University of Edinburgh, School of Geosciences. The starting material, finely ground, is put in a 5 mm inner diameter, 10 mm long, Pt capsule and welded shut. The capsules are placed into a 0.5 inch pyrex-talc piston-cylinder assembly containing an internal graphite furnace (Bromiley et al., 2004). The experiments are run at  $P = 3$  GPa and with a temperature range from 1100 to 1350 °C depending on the samples. Pressure and temperature are maintained constant for approximately six hours, then, the heating system is switched off and the samples are quenched. The temperature is measured with a Pt-Pt10%-Rh thermocouple. The piston cylinder apparatus is described in appendix. The sample with nominal composition  $\text{Co}_2\text{Si}_2\text{O}_6$  is synthesized both with piston cylinder ( $P = 3$  GPa,  $T = 1200^\circ\text{C}$ ) obtaining an assemblage of orthopyroxene and quartz; and then it is then compressed in a multianvil apparatus at  $T = 900^\circ\text{C}$  and  $P = 7$  GPa, obtaining a single clinopyroxene phase.

Further experiments are carried out with the same procedure but adding in the capsule 20 wt% distilled water to enhance the reaction speed. The samples are first heated at 1500°C for 30 minutes and then cooled from 1500°C to 1200°C for the samples Co2 ( $\text{Ca}_{0.8}\text{Co}_{1.2}\text{Si}_2\text{O}_6$ ) and Co4 ( $\text{Ca}_{0.6}\text{Co}_{1.4}\text{Si}_2\text{O}_6$ ) or to 1350°C for Co6 ( $\text{Ca}_{0.4}\text{Co}_{1.6}\text{Si}_2\text{O}_6$ ) and Co8 ( $\text{Ca}_{0.2}\text{Co}_{1.8}\text{Si}_2\text{O}_6$ ) and annealed for 6 hours. The higher temperature of annealing for Co6 and Co8 is chosen in order to avoid exsolution. An

assemblage of Ca,Co-pyroxene crystals sized up to 600  $\mu\text{m}$  is obtained, among which those examined for the single crystal XRD are selected by sharp optical extinction. No glass is found in any sample after the synthesis (Mantovani et al.2013). XRD powder diffraction and SEM-EDS characterization confirmed that Ca,Co-pyroxene is the only phase, with stoichiometric composition. The experimental conditions of the syntheses are reported in table 3.1. After every experiment the run products are characterized by means SEM-EDS, PXRD, Raman Spectroscopy and where it is possible X-ray single crystal and TEM.

Figure 3.1 shows some images of the synthesized samples at the optical microscope.

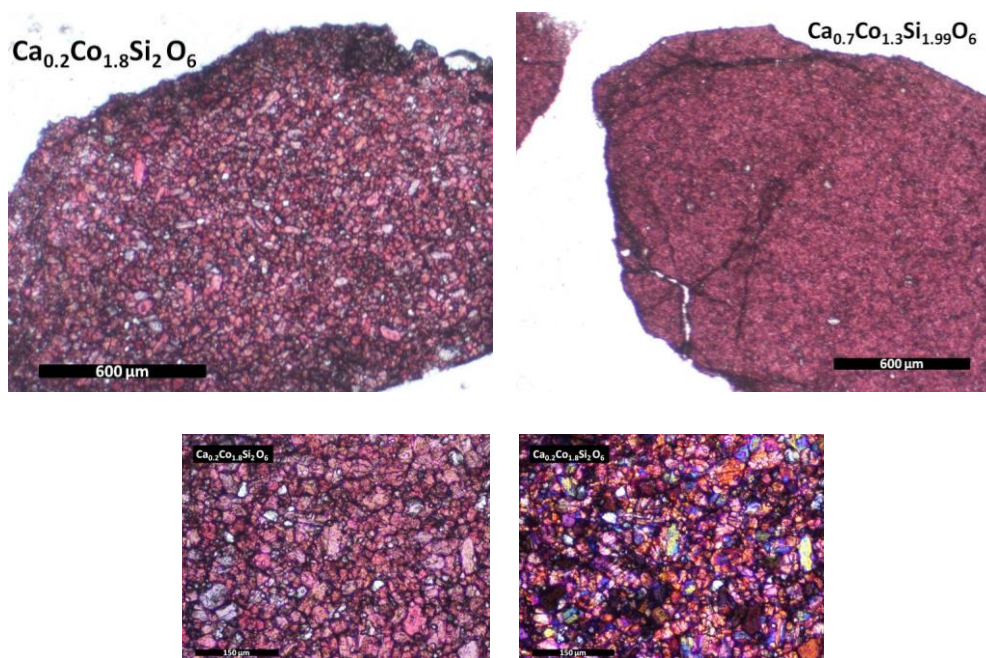


Fig. 3.1: images of the synthesized samples recorded by optical microscope:  
 a) Co8, 1350°C, 3 GPa (2.5x); b) Co3, 1200°C, 3GPa (2.5x) c) Co8, 1350°C, 3 GPa (10x);  
 Co8, 1350°C, 3 GPa (10x, NX);

Sample	Nom. Ca	Synthesis condition			Chemical analysis						Phase	Cell parameters				
		P (GPa)	T (°C)	t (h)	Ca	st. dev.	Co	st. dev.	Si	st. dev.		a (Å)	b (Å)	c (Å)	$\beta$ (°)	V (Å <sup>3</sup> )
Co0	1	3	1200	6	0.997	0.011	0.968	0.014	2.023	0.010	cpx	9.802(1)	8.962(1)	5.249(1)	105.40(1)	444.54(3)
Co1	0.9	3	1200	4	0.949	0.008	1.058	0.007	1.995	0.008	cpx	9.789(1)	8.949(1)	5.246(1)	105.53(1)	442.81(3)
Co2	0.8	3	1200*	6	0.860	0.008	1.133	0.006	2.005	0.005	cpx	9.791(1)	8.954(1)	5.246(1)	105.77(1)	442.58(8)
Co3	0.7	3	1200	4	0.723	0.015	1.283	0.017	2.010	0.006	cpx	9.777(1)	8.958(1)	5.242(1)	106.13(1)	441.05(8)
Co4	0.6	3	1200*	4	0.618	0.019	1.397	0.031	2.005	0.013	cpx	9.769(1)	8.964(1)	5.243(1)	106.46(1)	440.28(3)
Co5	0.5	3	1200	5	0.519	0.028	1.488	0.033	2.009	0.006	cpx	9.753(1)	8.962(1)	5.239(1)	106.78(1)	438.41(9)
Co5	0.5	3	1100	5	0.687	0.030	1.319	0.032	1.997	0.007	cpx (63.9 %) + pig <sup>+</sup> (36.0%)	9.806(1)	8.994(1)	5.260(1)	106.34(1)	445.3(1)
					0.206	0.051	1.837	0.048	2.007	0.011		9.698(1)	8.935(2)	5.237(1)	108.53(5)	433.7(1)
Co5	0.5	3	1280	7	0.517	0.027	1.477	0.029	1.997	0.013	cpx	9.747(1)	8.962(1)	5.237(1)	106.84(3)	437.83(9)
Co5	0.5	3	1350	6	0.517	0.014	1.498	0.005	2.018	0.023	cpx	9.751(1)	8.964(1)	5.238(1)	106.83(1)	438.28(8)
Co6	0.4	3	1200	4	0.561	0.101	1.436	0.102	2.002	0.008	cpx	9.735(2)	8.971(2)	5.250(1)	107.49(1)	437.3(2)
Co6	0.4	3	1200*	6	0.626	0.035	1.376	0.036	1.999	0.005	cpx (66.6%) + opx(33.3%)	9.747(1)	8.955(1)	5.233(1)	106.64(1)	437.66(5)
					0.110	0.011	1.891	0.017	2.000	0.005		18.338(3)	8.927(2)	5.207(1)		852.48(9)
Co6	0.4	3	1350*	6	0.392	0.020	1.631	0.021	1.998	0.005	cpx	9.747(6)	8.982(5)	5.249(3)	107.46(8)	438.37
Co6	0.4	3	1350		0.419	0.023	1.596	0.025	1.991	0.015	cpx	9.749(1)	8.963(1)	5.237(1)	106.82(7)	438.11(9)
Co7	0.3	3	1350	7	0.300	0.027	1.691	0.019	2.010	0.006	cpx	9.717(1)	8.952(1)	5.245(1)	107.92(6)	434.09(8)
Co8	0.2	3	1200	6	0.419	0.042	1.553	0.041	2.010	0.011	cpx (42.5%) + opx(57.9%)	9.738(1)	8.957(1)	5.244(1)	107.17(3)	437.05(7)
					0.131	0.019	1.866	0.028	2.003	0.015		18.357(2)	8.941(1)	5.224(1)		857.3(1)
Co8	0.2	3	1350	4	0.209	0.012	1.802	0.015	2.002	0.004	pig	9.707(1)	8.950(2)	5.238(1)	108.43(5)	431.7(1)
Co10	0	3	1200	6	-	-	2.012	0.123	2.005	0.015	opx	18.298(2)	8.921(2)	5.203(1)		849.4(1)
Co10	0	7	900	4	-	-	2(n.a.)	-	2 (n.a)	-	pig	9.650(3)	8.929(2)	5.220(1)	108.84(2)	424.3(1)

Table 3.1. Synthesis condition, chemical analysis (from SEM-EDS) and cell parameters (from PXRD) of the samples. For Co5, Co6 and Co8 at 1100°C and 1200°C weight % of the two phases are reported; (\*) water added in the capsule; (Pig<sup>+</sup>): monoclinic pyroxene with Ca content less than 0.25. If Ca is higher it is labelled as cpx.

### *X-ray Powder Diffraction and SEM-EDS analysis*

After the experiments the run products are characterized by means of SEM-EDS and powder X-ray diffraction.

For this two techniques the same instruments and the same operating conditions already described in the room pressure synthesis are used.

The first information we have are about the obtained phases: XRD powder diffraction and SEM-EDS characterization confirmed that, apart for a small quartz excess, pyroxene is the only phase present. Excess of quartz is related to the excess of silica in the starting materials.

A single pyroxene phase, whose composition is checked by SEM-EDS to be close to the expected stoichiometry is generally found. When pyroxene is a single phase, it shows a monoclinic symmetry in all but the Ca free composition Co10 at 1350°C and P = 3 GPa, where a single orthopyroxene phase is present.

But also in the Ca-free composition, a single clinopyroxene phase could be synthesized, by multinaeil so that the whole join of the monoclinic pyroxenes is obtained. A peak enlargement in Co6 at about  $2\theta = 36^\circ$  and the appearance of a small peaks in Co7 and Co8 suggest a phase transition from  $C2/c$  to  $P2_1/c$ , in analogy with previous papers along the join Di-En and Hd-Fs (Ohashi et al., 1975a).

The point will be better documented in the following chapters.

In syntheses at or below 1200°C, and for starting materials with Ca between 0.5 and 0.8 atoms p.f.u. in the nominal pyroxene, a two pyroxene assemblage of Ca-rich and Ca-poor pyroxenes is found. This can be well observed in figure 3.2 a) showing the XRD pattern of some samples synthesized at 1100 (Co5) or 1200°C (Co6). In Co5 and Co6 samples it is clearly visible the coexistence of two phases, clinopyroxene

and orthopyroxene; the latter visible by two little peaks, one at about 18° and another at 32° in 2θ.

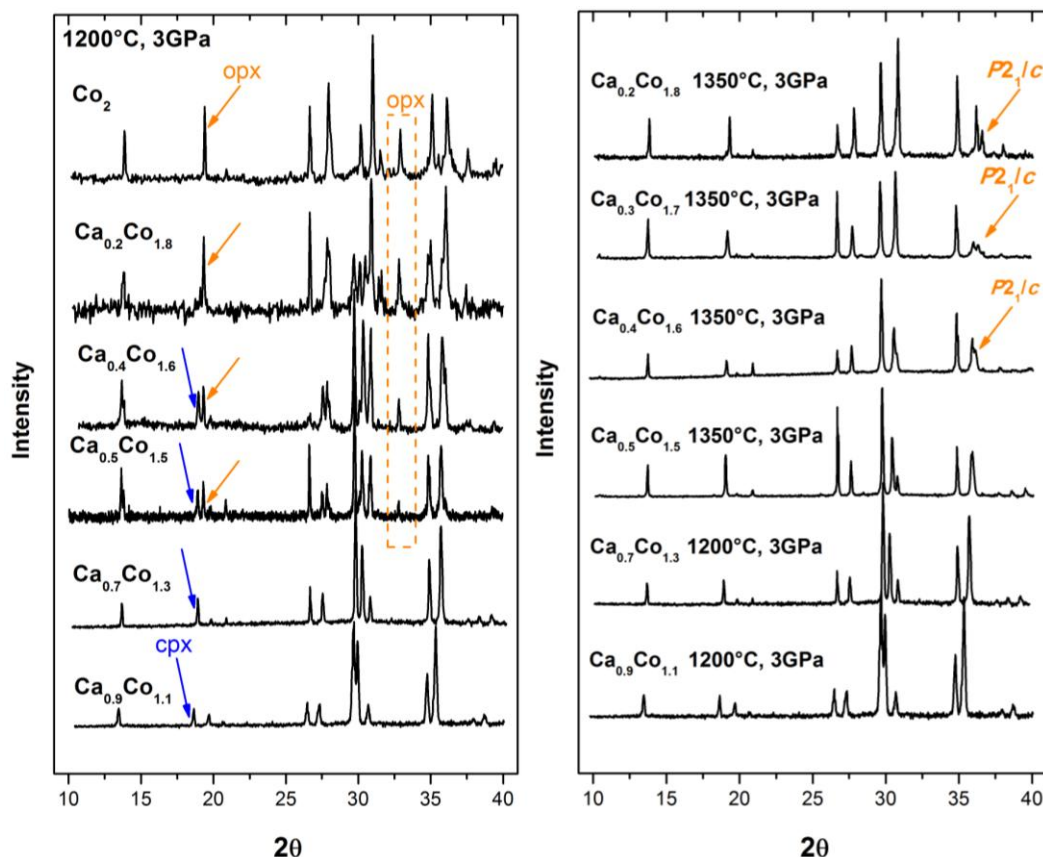


Fig. 3.2: XRD powder diffraction: a) diffraction patterns of the samples Co1 (1200°C), Co3(1200°C), Co5 (1100°C), Co6 (1200°C), Co8(1200°C), Co10 (1200°C): the arrows show the diagnostic peaks for the orthopyroxene; b) diffraction patterns of the samples Co1 (1200°C), Co3 (1200°C), Co5 (1350°C), Co6 (1350°C), Co7 (1350°C), Co8 (1350°): the arrows show little peak ascribable to P2<sub>1</sub>/c phase.

Cell parameters are calculated by Rietveld analysis starting from a structure model taken from Ghose et al. (Ghose et al., 1987) for C2/c CaCoSi<sub>2</sub>O<sub>6</sub> and from Sasaki et al. (S Sasaki, 1982) for Pbc<sub>a</sub> Co<sub>2</sub>Si<sub>2</sub>O<sub>6</sub>. Since no data are found in literature, for Co-rich samples (Co8 and Co10), the atom parameters are taken from the structure of an iron pigeonite (Ohashi et al., 1975b) and clinoferrosilite (Hugh-Jones et al., 1994), but with the substitution of the iron atoms with cobalt. The site occupancies

are based on the stoichiometric compositions with the assumption that Ca and Co share the M2 site and that Co fully occupies the M1 site. Such assumption is confirmed by single crystal XRD evidence (Mantovani et al. 2013).

The independent variable calculated are: scale factor, zero point, 8 coefficients of the shifted Chebyshev function to fit the background, cell parameters and profile coefficients, (2 Gaussian terms, Gv and Gw and one Lorentzian term, Lv). The value of  $\chi^2$  varied between 2.9 and 1.4. Atom positions, thermal vibration parameters and occupancies were also refined, to obtain better fit. The results of the phase cell parameters and composition are reported in table 3.1. An example of Rietveld refinement of a diffraction pattern with a single pyroxene phases is reported in figure 3.3.

As shown in table 3.2 cell parameters of the Ca-rich end member are not different from those found by Ghose et al. (1987). If we consider the Ca-free end member no data are available on monoclinic phase but only on orthorhombic symmetry. Cell dimension of the orthopyroxene Co<sub>10</sub> (1200°, 3GPa) is similar to the orthopyroxene analyzed by Sasaki et al. (1982).

	<b>CaCoSi<sub>2</sub>O<sub>6</sub> C2/c</b>		<b>Co<sub>2</sub>Si<sub>2</sub>O<sub>6</sub> Pbcn</b>	
	<i>Ghose et al. (1987)</i>	<i>This work</i>	<i>Sasaki et al. (1982)</i>	<i>This work</i>
<i>a</i> (Å)	9.806 (1)	9.802 (1)	18.296 (4)	18.298(2)
<i>b</i> (Å)	8.950 (1)	8.962 (1)	8.923 (1)	8.921(2)
<i>c</i> (Å)	5.243 (1)	5.249 (1)	5.204 (1)	5.203(1)
$\beta$ (°)	105.45 (1)	105.40 (1)		
<i>V</i> (Å <sup>3</sup> )	443.51 (10)	444.54 (3)	849.58 (12)	849.4(1)

*Tab. 3.2: Comparison between cell parameters data for CaCoSi<sub>2</sub>O<sub>6</sub> and Co<sub>2</sub>Si<sub>2</sub>O<sub>6</sub> found in literature and those of our syntheses.*

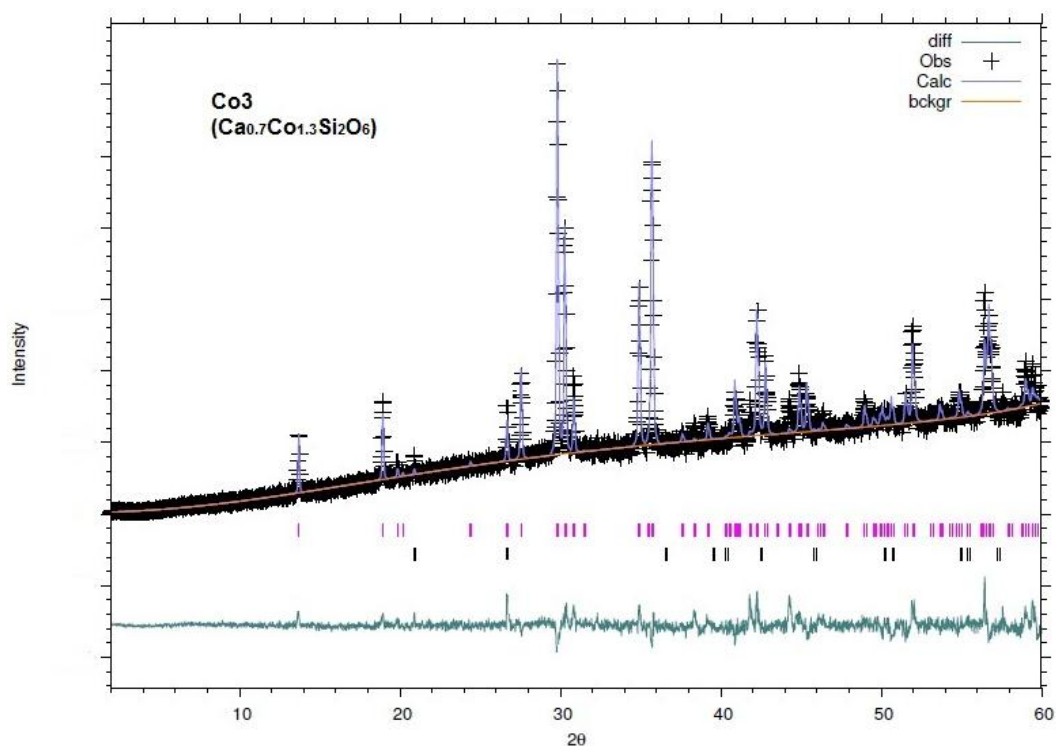


Fig. 3.3: Plot of the Rietveld refinement of the samples Co<sub>3</sub> (GSAS-EXPGUI software). The experimental data (obs) are indicated by crosses, the calculated pattern is continuous line, and the lower curve is the weighted difference between the calculated and observed patterns. Fitted background is reported in orange. Vertical tick marks report the position of allowed reflections for the CaCoSi<sub>2</sub>O<sub>6</sub> (in pink) and quartz (in black) phases present in the sample.

The composition of the phases is determined by SEM-EDS analysis over polished sections of the crystals. No less than 10 analytical spots are collected from homogeneous samples and 20 from heterogeneous. Average results are reported in table 3.1. Unit cell parameters and phase quantification (in the sample with two phases) are obtained by X-ray powder diffraction and Rietveld refinement.



Chemical analyses are expressed in atoms per formula units calculated on the basis of six oxygen and four cations; standard deviation is also reported (table 3.1).

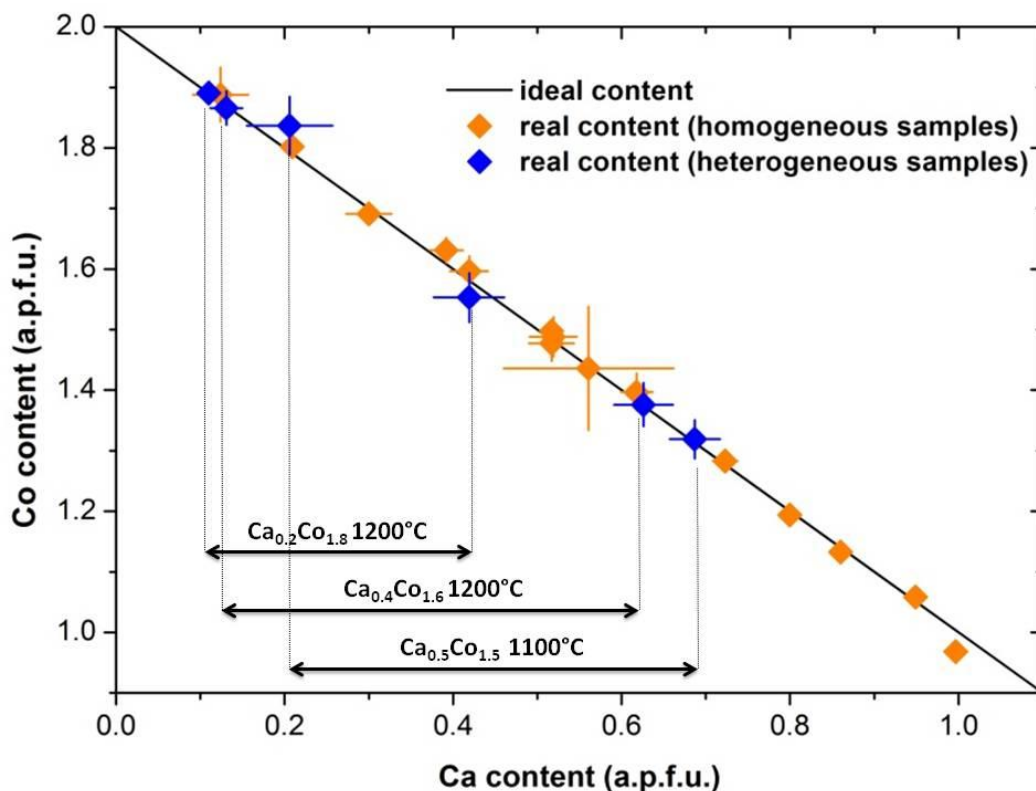


Fig. 3.4: Ca vs Co content from experimental data (blue and orange diamond) and the expected trend for stoichiometric composition (black straight line). Blue diamond represent the two composition of the samples formed by two phases.

The chemical analysis (EDS) shows a good agreement with the nominal composition of the samples. Figure 3.4 displayed the Ca vs Co content both from experimental data (blue and orange diamond) and from nominal composition (black straight line). The standard deviation is represented in error bar. Orange diamonds refer to homogeneous samples (single phase clinopyroxene) while blue ones represent the two compositions of the two phases – Ca-rich and Ca-poor - in the samples Co5 (1100°C, 3GPa), Co6 (1200°C, 3GPa) and Co8 (1200°C, 3GPa).

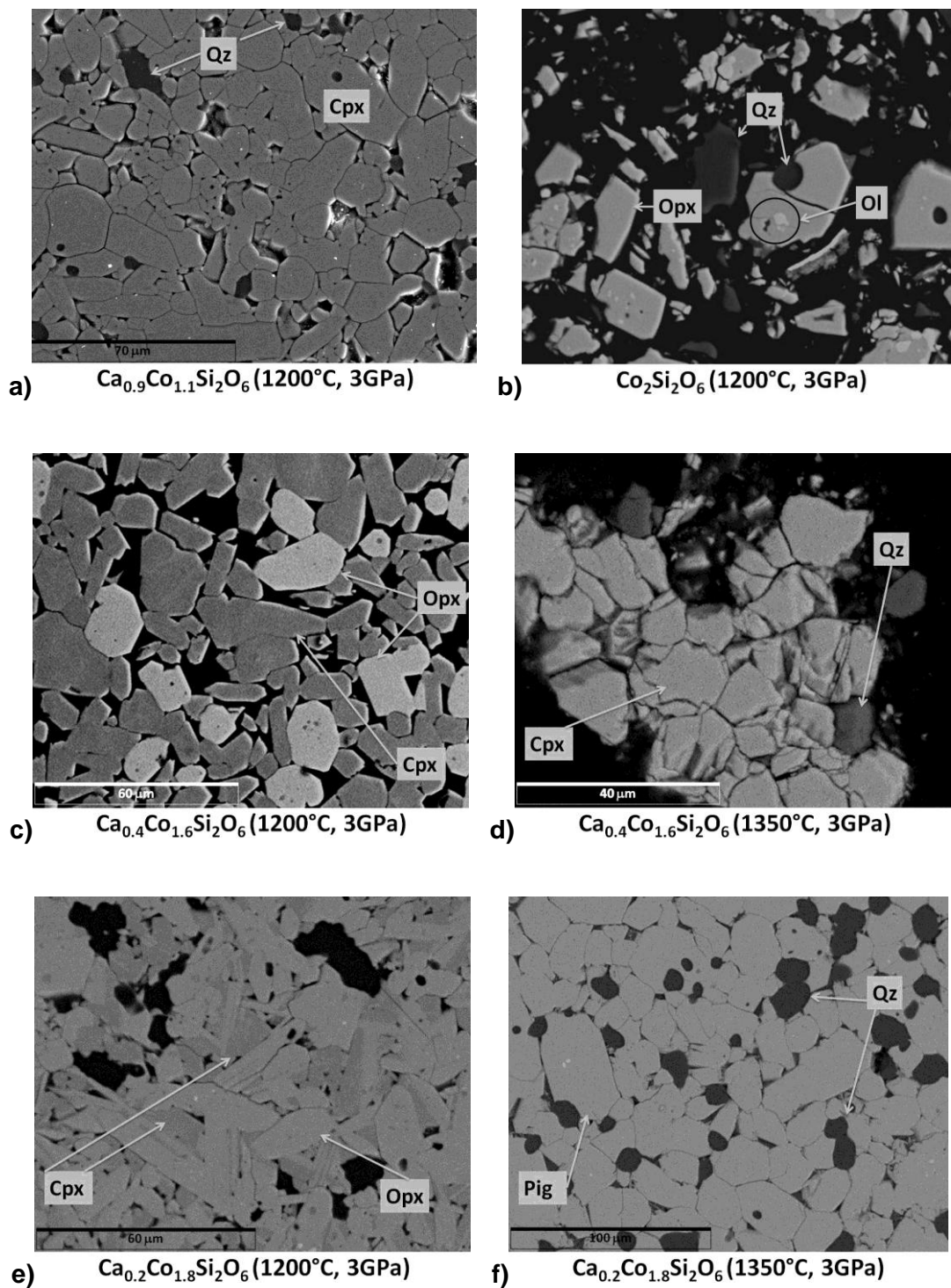


Fig.3.5: BS images of some samples: a)  $\text{Ca}_{0.9}\text{Co}_{1.1}\text{Si}_2\text{O}_6$  (1200°C, 3GPa), b)  $\text{Co}_2\text{Si}_2\text{O}_6$  (1200°C, 3GPa), c)  $\text{Ca}_{0.4}\text{Co}_{1.6}\text{Si}_2\text{O}_6$  (1200°C, 3GPa) d)  $\text{Ca}_{0.4}\text{Co}_{1.6}\text{Si}_2\text{O}_6$  (1350°C, 3GPa) e)  $\text{Ca}_{0.2}\text{Co}_{1.8}\text{Si}_2\text{O}_6$  (1200°C, 3GPa), f)  $\text{Ca}_{0.2}\text{Co}_{1.8}\text{Si}_2\text{O}_6$  (1350°C, 3GPa)

Figure 3.5 recorded with backscattered electron shows the morphology of some samples. They appear as euhedral crystals of about ten microns size. The shape is well defined and in few cases we can recognize the preferential growth axis *c*. BSE images reveal the presence of crystals with a different shades of grey: dark grey colour refers to quartz crystals (average atomic number  $Z = 10.6$ ). Glass or melt are not present, even minimally.

Ca-rich samples, from Co0 to Co4, appear very homogeneous with a chemical composition very similar to the nominal one. In Ca-poor sample (with Ca content equal or less than 0.5 atoms p.f.u.), synthesized at a temperature equal or less than 1200°C, (i.e. Co5 at 1100°C and 1200°C, Co6 at 1200°C and Co8 at 1200°C) we find two pyroxene phases, one Ca-richer and another Ca-poorer respect the nominal composition. The coexistence of a Ca-poor and Ca-rich pyroxene is interpreted, in accordance with literature data about Ca-Fe and Ca-Mg pyroxenes, as an evidence of a miscibility gap between pyroxenes (Gasparik and Lindsley, 1980; Lindsley and Munoz, 1969).

However, experimentally, the composition of the coexisting phases is poorly constrained. At 1200°C, for bulk composition Co5, only one phase pyroxene is found with a composition close to  $\text{Ca}_{0.52}\text{Co}_{1.48}\text{Si}_{2.01}\text{O}_6$ .

Sample Co6 at 1200°C is a single phase but with a strong deviation from the expected stoichiometry (Ca = 0.56 a.p.f.u. vs expected 0.40 a.p.f.u.). In sample Co8 at 1200°C two different phases are present, one Ca-poor with a composition of  $\text{Ca}_{0.13}\text{Co}_{1.87}\text{Si}_{2.01}\text{O}_6$  and another Ca-rich with a composition  $\text{Ca}_{0.42}\text{Co}_{1.55}\text{Si}_{1.99}\text{O}_6$ . Within the miscibility gap, at a given temperature the system is invariant, that is the coexisting phases and their composition will be the same for any bulk composition within the gap. The above differences between Co5, Co6 and Co8 indicate that

equilibrium is not reached likely for sluggishness of the reaction. To enhance the reaction and determine the extension of the miscibility gap at 1200°C and 1100°C water is added into the capsule during the synthesis. In fact in the samples Co6 synthesized at 1200°C with water in the capsule the formation of two different phases with a composition ( $\text{Ca}_{0.63}\text{Co}_{1.38}\text{Si}_2\text{O}_6$  and  $\text{Ca}_{0.11}\text{Co}_{1.89}\text{Si}_2\text{O}_6$ ) is observed. The sample Co5 at 1100°C, instead, is formed by two pyroxene phases, one Ca-rich with 0.69 Ca atoms (p.f.u.) and another, Ca-poor with 0.21 Ca atoms p.f.u.

In the Co10 sample (T =1200°C and P =3GPa) the pyroxene is only orthorhombic, as shown by XRD diffraction. Co-olivine is not present as a major phase, but as small rounded crystals within the pyroxene, that indicates its metastable nature. SEM-EDS analyses has not been done on sample Co10 (P = 7GPa, T =1000°C,) due to the scarcity of the material.

As concern intermediate composition figure 3.6 shows the variation in lattice parameters as a function of Co content (a.p.f.u.) in M2 for single phase clinopyroxenes.

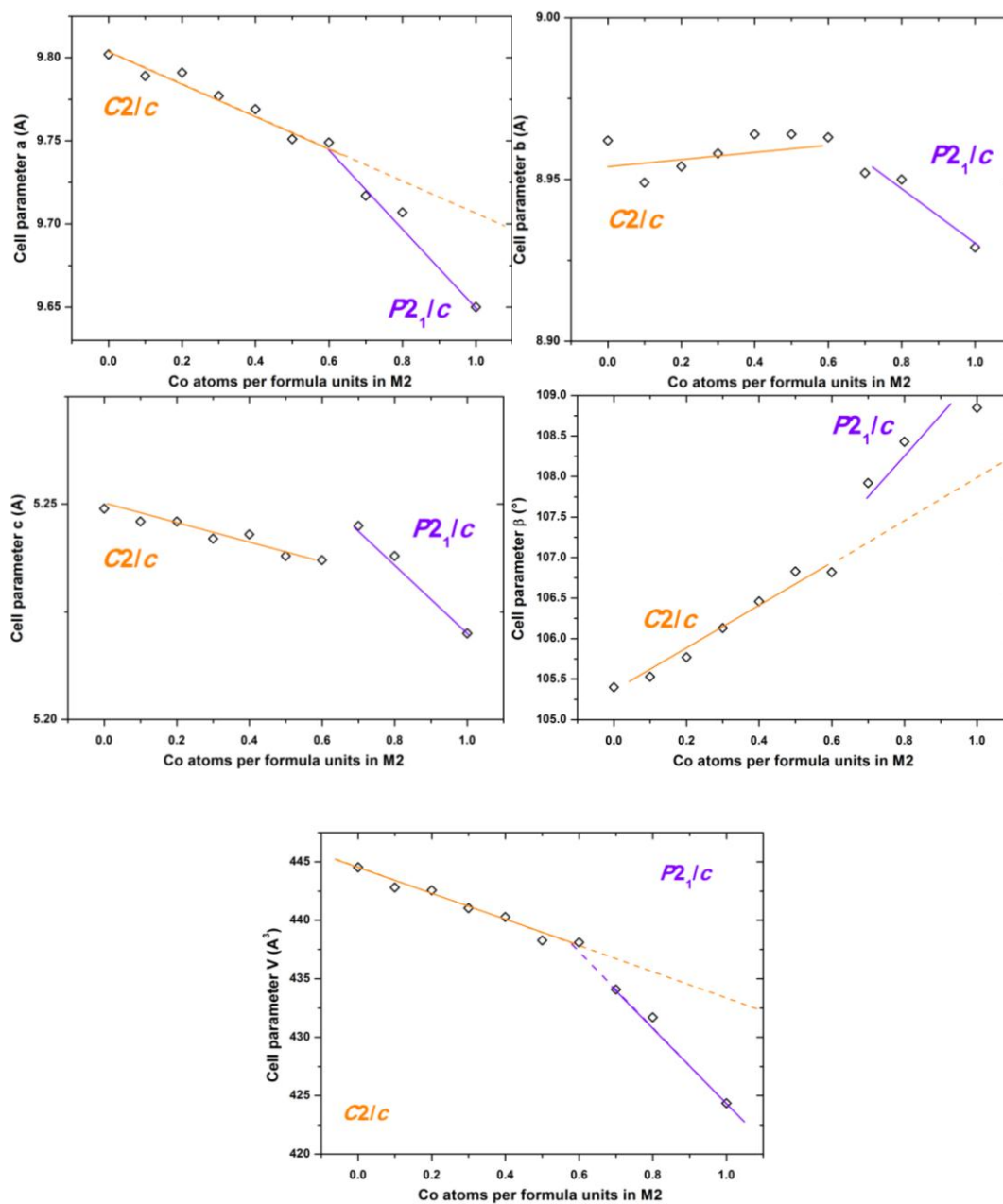


Fig. 3.6: cell parameters of the monoclinic series  $\text{CaCoSi}_2\text{O}_6\text{-Co}_2\text{Si}_2\text{O}_6$ . Trend line for *C2/c* and *P2<sub>1</sub>/c* each phases are reported.

Starting from the Ca-rich end member and increasing cobalt content we can notice that the parameter *a* exhibits a decrease (from 9.802 Å to 9.650 Å) while *b* and *c* are almost constant at an average value respectively of 8.944 Å and 5.234 Å in the first part of the series, and then they show a decrease in Co-richer samples;  $\beta$  angle

increases from  $105.4^\circ$  to  $108.3^\circ$  while volume decreases from  $445.3 \text{ \AA}^3$  to  $425.2 \text{ \AA}^3$ . Along the series linear changes with composition are never observed, but every parameter show a marked change at about 0.4 - 0.3 Ca content (atoms p.f.u.) like the inversion in the slope of in the **b** parameter at about 0.4 - 0.3 Ca content (samples Co6 - Co7). At the same composition a change in the intensity of several major reflections and the above cited peak at about  $2\theta = 36^\circ$  is observed.

The above changes in cell parameters and diffraction pattern are observed also in pyroxene along the series Di-En and Hd-Fs, indicating a transition from *C2/c* to *P2<sub>1</sub>/c*.

In analogy with literature data we can suppose that the miscibility gap and phase transition occur similarly for the join Di-En and Hd-Fs pyroxenes (Gasparik and Lindsley, 1980; Lindsley, 1980; Lindsley and Munoz, 1969). A sketch of a  $\text{CaCoSi}_2\text{O}_6$  -  $\text{Co}_2\text{Si}_2\text{O}_6$  phase diagram, and the compositions found in the synthesis of the samples, in and out the miscibility gap are represented in figure 3.7.

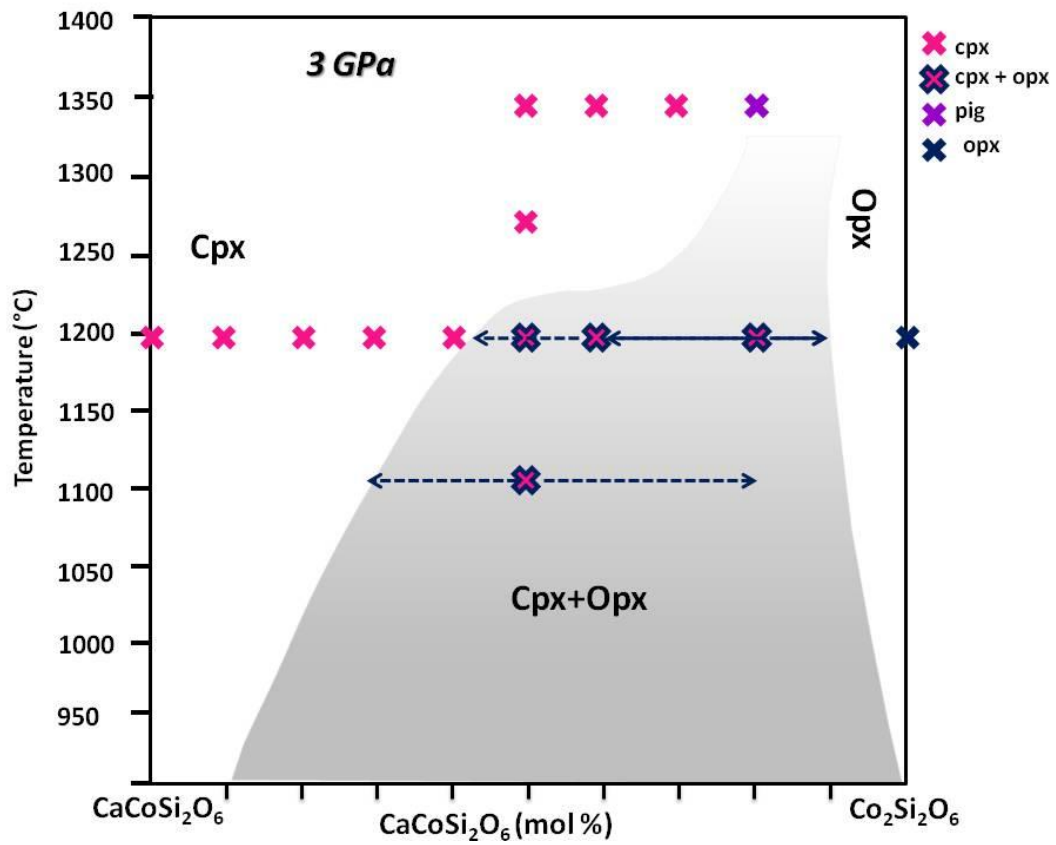


Fig. 3.7: sketch of the phase diagram of the series  $\text{CaCoSi}_2\text{O}_6$  -  $\text{Co}_2\text{Si}_2\text{O}_6$  at 3GPa

### Raman Spectroscopy

Raman spectroscopy is performed on powdered samples using a Jobin-Yvon Horiba LabRam microRaman apparatus, already described in part II. An average of ten analyses is made on every sample to verify the homogeneity at a micrometer scale.

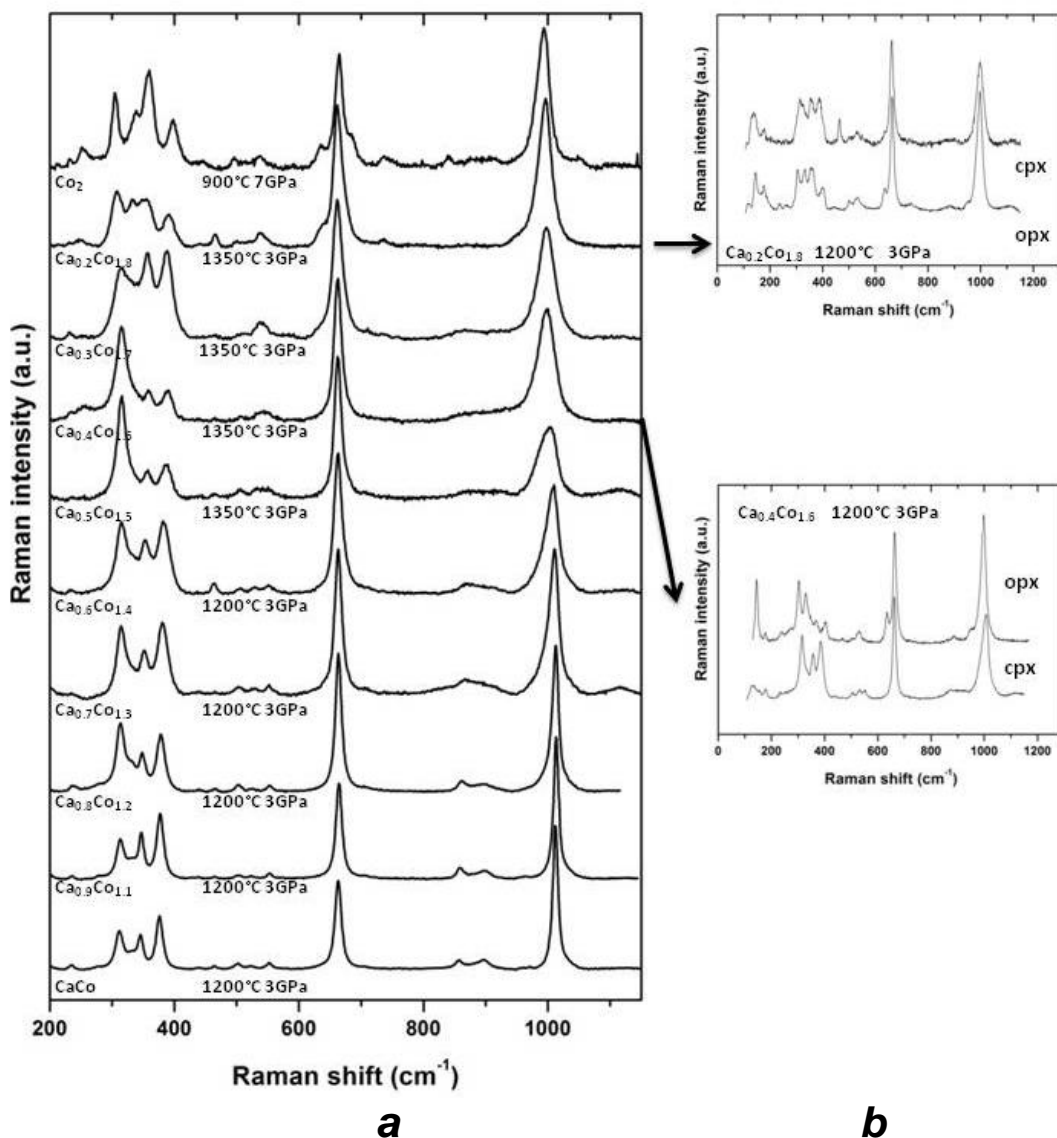


Fig. 3.8: a) Raman spectra of the monoclinic series  $\text{CaCoSi}_2\text{O}_6\text{-Co}_2\text{Si}_2\text{O}_6$ , b) Raman spectra of the samples formed by two pyroxenes, monoclinic and orthorhombic.



Sample	$\nu_1$	$\nu_2$	$\nu_3$	$\nu_4$	$\nu_5$	$\nu_6$
$\text{Ca}_1\text{Co}_1$	311.4	330.7	345.6	375.9	662.9	1012
	13.1	22.8	9.5	11.6	11.5	9.6
$\text{Ca}_{0.9}\text{Co}_{1.1}$	312.5	329.9	346.3	376.4	663.4	1011
	16.6	12.8	10.5	11.9	11	9.8
$\text{Ca}_{0.8}\text{Co}_{1.2}$	312.9	330.1	348	377.6	663.1	1011.2
	14.7	13.2	12.3	13.5	11.3	11.4
$\text{Ca}_{0.7}\text{Co}_{1.3}$	314.5	332.2	351.7	381	663.2	1009.4
	15.6	12.0	15.4	18.2	13.1	18.9
$\text{Ca}_{0.6}\text{Co}_{1.4}$	314.8	331.8	353.8	382.8	663.3	1008.1
	13.2	57	13.7	16.6	13.3	21.7
$\text{Ca}_{0.5}\text{Co}_{1.5}$	315.3	333.8	355.2	384.4	662.3	1003.7
	19.3	13.8	17.8	19.4	14.1	27.8
$\text{Ca}_{0.4}\text{Co}_{1.6}$	312.9	331.3	357.1	387	661.4	998
	19.8	56	23	19.4	19.1	30.6
$\text{Ca}_{0.3}\text{Co}_{1.7}$	314.2	336.2	357	387.8	662.4	997.4
	23.7	16.7	19.6	20.6	20.2	27.3
$\text{Ca}_{0.2}\text{Co}_{1.8}$	307.5	346.4	358.1	391.1	662.5	995
	17.5	14.5	17.5	18	19	24
$\text{Co}_2$	300.9	353.3	361.7	402.1	662.3	993.3
	12.2	21.1	30.8	12.3	13.8	22.7

Tab.3.3: Peak positions and linewidth of the fitted Raman peaks of monoclinic series  $\text{CaCoSi}_2\text{O}_6\text{-Co}_2\text{Si}_2\text{O}_6$ . Error is estimated  $\pm 0.5 \text{ cm}^{-1}$

Raman spectra of monoclinic pyroxenes along the join  $\text{CaCoSi}_2\text{O}_6\text{-Co}_2\text{Si}_2\text{O}_6$  are shown in figure 3.8, their peak positions and linewidth are reported in table 3.3.

From factor-group analysis (Wang et al., 2001)  $C2/c$  and  $P2_1/c$  pyroxenes are expected to exhibit 30 and 60 active Raman peaks, respectively, but most part of them are too weak to be observed experimentally.

In fact about 15 peaks could be identified in  $\text{CaCoSi}_2\text{O}_6$  Raman spectrum, but only six of them (at 310, 330, 350, 380, 660 and  $1010 \text{ cm}^{-1}$ ) could be followed throughout the join (table 3.3). This number of peaks is comparable to the number studied in a set of natural and synthetic quadrilateral pyroxenes by Huang et al. (2000) and Wang et al. (2001).

The peaks come from different vibration modes, which are related to specific structural features (Wang et al 2001, Prencipe et al. 2012). According to literature data the pyroxene spectrum is divided in three region:

- 1) T-O stretching peaks near  $1000\text{ cm}^{-1}$ , including an intense peak at  $1010\text{ cm}^{-1}$  ascribed to stretching modes of Si and non-bridging O1 and O2 atoms within the  $\text{SiO}_4$  tetrahedron (R1 region according to Wang et al., 2001);
- 2) peaks due to chain bending and/or stretching at  $500\text{--}700\text{ cm}^{-1}$  (R2 and R4 in Wang et al., 2001), including the most intense peak at  $665\text{ cm}^{-1}$  and a few weak peaks around  $500\text{ cm}^{-1}$
- 3) peaks below  $500\text{ cm}^{-1}$  generally ascribed to non-tetrahedral cation-oxygen stretching of M1-O and M2-O bonds (R3 and R5 regions in Wang et al., 2001).

Within this frame each pyroxene phase has its own spectrum. For example in figure 3.9 the same Raman spectrum of diopside from Prencipe et al. (2012) is compared with that of  $\text{CaCoSi}_2\text{O}_6$ .

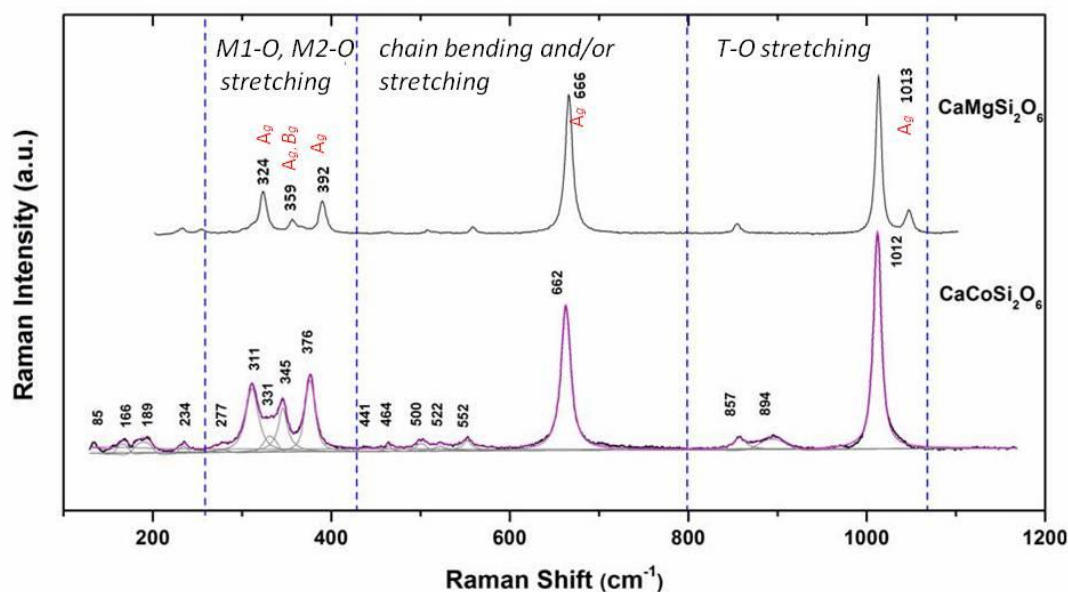


Fig. 3.9: comparison between Raman spectrum of diopside (from Prencipe et al., 2012) and that of  $\text{CaCoSi}_2\text{O}_6$ .

We can observe that the main peaks related to M-O stretching of the  $\text{CaCoSi}_2\text{O}_6$  are slightly shifted towards shorter wavenumber. Specifically, in  $\text{CaCoSi}_2\text{O}_6$  the triplet at  $300 - 400 \text{ cm}^{-1}$  is shifted on average by  $15 \text{ cm}^{-1}$  respect to diopside. Minor differences are present in the peaks at  $666 \text{ cm}^{-1}$  and  $1010 \text{ cm}^{-1}$  related to tetrahedral silicate chain.

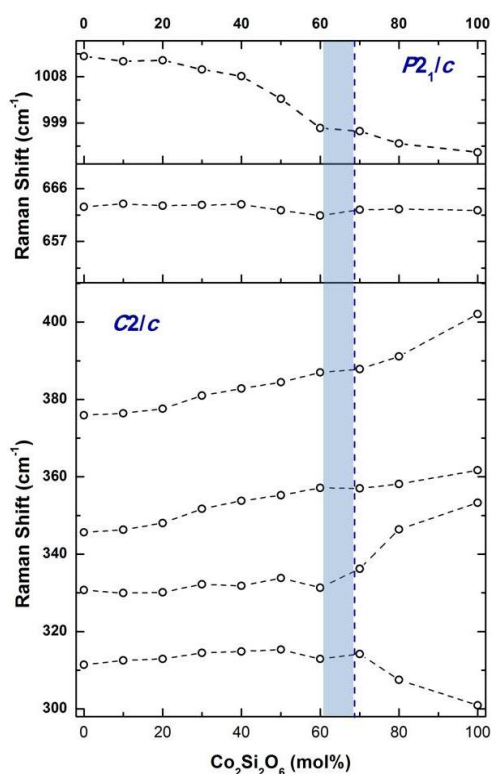


Fig.3.10: trend of the most important peaks of the monoclinic series  $\text{CaCoSi}_2\text{O}_6$ - $\text{Co}_2\text{Si}_2\text{O}_6$ . Blue area suggest the critical composition of the transition

When comparing Raman spectra along the join  $\text{CaCoSi}_2\text{O}_6$ - $\text{Co}_2\text{Si}_2\text{O}_6$  we find that almost all the peaks, except that at  $666 \text{ cm}^{-1}$  change with composition. The peaks between  $300$  and  $400 \text{ cm}^{-1}$ , related to the M-O stretching show different trend: while the peaks at  $330 \text{ cm}^{-1}$ ,  $350 \text{ cm}^{-1}$ , and  $380 \text{ cm}^{-1}$  increased with Co content, that at  $310 \text{ cm}^{-1}$  decreases.

Changes with composition are not continuous, as most peaks show a turnover at about 0.4 - 0.3 Ca content (atoms p.f.u.). This is best observed in the peaks at 310, 330, 380 and 1000  $\text{cm}^{-1}$ .

The strong peak at 660  $\text{cm}^{-1}$  does not change its position along the series, but a side peak appears at about 630  $\text{cm}^{-1}$  at a composition of  $\text{Ca}_{0.2}\text{Co}_{1.8}\text{Si}_2\text{O}_6$ , seemingly a peak splitting. At the same composition more peaks than in the Ca richer series are present: four distinct peaks at about 300-400  $\text{cm}^{-1}$ , instead of three, and two small peaks and 980  $\text{cm}^{-1}$  arise.

Similar changes are observed along the series diopside – enstatite (Tribaudino et al. 2012); they are compared with those of  $\text{CaCoSi}_2\text{O}_6$ - $\text{Co}_2\text{Si}_2\text{O}_6$ .(figure 3.11).

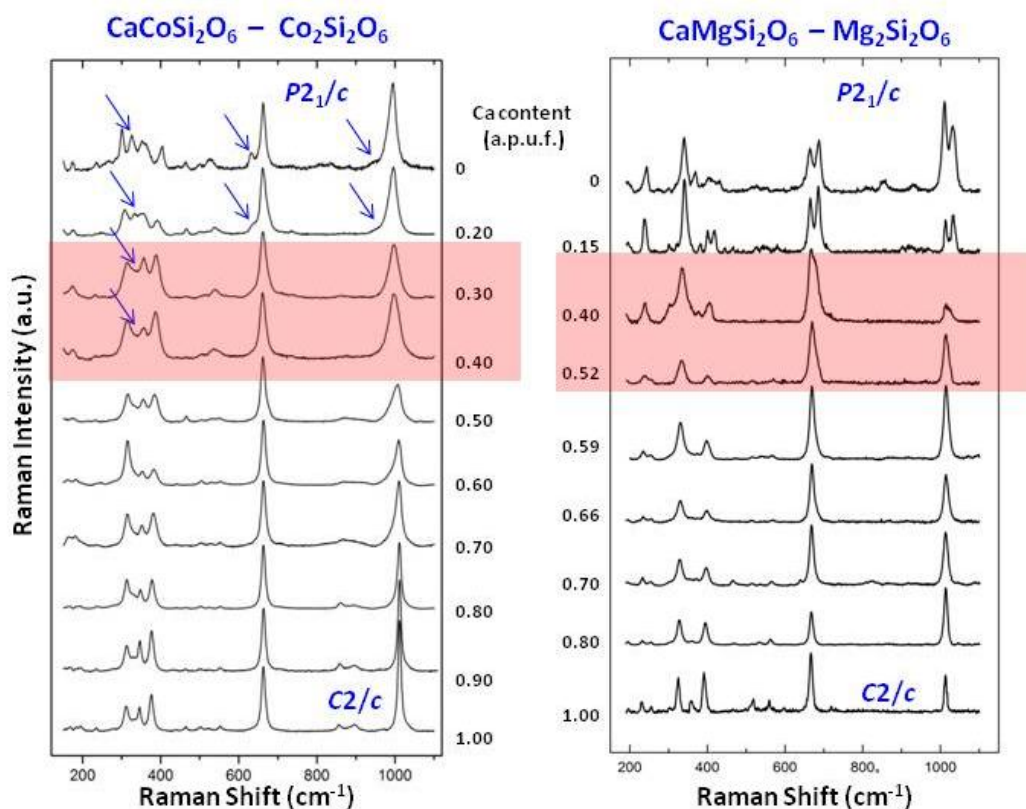


Fig. 3.11: comparison between peaks profiles of the series  $\text{CaCoSi}_2\text{O}_6$ - $\text{Co}_2\text{Si}_2\text{O}_6$  and those of  $\text{CaMgSi}_2\text{O}_6$ - $\text{Mg}_2\text{Si}_2\text{O}_6$  (Di-En) from Tribaudino et al. (2012)

In the two series we have an increase in the spectral complexity comparing Ca rich and Ca-poor pyroxenes; another common point is the presence of a transition field, shown by the spectra of clinopyroxenes with 0.3 and 0.4 Ca atoms p.f.u. in Ca,Co-pyroxenes, and with 0.40 and 0.52 in Ca,Mg ones. A deviation from linear behaviour in the peak position vs composition plot is found also in pyroxenes along the join diopside-enstatite, as well as peak splitting for the peaks at  $666\text{ cm}^{-1}$  and  $1010\text{ cm}^{-1}$ . In the diopside-enstatite series, by comparison of single crystal structural data and Raman spectra, these changes are interpreted as due to the transition from the  $C2/c$  to the  $P2_1/c$  structure. As highlighted in the introduction such transition is expected in the Ca-poorer clinopyroxenes. In the  $\text{CaCoSi}_2\text{O}_6$ - $\text{Co}_2\text{Si}_2\text{O}_6$  clinopyroxenes the same interpretation likely applies. In diopside-enstatite the transition could be pinpointed at the turnover of peak position vs composition plots, and similarly we could pinpoint the  $C2/c$  to  $P2_1/c$  phase transition in Ca,Co-pyroxenes at 0.40 Ca atoms per formula unit.

Another common feature between Ca,Mg and Ca,Co pyroxenes is the increasing linewidth with decreasing Ca, even in the  $C2/c$  clinopyroxene field, which is related, in the diopside-enstatite join, to increased structural disorder. Figure 3.12 reports changes in linewidth along the series  $\text{CaCoSi}_2\text{O}_6$ - $\text{Co}_2\text{Si}_2\text{O}_6$  and Di-En for three peaks,  $390$ ,  $666$  and  $1010\text{ cm}^{-1}$ .

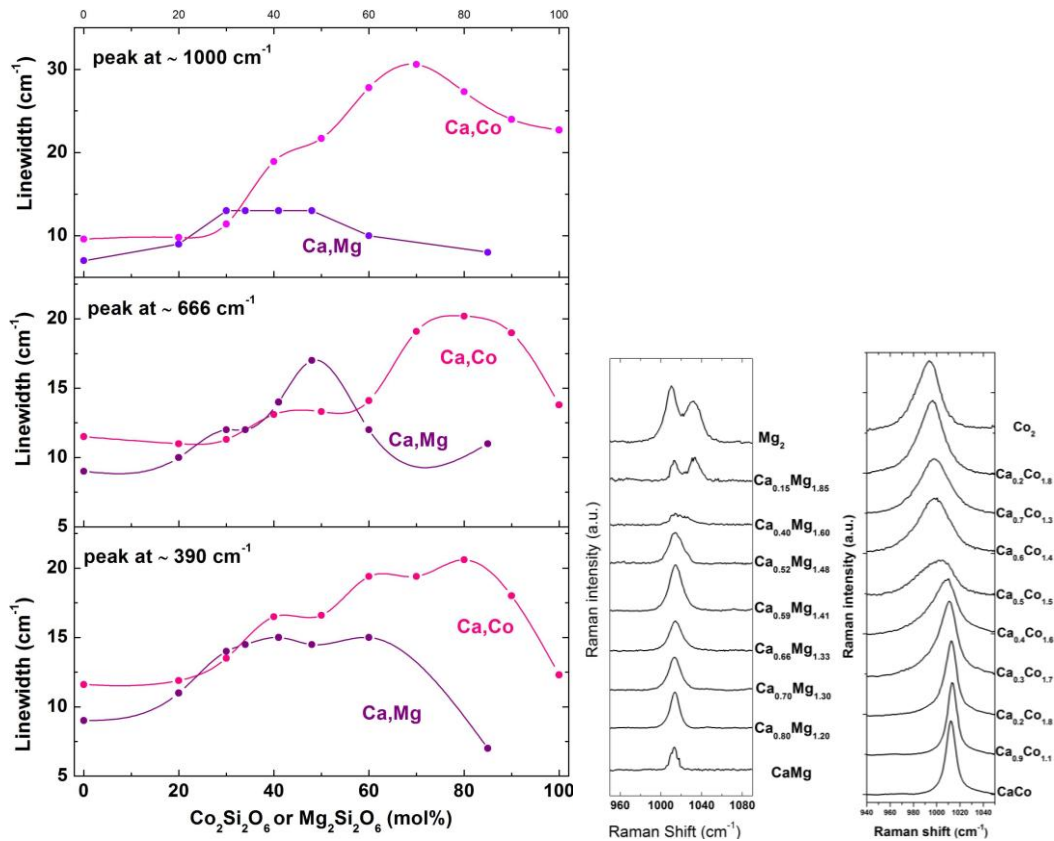
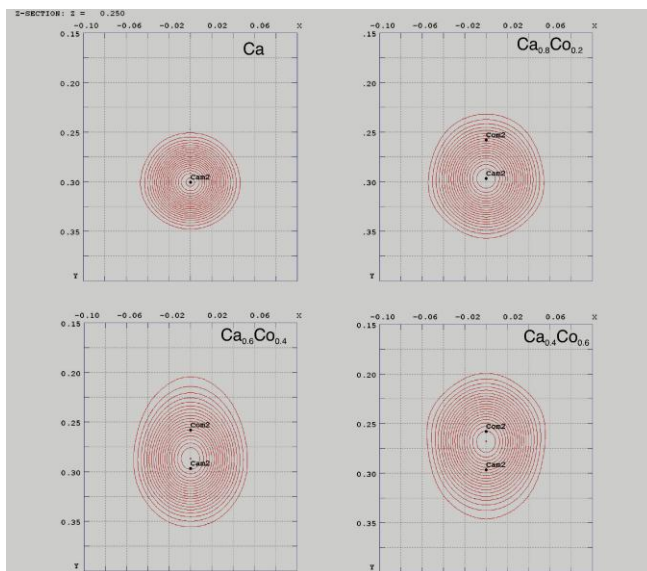


Fig. 3.12: a) linewidth relative to three peaks (1010, 666 and 390  $\text{cm}^{-1}$ ) both for  $\text{CaCoSi}_2\text{O}_6$ - $\text{Co}_2\text{Si}_2\text{O}_6$  and Di-En b) enlargement of the Raman spectra at about 1000  $\text{cm}^{-1}$  to show the difference between the splitting of the peaks in Di-En and the change in position in  $\text{CaCoSi}_2\text{O}_6$ - $\text{Co}_2\text{Si}_2\text{O}_6$

The linewidth reaches a maximum value at about  $\text{Ca}_{0.3}\text{Co}_{1.8}\text{Si}_2\text{O}_6$  for the  $\text{CaCoSi}_2\text{O}_6$ - $\text{Co}_2\text{Si}_2\text{O}_6$  series and at about  $\text{Ca}_{0.5}\text{Mg}_{1.5}\text{Si}_2\text{O}_6$  for the Di-En series and decreases at higher concentration of Mg or Co. Also for Ca, Co pyroxenes the increased linewidth is related to structural disorder, related to the mechanism of solid solution and possibly to the coexistence of  $C2/c$  and  $P2_1/c$  phases close to the transition, as found in diopside-enstatite by TEM observation (Tribaudino 2000).

This structural disorder within the  $C2/c$  field is related to the split of the M2 site. In single crystal X-Ray diffraction made on three samples (Co<sub>2</sub>, Co<sub>4</sub>, and Co<sub>6</sub>, Mantovani et al. 2013) we found that Ca and the smaller cation Co split in two

different positions along the diad axis, into the M2 cavity, respectively the M2 and M2' subsites. The split of the M2 site is observed in the Di-En series also by Rossi et al. (1987) and Tribaudino and Nestola (2003).



*Fig.3.13: electron density map at the M2 site (x across, y down) ; the cation occupancy of the site is reported. CaM2 and CoM2 site positions are always located respectively at the M2 and M2' positions (from Mantovani et al.,2013)*

The split can be shown by the electron distribution along the diad axis. As shown in the Fourier map in figure 3.13, if a cation smaller than Ca, like Co or Mg, is present in little amount the asymmetric electron distribution is most evident; if Ca and the smaller cation are in an amount, such that the electron distribution of the two cations is similar, a large apparent displacement parameter is found. Site splitting is then revealed by large atomic displacement parameters. In fact the size of the displacement parameters of the M2 site increases with cobalt content, and is also proportional to the sum of the linewidth of the four Raman peaks related to M-O motion ( $300-400\text{ cm}^{-1}$ ), as shown in figure 3.14.

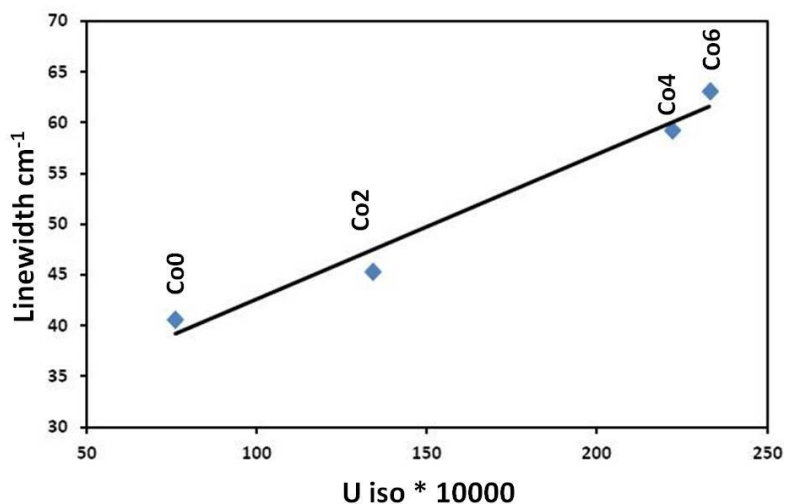


Fig 3.14: sum of the linewidth (FWHM) of the four Raman peaks related to M-O motion vs displacement parameters of the samples Co0 (from Ghose et al., 1987) Co2, Co4 and Co6.

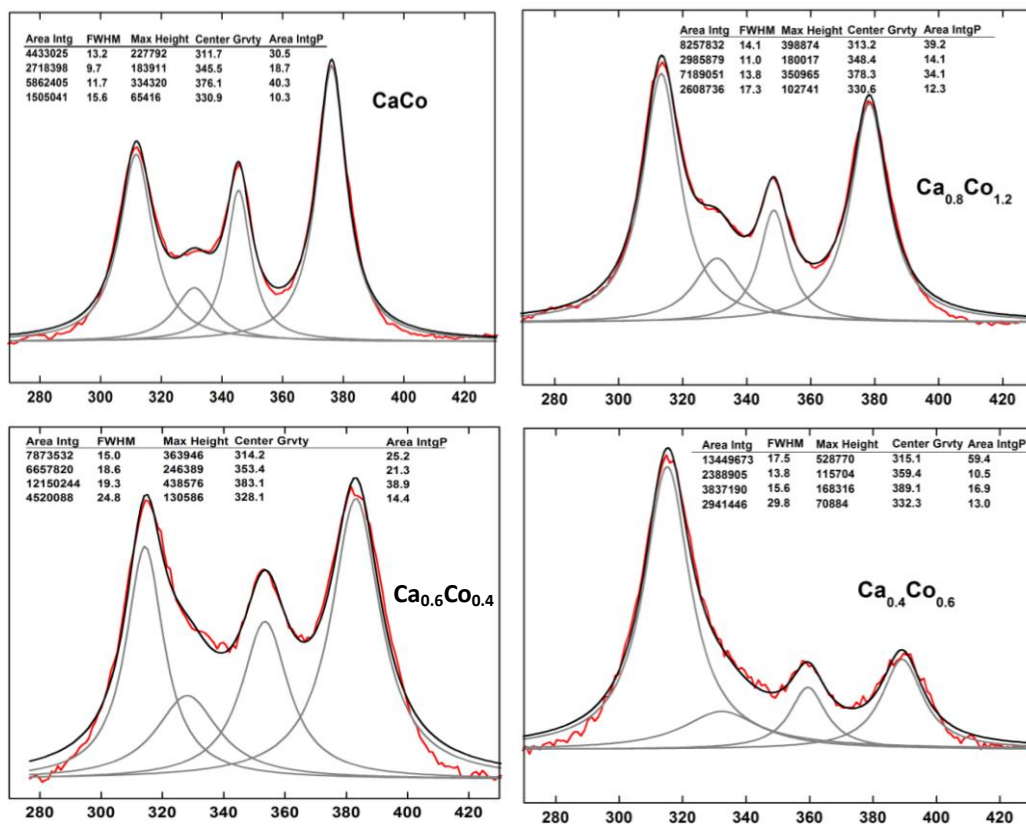


Fig. 3.15: example of the fitted Raman peaks in the range 300-400 cm<sup>-1</sup> ascribable to M-O motion for the samples Co0, Co2, Co4 and Co6.



### Transmission Electron Microscope (TEM)

The transmission electron microscope is an analytical tool that allows detailed micro-structural examination with high-resolution and high-magnification. In the analysis of crystal structures it is used to obtain diffraction patterns on crystals down to a nanometer scale, and lattice images down to atomic resolution.

In our samples TEM is however used only to determine the lattice of some examined crystals from the run Co7, by the exam of the diffraction pattern. The composition is critical: by the combined exam of X-ray diffraction and Raman spectra we have found that the transition occurred in pyroxenes with composition between 0.4 and 0.3 Ca atoms p.f.u., i.e. between Co6 and Co7. However single crystal X-ray diffraction for Co6 showed a *C2/c* space group. For the sample Co7 no single crystals sized as required for single crystal X-ray diffraction could not be synthesized. We had to use for the samples Co7 and Co8 transmission electron microscopy that enables to obtain diffraction patterns in crystal of submicrometric size, which are instead available for that composition

Two samples with composition  $\text{Ca}_{0.3}\text{Co}_{1.7}\text{Si}_2\text{O}_6$  and  $\text{Ca}_{0.2}\text{Co}_{1.8}\text{Si}_2\text{O}_6$  are then examined by Transmission Electron Microscopy. The samples are crushed, suspended on isopropyl alcohol and deposited on a holey carbon film. A JEOL electron microscope operating at 200 kV equipped by double tilt holder is used. Selected area diffraction patterns are collected along zone axes at different orientation, to show the changes in lattice symmetry.

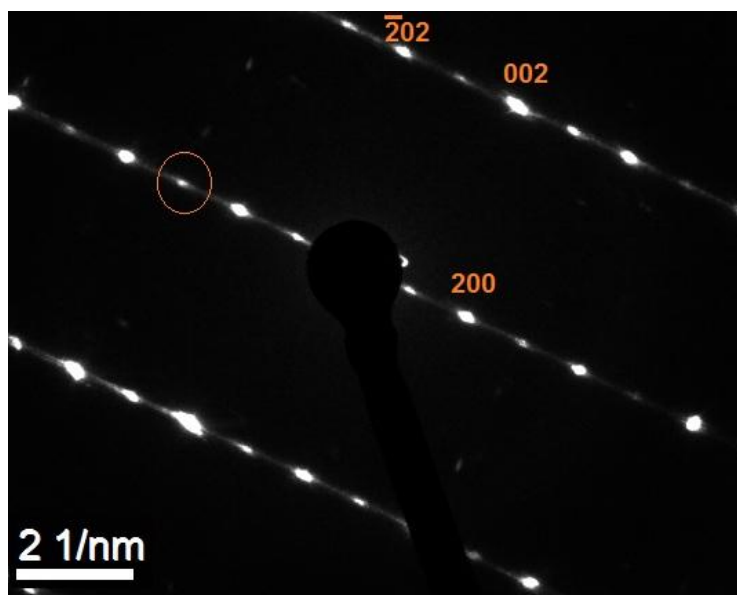


Fig. 3.16.: selected area of a electron diffraction pattern along [010]. Note streaking along  $a^*$ , interpreted as staking disorder, as in Tribaudino (2000)

As shown in the above diffraction pattern, taken from sample Co7 and oriented along the [010] zone axis, rows with spots of alternate intensity are present. The stronger ones are  $h+k$  even, the less intense one, in between of the stronger ones, have indexes  $h+k$  odd, these spots are violating the  $C$  lattice, and indicate a primitive symmetry. By analogy with other pyroxenes, this indicates a space group  $P2_1/c$ . This result gives a definitive confirmation of the occurrence of the transition. The composition at which the transition occurs will be discussed in the following sections.

## ***Comparison with quadrilateral pyroxenes: phase stability and cation ionic radius***

The syntheses at high pressure give important results on the crystal chemistry and phase stability of the series  $\text{CaCoSi}_2\text{O}_6$ - $\text{Co}_2\text{Si}_2\text{O}_6$ . The results obtained in this work, together with literature data, can better define the mechanism of cation substitution and the phase relations in quadrilateral pyroxenes.

In particular, the analysis of the system  $\text{CaCoSi}_2\text{O}_6$ - $\text{Co}_2\text{Si}_2\text{O}_6$  helps to clarify the mechanism of the substitution of large cations like Ca for Co in the M2 site, increasing and completing literature data on the substitution of Ca with a smaller cation in pyroxenes.

In fact in the  $\text{CaCoSi}_2\text{O}_6$ - $\text{Co}_2\text{Si}_2\text{O}_6$  series as the Co atoms substitute Ca in the M2 site we observe:

- 1) a phase transition in clinopyroxenes, from  $C2/c$  to  $P2_1/c$
- 2) exsolution of Ca-rich and poor pyroxenes

This is commonly to other pyroxenes series, when Ca is substituted by Mg or Fe.

Analogies and differences between the series  $\text{CaCoSi}_2\text{O}_6$ - $\text{Co}_2\text{Si}_2\text{O}_6$  and  $\text{CaFeSi}_2\text{O}_6$ - $\text{Fe}_2\text{Si}_2\text{O}_6$  and  $\text{CaMgSi}_2\text{O}_6$ - $\text{Mg}_2\text{Si}_2\text{O}_6$  are then investigated in order to clarify the general mechanism of substitution.

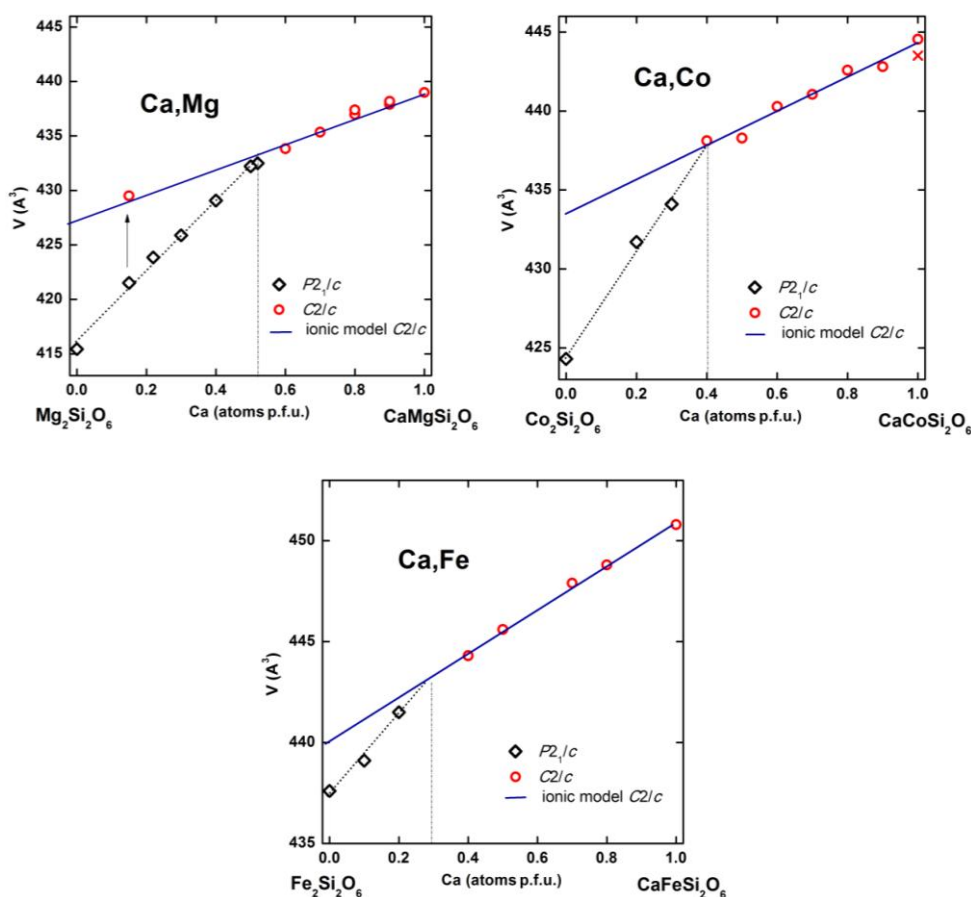


Fig. 3.17: comparison in the cell volume of the three series: blue line represent change in volume modelled by a ionic model, red circles the experimental data for C2/c and black diamond for P2<sub>1</sub>/c pyroxenes.

The cell parameters show the same trend in the three series. Increasing Co, Mg or Fe content we can notice that the *a* parameters decreases, *b* and *c* change little and  $\beta$  increase. The volume, reasonably, decreases since Co, Mg, Fe cations are smaller than Ca.

The changes of the cell parameters with compositions are not linear, in any series, as different trends are observed for a Ca-rich and Ca-poor samples. This is an evidence of the phase transition, as shown in the description of cell parameters of Co-pyroxenes. The turnover occurs at different compositions: at about 0.5 Ca atoms

p.f.u. in Di-En join, at about 0.4 Ca atoms p.f.u. for CaCo-CoCo and 0.3 Ca atoms for Hd-Fs.

The turnover at the transition is most apparent in the volume changes. Changes in volume along the series can be modelled by a ionic model, that is a model in which changes in volume are assumed to occur only by the substitution of cations in the M2 site. Being the substituting cations of different ionic radius and volume, the cell volume decreases only by the decreases size of the substituting cation.

In this model the volume is represented as a difference between the volume of the Ca-rich end member (i.e. Di, Hd or CaCoSi<sub>2</sub>O<sub>6</sub>) and the decrease due to the substitution of a smaller cation for Ca.

$$V = V_{EM} - Z \frac{4}{3} \pi \left[ R_{Ca}^3 - R_M^3 (1 - X_{Ca}) \right]$$

Where  $Z$  is the number of M2 site in the cell, which is 4 in both *C2/c* and *P2<sub>1</sub>/c* pyroxenes

$X$  is the atom fraction per formula unit of Ca in M2 ( $X_{Ca}$ )

$R$  is the ionic radius of Ca ( $R_{Ca}$ ) or Co/Mg/Fe ( $R_M$ ) in six-fold coordination

$V$  is the volume for each series of the Ca-rich end member ( $V_{EM}$ )

The calculated volume is represented by the blue line.

We can notice that in Ca-rich samples, experimental data within the *C2/c* region (red circles) lie on the line of the ionic model, suggesting that changes in volume can be simply explained by the substitution of a larger cation by a smaller one. In Ca-poor region changes in volume are higher than the predicted ones; the decrease in volume can be related also to an effect of the phase transition.

Another important point to note is that the volume likely corresponds to the volume strain due to the high temperature  $P2_1/c$   $C2/c$  phase transition. In the present work no data are provided for the high temperature transition in Ca,Co-pyroxenes but in previous work along the Di-En join (Tribaudino et al., 2002) an high temperature phase transition is observed and the evolution of cell volume with temperature across the transition can be followed. Extrapolating the high temperature  $C2/c$  volume data into the  $P2_1/c$  field at room temperature a difference in volume like that reported in figure 3.17 (black arrow) is found. It appeared that also the  $C2/c$  volume obtained by an extrapolation of the high temperature data lies in a ionic  $C2/c$  trend.

An important result is that within the  $C2/c$  structure changes in volume are ideal and the deviation to ionic behaviour is due simply to the phase transition, contrarily to previous observations by Newton et al., 1979.

We can assume that the turnover represents the composition at which the transition occurs. This point in which the volume-composition trend for Ca-poor  $P2_1/c$  pyroxenes came across those for Ca-rich samples (indicating both the  $C2/c$  symmetry and the ionic model) is the critical composition of the phase transition. This point occurs at a composition of Ca atoms p.f.u. = 0.52 for Di-En, of Ca (a.p.f.u.) = 0.4 for CaCo and Ca (a.p.f.u.) = 0.3 for Hd,Fs. The different critical compositions are related to the different ionic radius: Mg has a ionic radius equal to 0.72 Å, Fe 0.78 Å and Co 0.745 Å (figure 3.18). Changes in volume to pinpoint the transition are also used in the series kanoite-diopside ( $MnMgSi_2O_6$ - $CaMgSi_2O_6$ ) (Arlt et al., 1997). In this series a sharp decrease in volume is observed at the Ca content of 0.2 atoms per formula unit, and like in our samples it is interpreted as an evidence of the phase transition. As Mn has a ionic radius of 0.83Å this corresponds to an

average M2 ionic volume at the transition of  $0.86\text{\AA}$ , again similar to that of our pyroxenes.

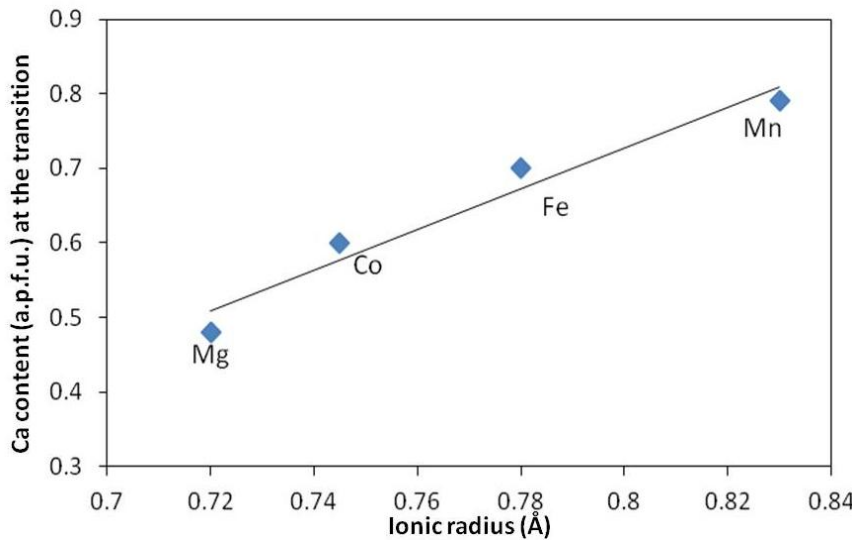


Fig. 3.18: ionic radius of the substituting cation vs with Ca content (a.p.f.u.) at the phase transition

The presence of very similar average ionic radii at the transition suggests that the transition is driven by a critical cation size. This was also proposed by Arlt et al.,(2001), that showed that the temperature of the  $P2_1/c \rightarrow C2/c$  phase transition was higher in samples with lower ionic radius at the M2 site. The transition temperature was linearly related to the cation radius and an extrapolation at room temperature pointed for a critical cation radius of  $0.88\text{\AA}$ , not far from our observation. The average cation radius we obtained is slightly lower than that predicted by Arlt et al.,(2001). It is not clear if this difference is significant or not. If it is, one could possibly speculate on the effect of CFSE, absent for Mg and Mn or of an interaction of microstructures with the transition, which are seemingly present in the Di-En pyroxenes, but were not found in Ca-Co and Ca-Fe pyroxenes.

A ionic model can explain also the different extension of the miscibility gap in the different series.

A well known rule, from an adaptation to silicates of the Hume-Rothery rule used in metals, states that complete isomorphous solid solution occurs for isovalent cations if the ionic radius is less than 15% difference. In the series we examine the difference is by more than 20%, and complete solid solution is not expected to occur. A miscibility gap, of different extent, is revealed by comparison of the phase diagram of the three series at  $P = 3$  GPa.

The gap is asymmetric, being solubility much lower in the Ca-poor region. This occurs because the end-members pyroxenes have not the same structure, and the orthorhombic structure of Ca-poor pyroxenes allows very little Ca entrance. In the orthopyroxenes region of the phase diagram solid solution is then very limited, and quite similar in all the series, while in clinopyroxene the solubility is different in the different series.

Figure 3.19 shows the miscibility gaps of the three series Di-En, Hd-Fs and CaCo at the same pressure plotted together with the ionic radius of the substituting cations and the percentage difference.



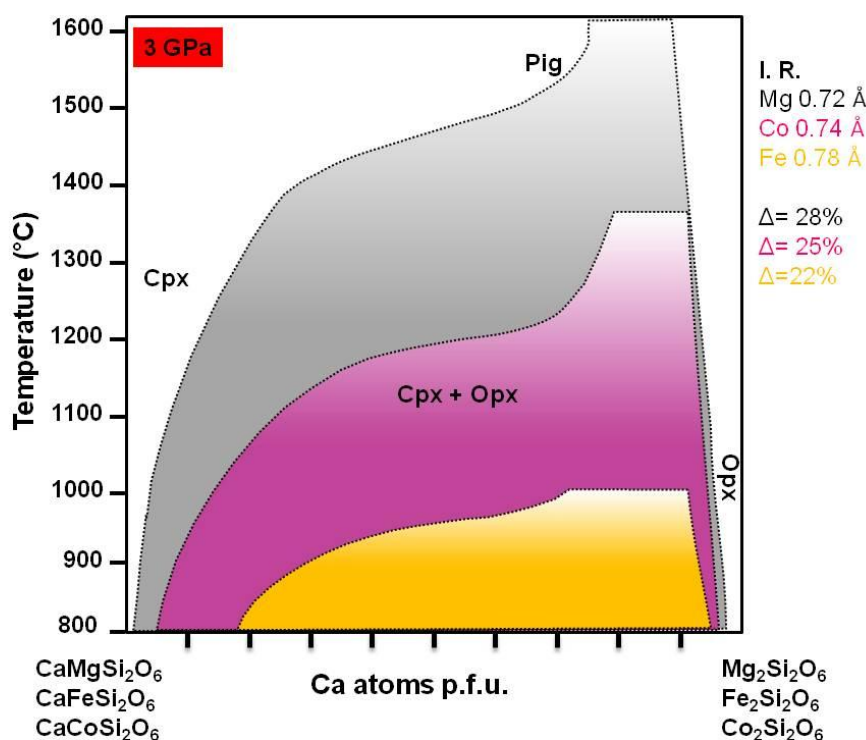


Fig. 3.19: sketch of a phase diagram for the three series examined. Gray colour indicate the miscibility gap of Di-En, pink that of CaCo series and yellow is referred to Hd-Fs.

What is most apparent is that the pyroxene solubility decreases on the Ca rich side with the substituting cation at the M2 site, from Fe to Co and Mg. Also the temperature of the upper limit of the miscibility gap is related to the cation in M2. For example at about Ca content of 0.5 apfu we found single clinopyroxene phase at a temperature of 1500°C for Di-En, 1200°C for CaCo and 900°C for Hd-Fs. Such differences occur by a change in the size of the substituting cation, that is by an increase of the difference of the ionic radius with Ca.

From the above results the most relevant crystal chemical changes due to the substitution of a smaller cation for Ca in M2 can be explained by an ionic model. However structural investigations and TEM observations in the samples of the three series show that simple ionic substitution occurs with several structural changes, as

discussed by Mantovani et al., (2012) using single crystal data of CaCo, Ca-Mg and Ca,Fe.

- a. At first the solid solution occurs by the formation of two subsites in the M2 cavity, M2 and M2'. There are evidences that such splitting occurs also in O atoms. The observed Raman peak enlargement for samples C2/c with intermediate composition is related to this splitting which induces local disorder: to note, peak enlargement is proportional to displacement parameter in CaCo (figure 3.14) and Ca,Mg (Tribaudino et al., 2012).
- b. Changes in the average C2/c structure and in particular in deformation of M2 polyhedron are not linear in spite of the linear behaviour of the volume. For instance the deformation of the M2 polyhedron is not linear. What is observed is that the deformation at first is small and increases with decreasing average ionic radius. Similar behaviour is observed also in Raman peak width (fig. 3.14).
- c. After the phase transition a strong decrease in volume occurs as an effect of chain kinking which reduced the size of M2 polyhedron in addition to the changes in the ionic radius. Again Raman spectra shows a significant deviation in the linear behaviour both in Di-En and CaCo.

In conclusion the most interesting features in the series are explained by ionic radius, although in a flexible structure like pyroxene the detailed changes are rather complex. At the resolution of the present data we can not detail further to verify the effect of other parameters like the crystal field stabilization energy, the microstructural disorder or the combined effect of cation substitutions in the M1 site

## Conclusions

Room and high pressure studies allowed to clarify the phase diagram along the  $\text{CaCoSi}_2\text{O}_6$ - $\text{Co}_2\text{Si}_2\text{O}_6$  series, and to constrain the stability field of the pyroxene phases.

Like it was observed in the hedenbergite - ferrosilite join, Ca,Co-pyroxenes at room pressure have a stability field limited to the Ca-rich end member, and for higher Co content the clinopyroxene destabilize in an assemblage containing also Co-olivine and silica. However it was also observed the metastable formation in Ca-richer samples of Co-ackermanite. This has a strong effect on the final colour, and on the performances of the possible pigment, since the blue colour prevailed even if Co-ackermanite was present in small quantities.

At high pressure instead a complete series of pyroxene phases can be synthesized, showing several features familiar to natural quadrilateral pyroxenes: 1) a transition from the monoclinic  $C2/c$  structure of Ca-richer compositions to a  $P2_1/c$  one in Ca-poorer ones and in an orthopyroxene phase, likely  $Pbca$  as in quadrilateral, for pyroxenes where Ca is lowest.; 2) a large miscibility gap where clinopyroxenes and orthopyroxenes or Ca-rich and Ca-poor monoclinic pyroxenes coexist. In detail however the  $C2/c$  -  $P2_1/c$  transition occurs at a composition between that of Ca-Mg and Ca-Fe pyroxenes, and the extension of the miscibility gap at high pressure is also smaller than in Ca-Mg and larger than in Ca-Fe pyroxenes.

Also several crystal chemical features are similar in Co-pyroxenes with Ca-Mg and Ca-Fe ones: 1) the large M2 polyhedron hosts split sites for the larger Ca and

smaller Co, Fe or Mg atoms; 2) changes of cell parameters and angles and individual bond lengths are not linear, showing a change in slope at the phase transition, but also a non linear behaviour within the  $C2/c$  phase; 3) the structural and spectroscopic markers of the phase transition are very similar in the three series.

The above results can be interpreted within the framework of a model considering the differences in ionic radius of the three end members: in fact the changes in volume, in spite of the non linear nature of the changes in individual cell parameters are linear within the  $C2/c$  field, and can be fully described in a model simply accounting for the different ionic radius of the substituting cation.

Likewise, the critical composition of the phase transition and the extension of the miscibility gap changes with cation radius of the substituting cation: the higher the radius the larger the extension of the  $C2/c$  field and the smaller the miscibility gap.

# REFERENCES

## WEB SITES REFERENCES

Cobalt Development institute: <http://www.thecdi.com>.

Cobalt: <http://education.jlab.org/itselemental/ele027.html>.

Cobalt: <http://en.wikipedia.org/wiki/Cobalt>.

CTIOA Ceramic Tile Institute of America.

Oil paint cobalt-based: <http://www.myartandcraftsupplies.com/Williamsburg-Oil-Paint-Sets.html>.

Akimoto, S.-I., Katsura, T., Syono, Y., Fujisawa, H. and Komada, E., 1965. Polymorphic transitions of pyroxenes FeSiO<sub>3</sub> and CoSiO<sub>3</sub> at high pressures and temperatures. *Journal of Geophysical Research*, 70: 5269-5278.

Arlt, T., Armbruster, T. and 1997. The temperature dependent  $P2_1/c-C2/c$  phase transition in the clinopyroxene kanoite MnMg[Si<sub>2</sub>O<sub>6</sub>]: a single-crystal X-ray and optical study. *European Journal of Mineralogy*, 9: 953-964.

Biggar, G.M., 1969. The System CaO-NiO-SiO<sub>2</sub>. *Journal of the American Ceramic Society*, 52(6): 316-317.

Bondioli, F., 2008. I pigmenti ceramici. *Ceramica Informazione*, 7: 95-100.

Bouchard, M. and Gambardella, A., 2010. Raman microscopy study of synthetic cobalt blue spinels used in the field of art. *Journal of Raman Spectroscopy*, 41(11): 1477-1485.

Boyd, F.R. and Schairer, J.F., 1964. The System MgSiO<sub>3</sub>—CaMgSi<sub>2</sub>O<sub>6</sub>. *Journal of Petrology*, 5(2): 275-309.

Bromiley, G.D., Keppler, H., McCammon, C., Bromiley, F.A. and Jacobsen, S.D., 2004. Hydrogen solubility and speciation in natural, gem-quality chromian diopside. *American Mineralogist*, 89: 941-949.

Bruno, E., Carbonin, S. and Molin, G., 1982. Crystal structures of Ca-rich clinopyroxenes on the CaMgSi<sub>2</sub>O<sub>6</sub>-Mg<sub>2</sub>Si<sub>2</sub>O<sub>6</sub> join. *Tschermaks mineralogische und petrographische Mitteilungen*, 29(4): 223-240.

Burnham, C.W., Clark, J.R., Papike, J.J. and Prewitt, C.T., 1967. A proposed crystallographic nomenclature for clinopyroxene structures. *Zeitschrift für Kristallographie - Crystalline Materials*, 125(125): 109-119.

- Burns, R.G., 1993. *Mineralogical Applications of Crystal Field Theory*. Cambridge University Press.
- Cameron, M. and Papike, J.J., 1981. Structural and chemical variation in pyroxenes. *American Mineralogist*, 66: 1-50.
- Carlson, W.D., 1989. Subsolidus phase equilibria near the enstatite-diopside join in CaO-MgO-Al<sub>2</sub>O<sub>3</sub>-SiO<sub>2</sub> at atmospheric pressure. *American Mineralogist*, 74(3-4): 325-332.
- Cassese, A., 2006. *Zeoliti come precursori di materiali ceramici* - PhD Thesis, Università di Napoli.
- Choi, S.R. and Bansal, N.P., 2005. Mechanical behavior of zirconia/alumina composites. *Ceramics International*, 31(1): 39-46.
- Colomban, P., Sagon, G. and Faurel, X., 2001. Differentiation of antique ceramics from the Raman spectra of their coloured glazes and paintings. *Journal of Raman Spectroscopy*, 32: 351-360.
- DCMA, 1991. *Classification and Chemical Description of the Mixed Metal Oxide Inorganic Colour Pigments*. DCMA Complex Inorganic Color Pigment and Ceramic Colors Committee.
- Deer, W.A., Howie, R.A. and Zussman, J., 1963. *Rock-forming minerals*. Vol 2. Single chain silicate. Gren and Co LTD, London.
- Downs, R.T., 2003. Topology of the pyroxenes as a function of temperature, pressure, and composition as determined from the procrystal electron density. *American Mineralogist*, 88(4): 556-566.
- Durand, G., Vilminot, S., Rabu, P., Derory, A., Lambour, J.P. and Ressouche, E., 1996. Synthesis, Structure, and Magnetic Properties of CaMSi<sub>2</sub>O<sub>6</sub>(M= Co, Ni) Compounds and Their Solid Solutions. *Journal of Solid State Chemistry*, 124(2): 374-380.
- Eppler, R.A., 2000. *Colorants for Ceramics*, Kirk-Othmer Encyclopedia of Chemical Technology. John Wiley & Sons, Inc.
- Fores, A., Llusar, M., Badenes, J.A., Calbo, J., Tena, M.A. and Monros, G., 2000. Cobalt minimisation in willemite (CoZnSiO) ceramic pigments. *Green Chemistry*, 2(3): 93-100.
- Gasparik, T., 1984. Two-pyroxene thermobarometry with new experimental data in the system CaO-MgO-Al<sub>2</sub>O<sub>3</sub>-SiO<sub>2</sub>. *Contributions to Mineralogy and Petrology*, 87(1): 87-97.
- Gasparik, T. and Lindsley, D.H., 1980. Phase equilibria at high pressure of pyroxenes containing monovalent and trivalent ions. *Reviews in Mineralogy and Geochemistry*, 7(1): 309-339.

- Ghose, S., Wan, C. and Okamura, F.P., 1987. Crystal structures of CaNiSi<sub>2</sub>O<sub>6</sub> and CaCoSi<sub>2</sub>O<sub>6</sub> and some crystal-chemical relations in C2/c clinopyroxenes. *American Mineralogist*, 72: 375-381.
- HORIBA, Labspec -Raman Spectroscopy software
- Huebner, J.S., 1980a. Pyroxene phase equilibria at low pressure. *Reviews in mineralogy: Minerl. Soc. America*, 7: 213-280.
- Hugh-Jones, D.A., Woodland, A.B. and Angel, R.J., 1994. The structure of high-pressure C2/c ferrosilite and crystal chemistry of high-pressure C2/c pyroxenes. *American Mineralogist*, 79(11-12): 1032-1041.
- Iezzi, G., Tribaudino, M., Ventura, G.D. and Margiolaki, I., 2011. The high-temperature P21/m -> C2/m phase transitions in synthetic amphiboles along the richterite-(BMg)-richterite join. *American Mineralogist*, 96(2-3): 353-363.
- Ito, T., 1950. X-ray studies on polymorphism. Maruzen, Tokyo, 231 pp.
- Jonynaitė, D., Senvaitienė, J., Kiuberis, J. and Kareiva, A., 2009. XRD characterization of cobalt-based historical pigments and glazes. *chemija*, 20(1): 10-18.
- Kim, J.H., 1992. Cobalt and inorganic cobalt compound. Concise International Chemical Assessment Document 69.
- Kimata, M., 1983. The crystal structure and stability of Co-akermanite, Ca<sub>2</sub>CoSi<sub>2</sub>O<sub>7</sub>, compared with the mineralogical behavior of Mg cation. *Neues Jahrbuch für Mineralogie, Abhandlungen*, 146: 221-241.
- Konnert, J.H. and E, A.D., 1978. The crystal structure of low tridymite. *Acta Crystallographica B* 34 391-403.
- Larson, A.C. and Von Dreele, R.B.G., 2000. General Structural Analysis System (GSAS). Los Alamos National Laboratory Report, LAUR: 86-748.
- Leung, P.L. and Luo, H., 2000. A study of provenance and dating of ancient Chinese porcelain by x-ray fluorescence spectrometry. *X-Ray Spectrometry* 29(1): 34-38.
- Lindsley, D.H., 1980. Phase equilibria of pyroxenes at pressures >1 atmosphere. *Reviews in Mineralogy and Geochemistry*, 7(1): 289-307.
- Lindsley, D.H. and Munoz, J.L., 1969. Subsolidus relations along the join hedenbergite-ferrosilite. *American Journal of Science*, 267: 295-324.
- Llusar, M., Forés, A., Badenes, J.A., Calbo, J., Tena, M.A. and Monrós, G., 2001. Colour analysis of some cobalt-based blue pigments. *Journal of the European Ceramic Society*, 21(8): 1121-1130.



- Longhi, J. and Boudreau, A.E., 1980. The orthoenstatite liquidus field in the system forsterite-diopside-silica at one atmosphere. *American Mineralogist*, 65(5-6): 563-573.
- Masse, D.P. and Muan, A., 1965. Phase relations in the system CoO-SiO<sub>2</sub>. *Transition Metal Society AIME*, 233: 1448-1449.
- Masse, S., Boch, P. and Vaissière, N., 1999. Trapping of nickel and cobalt in CaNiSi<sub>2</sub>O<sub>6</sub> and CaCoSi<sub>2</sub>O<sub>6</sub> diopside-like phases in heat-treated cement. *Journal of the European Ceramic Society*, 19(1): 93-98.
- Melo, D.M.A., Cunha, J.D., Fernandes, J.D.G., Bernardi, M.I., Melo, M.A.F. and Martinelli, A.E., 2003. Evaluation of CoAl<sub>2</sub>O<sub>4</sub> as ceramic pigments. *Materials Research Bulletin*, 38(9): 1559-1564.
- Mimani, T. and Ghosh, S., 2000. Combustion synthesis of cobalt pigments: Blue and pink. *Current Science*, 78(7): 892-896.
- Morimoto, N., 1989. Nomenclature of pyroxenes. *Canadian Mineralogist*, 27: 143-156.
- Morimoto, N., Appleman, D.E. and Evans Jr., H.T., 1960. The crystal structures of clinoenstatite and pigeonites. *Zeitschrift für Kristallographie*, 114: 120-147.
- Morimoto, N., Tokonami, M., Watanabe, M. and Koto, K., 1974. Crystal structures of three polymorphs of Co<sub>2</sub>SiO<sub>4</sub>. *American Mineralogist*, 59: 475-485.
- Mukhopadhyay, S. and Jacob, T., 1996. Phase equilibria in the system CaO-CoO-SiO<sub>2</sub> and Gibbs energies of formation of the quaternary oxides CaCoSi<sub>2</sub>O<sub>6</sub>, Ca<sub>2</sub>CoSi<sub>2</sub>O<sub>7</sub>, and CaCoSiO<sub>4</sub>. *American Mineralogist*, 81: 963-972.
- Navrotsky, A. and Coons, W.E., 1976. Thermochemistry of some pyroxenes and related compounds. *Geochimica et Cosmochimica Acta* 40: 1281-1288.
- Ohashi, Y., Burnham, C.W. and Finger, L.W., 1975a. The effect of Ca-Fe substitution on the clinopyroxene crystal structure. *American Mineralogist*, 60: 423-434.
- Ozel, E., Yurdakul, H., Turan, S., Ardit, M., Cruciani, G. and Dondi, M., 2010. Co-doped willemite ceramic pigments: Technological behaviour, crystal structure and optical properties. *Journal of the European Ceramic Society*, 30(16): 3319-3329.
- Peco, G., 1991. I prodotti ceramici: dalla tradizione all'alta tecnologia. Marzorati, Milano.
- Putnis, A., 1992. An introduction to mineral science. Cambridge University Press.
- Redhammer, G.J., Nestola, F. and Miletich, R., 2012. Synthetic LiAlGe<sub>2</sub>O<sub>6</sub>: The first pyroxene with P21/n symmetry. *American Mineralogist*, 97(7): 1213-1218.

- Riederer, J., 1974. Recently identified Egyptian Pigments. *Archaeometry*, 16(1): 102-109.
- Rietveld, H., 1969. A profile refinement method for nuclear and magnetic structures. *Journal of Applied Crystallography*, 2(2): 65-71.
- S Sasaki, Y.T., K Fujino, S Akimoto, 1982. Electron-density distribution of three orthopyroxenes, Mg<sub>2</sub>Si<sub>2</sub>O<sub>6</sub>, Co<sub>2</sub>Si<sub>2</sub>O<sub>6</sub> and Fe<sub>2</sub>Si<sub>2</sub>O<sub>6</sub>. *Zeit. Kristallogr.*
- Shannon, R., 1976. Revised effective ionic radii and systematic studies of interatomic distances in halides and chalcogenides. *Acta Crystallographica Section A*, 32(5): 751-767.
- Singer, F. and Singer, S.S., 1979. *Industrial ceramics*. Chapman & Hall, London, pp. 299-302.
- Taran, M.N. and Rossman, G.R., 2001. Optical spectra of Co<sup>2+</sup> in three synthetic silicate minerals. *American Mineralogist*, 86(7-8): 889-895.
- Tribaudino, M. and Nestola, F., 2002. Average and local structure in P21/c clinopyroxenes along the join diopside-enstatite (CaMgSi<sub>2</sub>O<sub>6</sub>-Mg<sub>2</sub>Si<sub>2</sub>O<sub>6</sub>). *European Journal of Mineralogy*, 14(3): 549-555.
- Tribaudino, M., Nestola, F., Camara, F. and Domeneghetti, M.C., 2002. The high-temperature P21/c-C2/c phase transition in Fe-free pyroxene (Ca<sub>0.15</sub>Mg<sub>1.85</sub>Si<sub>2</sub>O<sub>6</sub>): Structural and thermodynamic behavior, pp. 648-657.
- Tribaudino, M., Prencipe, M., Nestola, F. and Hanfland, M., 2001. A P21/c-C2/c high-pressure phase transition in Ca<sub>0.5</sub>Mg<sub>1.5</sub>Si<sub>2</sub>O<sub>6</sub> clinopyroxene. *American Mineralogist*, 86(7-8): 807-813.
- Wang, A., Jolliff, B.L., Haskin, L.A., Kuebler, K.E. and Viskupic, K.M., 2001. Characterization and comparison of structural and compositional features of planetary quadrilateral pyroxenes by Raman spectroscopy. *American Mineralogist*, 86(7-8): 790-806.
- Warren, B. and Bragg, W.L., 1928. The structure of diopside *Zeitschrift für Kristallographie*, 69: 168-193.
- Warren, B.E. and Modell, D.I., 1930. The structure of enstatite MgSiO<sub>3</sub>. *Zeitschrift für Kristallographie*, 75: 1-14.
- White, B.W., McCarthy, G.J. and Scheetz, B.E., 1971. Optical spectra of chromium, nickel, and cobalt-containing pyroxenes. *American Mineralogist*, 56: 72-89.
- Yang, H., Finger, L.W., Conrad, P.G., Prewitt, C.T. and Hazen, R.M., 1999. A new pyroxene structure at high pressures: Single crystal X-ray and Raman study of the Pbcn-P21cn phase transition in protopyroxene. *American Mineralogist*, 84: 245-256.

Zucchiatti, A., Bouquillon, A., Katona, I. and D'Alessandro, A., 2006. The della Robbia blue: a case study for the use of Cobalt Pigments in ceramics during the italian reinassence. *Archaeometry*, 48(1): 131-152.

# APPENDIX

## MATERIALS AND METHODS

### SYNTHESIS

#### ***High pressure synthesis: the piston cylinder apparatus***

*High pressure synthesis were made at Grant Institute Earth Science, School of GeoSciences, University of Edinburgh (Prof. Bromiley Geoffrey)*

The piston cylinder is a large-volume, high-pressure apparatus that can be used to routinely generate pressures of 2 to 4 GPa with simultaneous temperatures up to 1800 °C. High pressures in this study are generated over the sample accommodated in a welded Pt (platinum) capsule with a diameter of 3mm and a height of 5mm, using a piston-cylinder device converting a small load on a large piston to a large load on a small piston (Fig. 1).

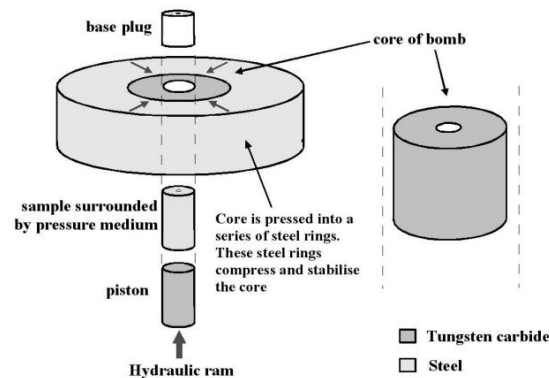


*Fig. 1: Schematic diagram describing the set up of piston-cylinder*

A Pt capsule is chosen since it is chemically inert against the compounds of interest in this study. Small carbide piston is forced into a pressure vessel, known as a bomb, which consists of a carbide core with central hole surrounded by steel support rings. Movement of the piston into the core compresses the sample volume. The sample assembly consists of a soft, deformable pressure medium (talc, NaCl, BaCO<sub>3</sub> etc) which is able to convert uniaxial compression into a hydrostatic sample pressure. An internal graphite furnace sits inside the pressure medium. Simultaneous high temperatures can be achieved by passing a large voltage across this internal resistance furnace. There is a Pyrex cylinder between the pressure

medium and the heater, which acts as an electrical insulator as well as a trap for water. The capsule is located in the centre of the sample assembly, surrounded and held in place by machineable ceramics (Fig.2). Space above and below the capsule was filled with plugs of  $\text{Al}_2\text{O}_3$  (Fig.2). The upper plug has a small central hole drilled for the R-type thermocouple. Pb (lead) foil was wrapped around the cell so that it can act as a lubricant at elevated pressure and temperature, and to aid removal of the sample assembly from the bomb after the experiment.

The entire assembly is placed into the tungsten carbide core and then an insulated steel plug is placed on top. This plug completes the heating circuit, and once the pressure is applied, clamps the thermocouple in place preventing it from extruding upward.

The piston-cylinder apparatus is made up of a frame and two hydraulic rams. The frame usually consists of three or four supporting posts. Pressure is first applied to the whole stack to compress and stabilize the pressure before load is applied to the sample via the piston. Such designs are described as end-loaded.

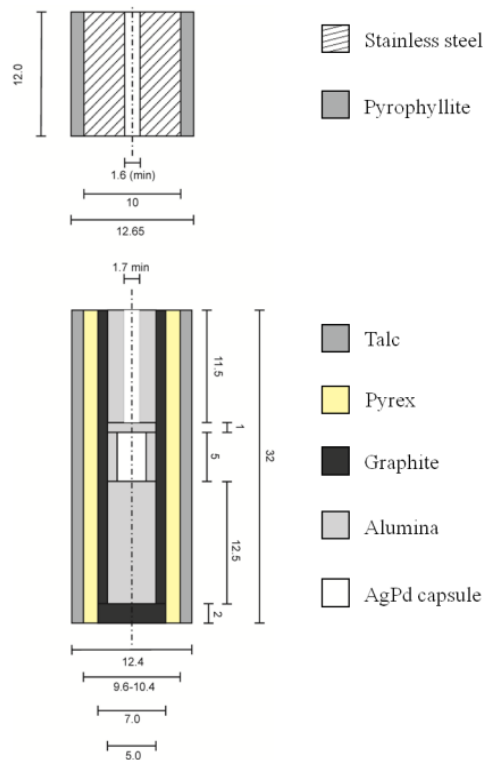


*Fig.2 Cross section of the piston-cylinder sample assembly (all units are in mm), composed of base plug (stainless steel/pyrophyllite) and Talc-Pyrex Assembly*

## CHARACTERIZATION

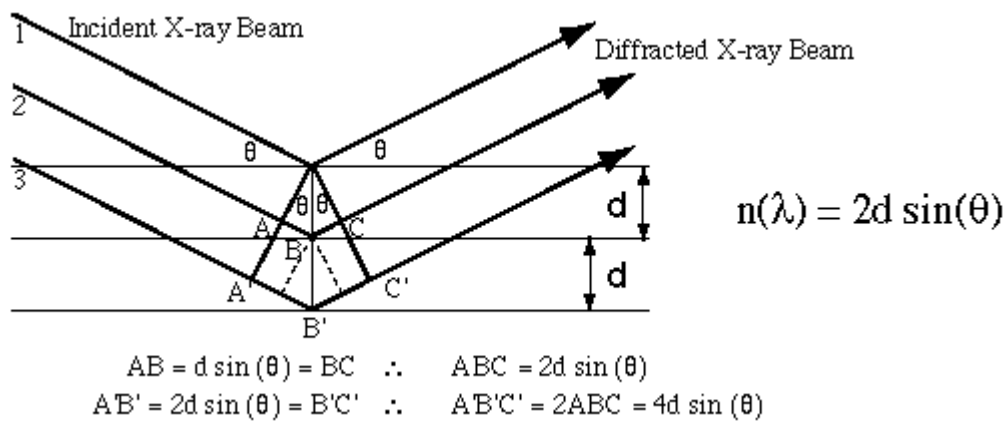
### ***Powder (PXRD) and Single crystal (SCXRD) X-ray diffraction***

*PXRD analysis on high pressure samples were made at the X-ray Fluorescence and X-Ray Diffraction Laboratory, Grant Institute Earth Science School of GeoSciences, University of Edinburgh (Dr. Nic Odling)*

*XRD on room pressure samples were done at ISTECCNR, Istituto Scienze e Tecnologie Ceramiche, Faenza. ( Dott.ssa Zanelli Chiara and Dott. Dondi Michele)*

*Some PXRD and SCXRD were done at the Dipartimento di Chimica inorganica e analitica, Università degli studi di Parma (Dott. Francesco Mezzadri and Prof. Calestani Gianluca)*

X-ray diffraction occurs when electromagnetic radiation with wavelength comparable to atomic spacing are scattered in a specular fashion by atoms in a crystalline structure and undergo constructive interference in accordance to Bragg's law.



For a crystalline solid, the waves are scattered from lattice planes separated by the interplanar distance  $d$ . If the scattered waves interfered constructively, they remain in phase since the path length of each wave is equal to an integer multiple of the wavelength. The path difference between two waves undergoing constructive interference is given by

$$2d \sin \theta = n\lambda$$

where  $\theta$  is the scattering angle,  $n$  is an integer determined by the order given, and  $\lambda$  is the wavelength. This is the Bragg's law, which describes the condition for

constructive interference from successive crystallographic planes ( $h,k$ , and  $l$ , as given in Miller Notation) of the crystalline lattice. A diffraction pattern is obtained by measuring the intensity of scattered waves as a function of scattering angle.

**Powder X-ray Diffraction** (PXRD) can be used to identify phases and to determine lattice parameters, crystalline grade in a sample. It is even possible to obtain the coordinates of atoms in the unit cell (by Rietveld refinement). For this thesis PXRD was used to determine and quantify the phases present and the lattice parameters (especially in part III). The information obtained is a statistical average of an area covering many grains (few milligrams).

**Single-crystal X-ray Diffraction** is an analytical technique which provides detailed information about the internal lattice of crystalline substances, including unit cell dimensions, bond-lengths, bond-angles, and details of site-ordering. Directly related is single-crystal refinement, where the data generated from the X-ray analysis is interpreted and refined to obtain the crystal structure.

On this thesis only a mention was done on SCXRD being the result of this analysis to be published.

### **Rietveld analysis**

The standard method of analyzing powder diffraction data is known as "Rietveld profile refinement" and named after Hugo Rietveld (Rietveld, 1969). The method involves fitting the parameters of a model to the measured "whole-profile", which is the intensity measured as a function of scattering angle. The model parameters in Rietveld refinement describe different aspects of the profile and can be divided into three general categories. First, the set of parameters which determine crystal symmetry (space group), unit cell parameters, atomic positions, site occupancy and displacements; these parameters describe the positions and integrated intensities of Bragg reflections. Second, there are the parameters which describe the background. Inelastic and/or incoherent scattering from the sample and its environment, air scattering, electronic noise, and other unwanted sources may contribute to the background. The Bragg peaks can usually be separated from the background because variation of the background scattering with scattering angle is relatively slow. A third set of parameters describe the shapes of Bragg peaks. Peak



broadening is in part due to the resolution of the instrument itself, however crystallite size and strain effects may also contribute to the broadening. The Rietveld refinement is guided numerically using agreement indices, or  $R$  values. The quantity minimized in the refinement is the residual  $S_y$

$$S_y = \sum_i w_i [y_i(ops) - y_i(calc)]^2$$

where  $y_i(ops)$  is the observed intensity at step  $i$ ,  $y_i(calc)$  is the calculated intensity and  $w_i$  is the weight. This quantity is included in the weighted-profile  $R$  value,  $R_{wp}$ , which is defined as

$$R_{wp} = \left\{ \frac{\sum_i w_i [y_i(ops) - y_i(calc)]^2}{\sum_i w_i [y_i(ops)]^2} \right\}^{1/2}$$

Ideally  $R_{wp}$  should approach the statistically expected  $R$  value,  $R_{exp}$ ,

$$R_{exp} = \left[ \frac{(N - P)}{\sum_i^N w_i y_i(ops)^2} \right]^{1/2}$$

where  $N$  is the number of observations and  $P$  the number of parameters. The goodness of fit is

$$\chi^2 = \left( \frac{R_{wp}}{R_{exp}} \right)^2$$

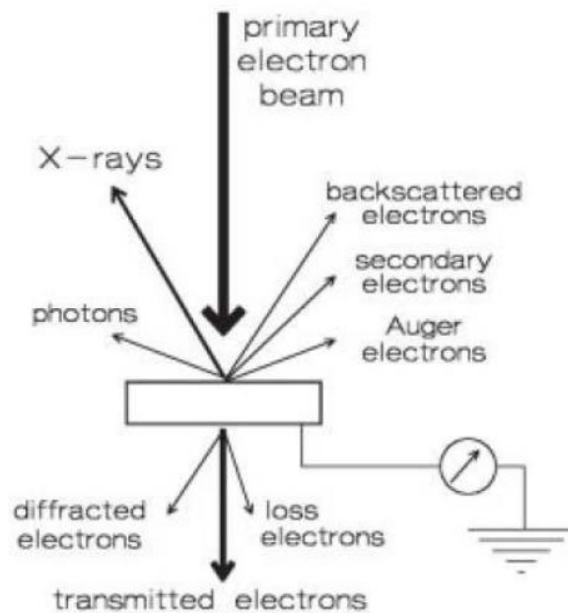
Rietveld profile refinements in this study were performed on the XRD powder data using the GSAS suite of programs (Larson and Von Dreele, 2000). Peak shapes were typically described by a linear combination of Lorentzian and Gaussian functions, modelled by pseudo-Voigt functions. In this work Rietveld refinements were made on every diffraction pattern to quantify phases and structural modification.

**Scanning electron microscope – energy dispersion spectroscopy (SEM-EDS)**

*SEM-EDS analysis were performed at the Dipartimento di Fisica e Scienze della Terra “Macedonio Melloni”, Università degli Studi di Parma (Dott.ssa Salvioli Emma)*

Electron microscopy is a rather straightforward technique used to determine the size and shape of supported particles. Electrons have characteristic wavelengths of less than 1 angstrom, and come close to monitoring atomic detail.

In this figure we summarize what happens when a primary electron beam of energy between 10 and 40 keV hits a sample:



- Emitted X-rays are characteristic for an element and allow for a determination of the chemical composition of a selected part of the sample. This technique is referred to as energy-dispersive X-ray analysis (EDX)
- Depending on sample thickness a fraction of the electrons passes through the sample without suffering energy loss. As the attenuation of the beam depends on density and thickness, the transmitted electrons form a two-dimensional projection of the sample.

- Electrons are diffracted by particles if these are favourably oriented towards the beam, enabling crystallographic information.
- Electrons can collide with atoms in the sample and be scattered back; backscattering becomes more effective as the mass of the atom increases. If a region of the sample contains heavier atoms (e.g. Pt) than the surroundings, it can be distinguished due to a higher yield of backscattered electrons.
- Auger electrons and X-rays are formed in the relaxation of core-ionized atoms.
- Electrons excite characteristic transitions in the sample, which can be studied by analyzing the energy loss suffered by the primary electrons.
- Many electrons lose energy in a cascade of consecutive inelastic collisions. Most secondary electrons emitted by the sample undergo their last loss process in the surface region.
- The emission of a range of photons from UV to infrared, called cathode luminescence, is mainly caused by the recombination of electron–hole pairs in the sample.

In this work BS images were recorded with the aim of discriminate different phases present using different atomic average number. Last but not least chemical information were gave by energy dispersive spectrometer.

### **Raman Spectroscopy**

*Raman spectroscopy was performed at Dipartimento di Fisica e Scienze della Terra “Macedonio Melloni”, Università degli Studi di Parma.(Prof. Pier Paolo Lottici, Dott. Danilo Bersani)*

Raman spectroscopy is a spectroscopic technique used to observe vibrational, rotational, and other low-frequency modes in a system.<sup>[1]</sup> It relies on inelastic scattering, or Raman scattering, of monochromatic light, usually from a laser in the visible, near infrared, or near ultraviolet range. The laser light interacts with molecular vibrations, phonons or other excitations in the system, resulting in the

energy of the laser photons being shifted up or down. The shift in energy gives information about the vibrational modes in the system. Infrared spectroscopy yields similar, but complementary, information.

Typically, a sample is illuminated with a laser beam. Light from the illuminated spot is collected with a lens and sent through a monochromator. Wavelengths close to the laser line due to elastic Rayleigh scattering are filtered out while the rest of the collected light is dispersed onto a detector.

Spontaneous Raman scattering is typically very weak, and as a result the main difficulty of Raman spectroscopy is separating the weak inelastically scattered light from the intense Rayleigh scattered laser light.

### ***Transmission Electron Microscopy (TEM)***

*TEM analysis were performed at IMEM-CNR at Università degli Studi di Parma (Dott. Giovanni Bertoni)*

Transmission electron microscopy (TEM) is a microscopy technique whereby a beam of electrons is transmitted through an ultra thin specimen, interacting with the specimen as it passes through. An image is formed from the interaction of the electrons transmitted through the specimen; the image is magnified and focused onto an imaging device, such as a fluorescent screen, on a layer of photographic film, or to be detected by a sensor such as a CCD camera.

TEMs are capable of imaging at a significantly higher resolution than light microscopes, owing to the small de Broglie wavelength of electrons. This enables the instrument's user to examine fine detail—even as small as a single column of atoms, which is tens of thousands times smaller than the smallest resolvable object in a light microscope. TEM forms a major analysis method in a range of scientific fields, in both physical and biological sciences. At smaller magnifications TEM image contrast is due to absorption of electrons in the material, due to the thickness and composition of the material. At higher magnifications complex wave interactions modulate the intensity of the image, requiring expert analysis of observed images. Alternate modes of use allow for the TEM to observe modulations in chemical

identity, crystal orientation, electronic structure and sample induced electron phase shift as well as the regular absorption based imaging.

TEM analysis were performed at IMEM-CNR at Università degli Studi di Parma. (Dott. Giovanni Bertoni)

### ***Ultraviolet–visible spectroscopy***

*UV-VIS spectroscopy were performed at the Dipartimento di Fisica e Scienze della Terra “Macedonio Melloni”, Università degli Studi di Parma (Prof. Andrea Baraldi)*

UV-VIS spectroscopy refers to absorption spectroscopy or reflectance spectroscopy in the ultraviolet-visible spectral region. This means it uses light in the visible and adjacent (near-UV and near-infrared (NIR)) ranges. The absorption or reflectance in the visible range directly affects the perceived color of the chemicals involved. In this region of the electromagnetic spectrum, molecules undergo electronic transitions. This technique is complementary to fluorescence spectroscopy, in that fluorescence deals with transitions from the excited state to the ground state, while absorption measures transitions from the ground state to the excited state. The principles of the method were based on molecules containing  $\pi$ -electrons or non-bonding electrons (n-electrons) that can absorb the energy in the form of ultraviolet or visible light to excite these electrons to higher anti-bonding molecular orbitals.<sup>[2]</sup> The more easily excited the electrons the longer the wavelength of light it can absorb.

### ***Colour analysis***

*Colour analysis were performed at the Dipartimento di Fisica e Scienze della Terra “Macedonio Melloni”, Università degli Studi di Parma (Prof. Claudio Oleari)*